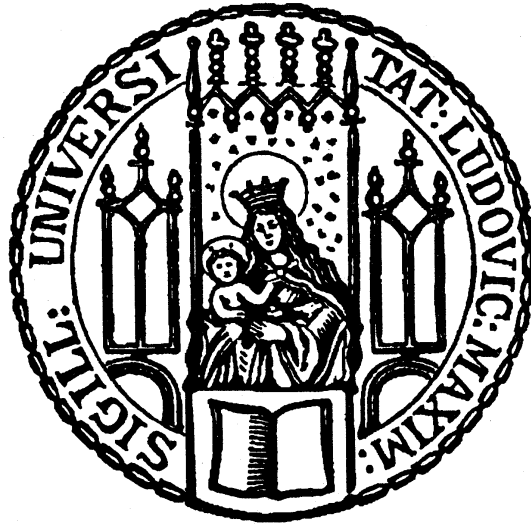


# Search for supersymmetry events with two same-sign leptons



Dissertation der Fakultät für Physik  
der  
Ludwig-Maximilians-Universität München

vorgelegt von  
Christian Kummer  
geboren in München

München, im Januar 2010

1. Gutachter: Prof. Dr. Dorothee Schaile
2. Gutachter: Prof. Dr. Wolfgang Dünneberger

Tag der mündlichen Prüfung: 09.03.2010

meiner Familie



## Abstract

Supersymmetry is a hypothetical symmetry between bosons and fermions, which is broken by an unknown mechanism. So far, there is no experimental evidence for the existence of supersymmetric particles. Some Supersymmetry scenarios are predicted to be within reach of the ATLAS detector at the Large Hadron Collider.

Final states with two isolated leptons (muons and electrons), that have same signs of charge, are suitable for the discovery of supersymmetric cascade decays. There are numerous supersymmetric processes that can yield final states with two same-sign or more leptons. Typically, these processes tend to have long cascade decay chains, producing high-energetic jets. Charged leptons are produced from decaying charginos and neutralinos in the cascades. If the R-parity is conserved and the lightest supersymmetric particle is a neutralino, supersymmetric processes lead to a large amount of missing energy in the detector. The most important Standard Model background for the same-sign dilepton channel is the semileptonic decay of top-antitop-pairs. One lepton originates from the leptonic decay of the W boson, the other lepton originates from one of the b quarks. Here, the neutrinos are responsible for the missing energy.

The Standard Model background can be strongly reduced by applying cuts on the transverse momenta of jets, on the missing energy and on the lepton isolation.

In this thesis, a cut-based analysis is presented, which is suitable for a discovery of the ATLAS SU4 point and other supersymmetric models in the mSUGRA parameter space. The analysis is optimized for a LHC center-of-mass energy of 10 TeV and for an integrated luminosity of  $200 \text{ pb}^{-1}$ .

A method to improve the estimation of the QCD background is presented and taken into account in the analysis.

Furthermore, a method to estimate the Standard Model background from data is presented. With an extensive statistical analysis, the discovery- and the exclusion potential is discussed for the ATLAS SU4 point and several additional example points in the mSUGRA parameter space.

## Zusammenfassung

Supersymmetrie ist eine hypothetische Symmetrie zwischen Bosonen und Fermionen, die aus noch unbekanntem Grund gebrochen ist. Bisher gab es noch keinen experimentellen Nachweis supersymmetrischer Teilchen. Es werden einige supersymmetrische Szenarien vorhergesagt, die innerhalb der Nachweisgrenzen des ATLAS Detektors am Large Hadron Collider liegen. Endzustände mit zwei isolierten Leptonen (Elektronen und Myonen), die gleiches Ladungsvorzeichen tragen, sind für eine Entdeckung supersymmetrischer Zerfallskaskaden geeignet. Zahlreiche supersymmetrische Prozesse können zu Endzuständen mit zwei gleich geladenen oder mehreren Leptonen führen. Üblicherweise haben diese Prozesse lange Zerfallskaskaden, in denen unter anderem hochenergetische Jets produziert werden. Die geladenen Leptonen werden beim Zerfall von Charginos und Neutralinos in den Zerfallskaskaden erzeugt. Sofern die R-Parität erhalten und das leichteste supersymmetrische Teilchen ein Neutralino ist, führen supersymmetrische Prozesse zu einem hohen Wert an fehlender Energie im Detektor. Der bedeutendste Untergrundprozess des Standardmodells für den Dileptonkanal mit gleichen Ladungsvorzeichen ist der semileptonische Zerfall von Topquark-Antitopquark-Paaren. Ein Lepton stammt hier vom semileptonischen Zerfall eines W-Bosons, das andere Lepton entsteht aus einem b-Quark. In diesem Fall sind die Neutrinos für die fehlende Energie verantwortlich.

In dieser Arbeit wird eine schnittbasierte Analyse vorgestellt, die für eine Entdeckung des ATLAS SU4-Punktes und weiteren supersymmetrischen Modellen innerhalb des mSUGRA-Parameterraumes geeignet ist. Die Analyse wurde für eine LHC-Schwerpunktsenergie von 10 TeV und eine integrierte Luminosität von  $200 \text{ pb}^{-1}$  optimiert. Es wird eine verbesserte Abschätzung des QCD-Untergrundes präsentiert und in der Analyse verwendet. Des Weiteren wird eine Methode vorgestellt, mit welcher der Standardmodell-Untergrund aus Daten abgeschätzt werden kann. Mit einer ausgiebigen statistischen Analyse werden sowohl das Entdeckungs- als auch das Ausschlusspotential für den ATLAS SU4-Punkt und zahlreichen weiteren Beispielpunkten im mSUGRA-Parameterraum diskutiert.





# Contents

<b>1</b>	<b>Introduction</b>	<b>5</b>
<b>2</b>	<b>Theoretical background</b>	<b>7</b>
2.1	The Standard Model . . . . .	7
2.1.1	Limitations of the Standard Model . . . . .	7
2.2	Supersymmetry . . . . .	9
2.2.1	Motivation . . . . .	9
2.2.2	The Minimal Supersymmetric Standard Model . . . . .	10
2.2.3	The Minimal Supergravity Model . . . . .	12
2.2.4	Constraints on MSSM and mSUGRA . . . . .	13
2.3	Decay of supersymmetric particles . . . . .	15
2.3.1	Charginos and Neutralinos . . . . .	16
2.3.2	Sleptons . . . . .	17
2.3.3	Squarks . . . . .	17
2.3.4	Gluinos . . . . .	18
2.4	Production of sparticles . . . . .	19
2.5	Supersymmetric signatures . . . . .	19
<b>3</b>	<b>Experimental setup</b>	<b>23</b>
3.1	The Large Hadron Collider (LHC) . . . . .	23
3.2	The ATLAS detector . . . . .	24
3.2.1	The ATLAS coordinate system . . . . .	25
3.2.2	The Inner Detector . . . . .	26
3.2.3	The electromagnetic calorimeter . . . . .	26
3.2.4	The hadronic calorimeter . . . . .	27
3.2.5	The muon system . . . . .	28
3.2.6	Particle visibility . . . . .	28
3.2.7	The trigger system . . . . .	28
3.3	Grid Computing . . . . .	30
3.4	The software framework ATHENA . . . . .	31
3.4.1	Monte-Carlo simulation . . . . .	31
3.4.2	Data formats . . . . .	33

<b>4</b>	<b>Search for <math>l^\pm l^\pm</math> SUSY events</b>	<b>35</b>
4.1	Introduction . . . . .	35
4.2	SUSY benchmark points . . . . .	36
4.3	Sources of Standard Model background . . . . .	36
4.3.1	Top-antitop . . . . .	36
4.3.2	Other Standard Model processes . . . . .	38
4.4	Monte-Carlo-Samples . . . . .	38
4.5	Object definition and reconstruction . . . . .	39
4.5.1	Muon reconstruction . . . . .	39
4.5.2	Electron reconstruction . . . . .	40
4.5.3	Jet algorithm . . . . .	40
4.6	Preselection . . . . .	41
4.6.1	Electrons . . . . .	42
4.6.2	Muons . . . . .	42
4.6.3	Jets . . . . .	42
4.6.4	Spatial Isolation . . . . .	42
4.6.5	Event preselection . . . . .	42
4.6.6	Results . . . . .	43
4.7	Analysis cuts . . . . .	44
4.7.1	Z-Veto . . . . .	45
4.7.2	Transverse mass cut . . . . .	46
4.7.3	Cut on Missing transverse Energy . . . . .	47
4.7.4	Cut on $p_T$ of the leading Jet . . . . .	48
4.8	QCD background . . . . .	52
4.9	Background estimation from data . . . . .	56
4.10	Systematic uncertainties . . . . .	59
4.11	Statistical analysis . . . . .	62
4.11.1	Significance . . . . .	62
4.11.2	Simulation of pseudo-observations . . . . .	63
4.11.3	Analysis of observations . . . . .	64
4.11.4	Uncertainty of the ABCD method . . . . .	65
4.11.5	Testing additional points in the $m_0$ - $m_{1/2}$ -plane . . . . .	69
4.11.6	Exclusion . . . . .	77
4.11.7	Exclusion limit . . . . .	78
<b>5</b>	<b>Summary and Conclusions</b>	<b>83</b>
<b>A</b>	<b>Background Monte-Carlo samples</b>	<b>85</b>
<b>B</b>	<b>Transverse Sphericity</b>	<b>89</b>

# Chapter 1

## Introduction

Our entire universe is determined by the properties and interactions of its most basic constituents: the elementary particles. In the course of time, with increasing technological and scientific progress, a theory emerged, which describes all known elementary particles and three of the four fundamental interactions: the strong, the weak and the electromagnetic interaction. This theory is called the *Standard Model* (SM) of particle physics. Over the decades, the SM has been successfully tested and confirmed by a lot of experiments.

Nevertheless, the SM bears a lot of deficiencies. The solar neutrino problem, for instance, where the measured flux of the solar electron-neutrinos only made up a third of what was expected from the knowledge of the processes inside the sun, could be solved by the so called neutrino-oscillations. But, as a consequence of the oscillations, the neutrinos have a non-zero rest mass, which is not described by the SM.

A much graver impact was the 'discovery' of the so called *Dark Matter* (DM), which is a - still hypothetical - kind of matter that has influence on visible matter via its gravitational forces, but does not interact electromagnetically. The effects of the DM are far from being negligible, as they dominate the dynamics and the formation of galaxies and galaxy clusters. There is no Standard Model particle that can explain the behavior of the DM [53]. The most popular theory to explain the DM and more open questions that can't be answered with the SM, is the so called *Supersymmetry* (SUSY), which is a hypothetical and broken symmetry between matter and forces, i.e. between fermions and bosons. In many SUSY models, the lightest supersymmetric particle is a so-called *Neutralino*, which is a reasonable candidate particle to explain the DM.

With the startup of the Large Hadron Collider (LHC) at CERN near Geneva in November 2009 [39], a new era of experimental physics has begun. With a design center-of-mass energy of  $\sqrt{s} = 14$  TeV [41], the LHC gains access to energy scales never reached before. Many SUSY models predict particles within the reach of the LHC.

This thesis provides a Monte-Carlo based feasibility study for the search for

SUSY events with two leptons in the final state, that have same signs of charge, using the ATLAS detector. The analysis presented here focuses on early LHC data with  $\sqrt{s} = 10$  TeV [42] and an integrated luminosity of 200 pb<sup>-1</sup>.

### Common units for high-energy physics

In physics, usually the SI basic units are used, based on the meter m, the second s, and the kilogram kg.

For particle physics, the usage of the SI units is impractical, as the typical length scales, the masses and the time periods usually are very small. Instead, as a common unit length the femtometer ( 1 fm =  $10^{-15}$  m) is used. The unit energy in particle physics is the electron volt (1 eV =  $1.6 \cdot 10^{-19}$  J), and masses are typically given by  $\frac{GeV}{c^2}$ . To simplify matters, a system of units is used where  $\hbar = c = 1$ .

# Chapter 2

## Theoretical background

### 2.1 The Standard Model

The Standard Model (SM) of particle physics is a gauge theory. It describes all known elementary particles and their fundamental interactions, except gravity. It is based on the  $SU(3)_C \times SU(2)_L \times U(1)_Y$  symmetry [01].

There are three sectors of the SM, characterized by the spins of their particles.

The first sector contains the so-called gauge-bosons, which are spin-1-particles that mediate the interactions between all particles.

The gauge bosons of Quantum-Chromodynamics (QCD) are the eight gluons, which only couple to particles carrying color-charge. The gluons mediate the strong interaction, which is described by the color group  $SU(3)$ .

The gauge bosons of the electroweak interaction are the massless photon ( $\gamma$ ), the two massive charged  $W^\pm$  bosons, and the massive neutral  $Z^0$  boson. The electroweak interaction is a unified description of electromagnetism and the weak force.

Spin- $\frac{1}{2}$ -fermions, the *quarks* and *leptons* make up the second sector of the SM. These particles are grouped into three *generations* with each of them containing two quarks and two leptons. These groups are similar to each other, except the masses of their particles.

Table 2.1 lists the particles of all three generations [03].

The third SM sector contains the spin-0 Higgs boson, or maybe more Higgs bosons, a consequence of the Higgs mechanism. So far, there is no experimental evidence for the existence of a Higgs boson.

#### 2.1.1 Limitations of the Standard Model

The SM, especially its gauge interactions, have been tested with high precision. So far, no measurement could show a significant deviation from the SM predictions.

Fermions	Generation			charge	weak isospin	color charge	lepton number	baryon number
	1st	2nd	3rd					
Leptons	$\nu_e$	$\nu_\mu$	$\nu_\tau$	0	$\pm\frac{1}{2}$	0	$\pm 1$	0
	$e$	$\mu$	$\tau$	$\mp 1$	$\mp\frac{1}{2}$	0	$\pm 1$	0
Quarks	u	c	t	$\pm\frac{2}{3}$	$\pm\frac{1}{2}$	r, g, b	0	$\pm\frac{1}{3}$
	d	s	b	$\mp\frac{1}{3}$	$\mp\frac{1}{2}$	r, g, b	0	$\pm\frac{1}{3}$

Table 2.1: Elementary fermions in the SM and their assigned quantum numbers. The signs refer to fermions (upper sign) and anti-fermions (lower sign).

Nevertheless, the SM leaves several open questions:

- The reason for the electroweak symmetry breaking is still unclear. The favored theory is the existence of a scalar Higgs field, but so far there is no experimental evidence for the consequent Higgs boson.
- Grand Unified Theories predict an energy scale of  $M_{GUT} \approx 10^{16}$  GeV, at which the strong, the weak and the electromagnetic forces are equally strong. The weak energy scale  $M_W \approx 10^2$  GeV is smaller than the GUT scale by orders of magnitudes. This is known as the *hierarchy problem*, being a strong indication for the existence of physics beyond the SM.
- The coupling 'constants' of the three forces in the SM are not really constant, but depend on the energy scale. The electromagnetic coupling increases with energy, whereas the strong and weak coupling decrease with energy. In the SM, the extrapolations of these couplings do not unify at the GUT scale (see Figure 2.1, [32]).
- In the SM, there are several free parameters that can't be derived from theory but have to be fit to experimental data [08].
  - three coupling constants
  - six quark masses
  - six lepton masses
  - four parameters of the CKM matrix
  - one parameter for the strong CP violation
  - one boson mass ( $W^+$  or  $W^-$  or  $Z^0$ )
  - the mass of the Higgs boson

- Quantum corrections from virtual effects of all particles coupling to the Higgs field influence the quadratic Higgs mass. Including the SM into a theory involving a high-energy scale, these loop integrals are regulated by an ultraviolet momentum cutoff  $\Lambda_{UV}^2$ . Assuming that  $\Lambda_{UV}$  is of the order of the Planck scale<sup>1</sup>, the quantum corrections to  $m_H^2$  are about 30 orders of magnitudes larger than  $m_H$  itself. In order to cancel the quadratic divergences, these quantum corrections need an extremely precise fine-tuning [03].
- Gravity is not described by the SM

## 2.2 Supersymmetry

Supersymmetry (SUSY) is a promising theory for new physics on a low-energy scale. It extends the Standard Model and is suitable to reduce some of the SM problems and limitations. SUSY is a new symmetry between bosons and fermions and describes all particles and interactions in one symmetry group.

A SUSY operator transforms a bosonic state into a fermionic state and vice versa, changing the spin by  $\frac{1}{2}$ , so that every Standard Model particle obtains a supersymmetric partner, called *superpartner* of the SM particle. The bosonic superpartners of fermions are called *sfermions* and the fermionic superpartners of the gauge bosons are called *gauginos*. Except from the spin, particles and their superpartners have identical quantum numbers and should also have equal masses [08]. If SUSY exists, the absence of supersymmetric particles indicates a SUSY breaking mechanism by which superparticles gain more mass than their SM partners.

### 2.2.1 Motivation

With SUSY, the Higgs fields gain additional interactions by sparticles, which produce the same quadratic divergences as their SM partners, but with the opposite sign. Thus, the contributions from the SM particles are canceled by the contributions from their superpartners (e.g. squark-loops cancel quark-loops). Therefore, the hierarchy of  $M_W$  and  $M_P$  is preserved and the fine-tuning problem is solved. In Grand Unified Theories (GUTs), the fundamental interactions (strong, weak and electromagnetic) are branches of a single interaction associated with a gauge group, which is broken below an energy scale of  $10^{16}$  GeV. The evolution of these branches, i.e. the three associated coupling constants, is described by the renor-

---

<sup>1</sup> $M_P = 1.2 \cdot 10^{19}$  GeV; this is the energy where gravity becomes comparable to the gauge interactions.

malization group equations.

Within the SM, there is no unification of the gauge couplings. Supersymmetric particles change the running of the coupling constants, so that there is a unification at one point at  $\approx 10^{16}$  GeV. Figure 2.1 shows the running of the inverse coupling constants with and without SUSY [32].

Furthermore, SUSY legitimizes the introduction of scalar Higgs fields due to the connection of spin-0 and spin-1/2 fields, naturally allowing electroweak symmetry breaking [11].

### 2.2.2 The Minimal Supersymmetric Standard Model

The Minimal Supersymmetric Standard Model (MSSM) is the simplest supersymmetric extension of the Standard Model. *Minimal* refers to the number of new particles and interactions.

The MSSM field content consists of all quarks and gauge bosons and their superpartners. Instead of the SM Higgs doublet, there are two chiral Higgs doublets, giving masses to the up- and down-type quarks as well as to the charged leptons. The superpartners of the Higgs bosons are called *Higgsinos*.

In addition, the graviton and its superpartner, the gravitino, are included in the MSSM.

The MSSM doesn't contain interactions violating the baryon- and lepton number (B and L) conservation. Therefore, one can define a new multiplicative parity for a particle with spin S [08]:

$$R = (-1)^{3B-3L+2S} \quad (2.1)$$

This R-parity distinguishes SM particles ( $R = +1$ ) from their MSSM superpartners ( $R = -1$ ) [05]. R-Parity conservation determines the SUSY phenomenology and predicts that the interactions of supersymmetric particles are the same as in the SM. For processes with SM particles as initial state, supersymmetric particles can only be produced in even numbers. In addition, the lightest supersymmetric particle (LSP) is stable, as by definition there are no lighter supersymmetric particles the LSP can decay into, and the decay into SM particles is forbidden by R-Parity conservation.

If the LSP only interacts weakly with matter, and especially does not contain electromagnetic charge, it behaves like a heavy and stable neutrino [09], being the prime candidate for the cold dark matter (CDM), which is needed for most cosmological models and for galaxy formation and has strong experimental evidence.

Table 2.2.2 shows the eigenstates of the MSSM particles.

Particle		spin	sparticle		spin
left-handed quarks	$q_{L,rgb}$	$\frac{1}{2}$	"left" squarks	$\tilde{q}_{Lrgb}$	0
right-handed quarks	$q_{R,rgb}$	$\frac{1}{2}$	"right" squarks	$\tilde{q}_{Rrgb}$	0
left-handed leptons	$l_L$	$\frac{1}{2}$	"left" sleptons	$\tilde{l}_L$	0
right-handed leptons	$l_R$	$\frac{1}{2}$	"right" sleptons	$\tilde{l}_R$	0
gluons	$g$	1	gluinos	$\tilde{g}$	$\frac{1}{2}$
W boson	$W^\pm$	1	charginos	$\tilde{\chi}_{1,2}^\pm$	$\frac{1}{2}$
charged Higgs	$H^\pm$	0			
photon	$\gamma$	0	neutralinos	$\tilde{\chi}_{1-4}^0$	$\frac{1}{2}$
Z boson	$Z^0$	1			
neutral Higgs	$H^0, h^0, A^0$	0			
graviton		2	gravitino		$\frac{3}{2}$

Table 2.2: The MSSM mass eigenstates

The gauginos and higgsinos are massive and mix to form the neutralinos and the charginos. From the eight degrees of freedom in the two Higgs doublets three are absorbed to give the  $W^\pm$  and the  $Z^0$  their masses, to that five physical Higgs bosons are left.

The MSSM Lagrangian consists of the SUSY Lagrangian from theory and a breaking term [07]:

$$L_{MSSM} = L_{SUSY} + L_{break} \quad (2.2)$$

$L_{break}$  violates Supersymmetry and is chosen to contain only masses and couplings which preserve the given hierarchy, as well as to preserve the cancellation of quadratic divergences. The terms in  $L_{break}$  are called *soft-breaking* terms [10].

The SUSY conserving term  $L_{SUSY}$  contains the particles and couplings of the SM, i.e. the three gauge couplings, one Higgs mass parameter ( $\mu$ ) and Higgs-fermion Yukawa coupling constants corresponding to the coupling of quarks, leptons, squarks and sleptons to the Higgs and higgsinos [07].

The SUSY breaking term contains the gaugino masses ( $M_{U_1}$ ,  $M_{SU_2}$  and  $M_{SU_3}$ ), trilinear scalar couplings, mass terms for left- and right-handed spin-0 fields, and three scalar Higgs mass parameters ( $m_{H_u}^2, m_{H_d}^2$  and the B term).

The number of all soft-breaking terms, i.e. free parameters of the model, is 106 [01]. By imposing SUSY breaking constraints at a high energy scale, this

number can be strongly reduced.

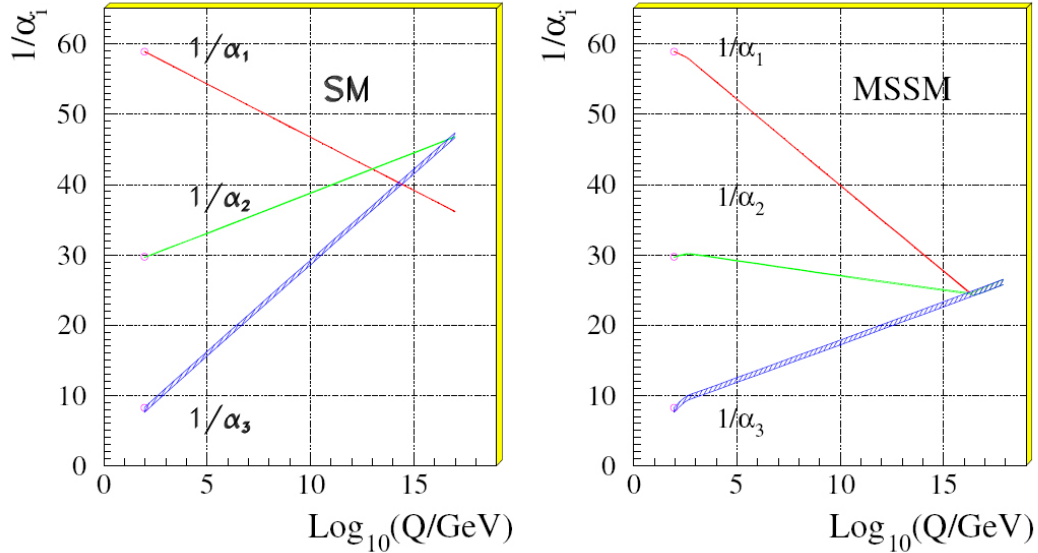


Figure 2.1: The dependence of the inverse couplings on the energy scale in the Standard Model (left) and in the MSSM (right) [32]

### 2.2.3 The Minimal Supergravity Model

The minimal supergravity model (mSUGRA) is a supersymmetric model including gravity. In mSUGRA, which is a GUT model, the symmetry breaking mechanism is similar to the Higgs mechanism, leaving only few free parameters of SUSY breaking. A common low-energy SUSY breaking scenario is called the *hidden sector* scenario, where two sectors, the *visible* and the *hidden* sector, are assumed to exist. The former is the sector the SUSY breaking is submitted to. It contains all MSSM particles. In the hidden sector, in contrast, the spontaneous SUSY breaking occurs via a Higgs mechanism, and the breaking is mediated to the visible sector by gravity [10].

The soft-breaking terms of the MSSM Lagrangian only contain five independent SUSY breaking parameters. Usually, the scale for which these parameters are specified is chosen to be the GUT scale. Fixing these parameters defines the MSSM masses and couplings at the electroweak scale. The radiative corrections to the masses and couplings can distort the Higgs potential and result in the breaking mechanism of the electroweak gauge symmetry, conserving color charge and electromagnetic charge.

The five mSUGRA parameters are [10]:

- $m_0$ : a scalar mass parameter, that determines the sfermion (spin-0) masses and the Higgs squared-mass parameters
- $m_{\frac{1}{2}}$ : a gaugino mass parameter, that determines the gaugino (spin- $\frac{1}{2}$ ) masses
- $A_0$ : a trilinear interaction parameter
- $\tan(\beta)$ : the ratio of the VEVs of the two Higgs fields
- $\text{sgn}(\mu)$ : the sign of the Higgs mass parameter  $\mu$

Their corresponding low-energy values can be calculated by using renormalization group evolution.

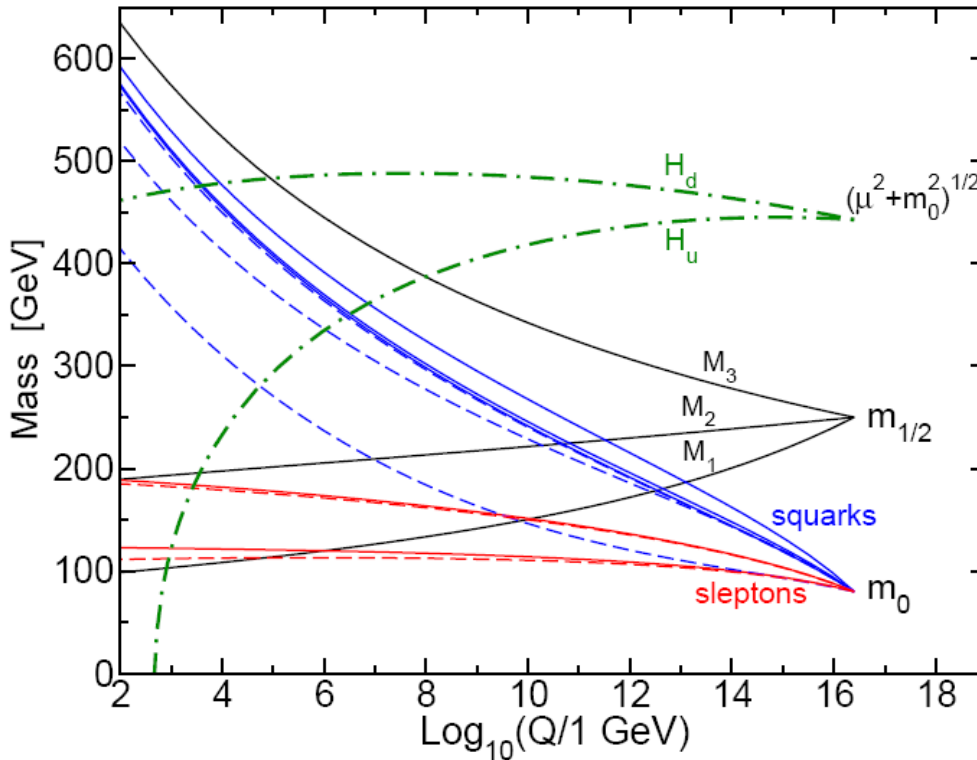


Figure 2.2: RG evolution of the  $m_0$  and  $m_{\frac{1}{2}}$  mass parameters in the MSSM with typical mSUGRA boundary conditions [11]

### 2.2.4 Constraints on MSSM and mSUGRA

Previous and currently running experiments, e.g. Tevatron and LEP, could not provide any experimental evidence for SUSY. However, lower mass limits for supersymmetric particles could be determined. For example, there is a lower mass

limit for charginos of  $m_{\chi_{\pm}} \geq 103.5$  GeV, provided by chargino searches at LEP [40]. The most important constraints on the squark and gluino masses are provided by Tevatron [08] and depend on the ration of squark- and gluino masses.

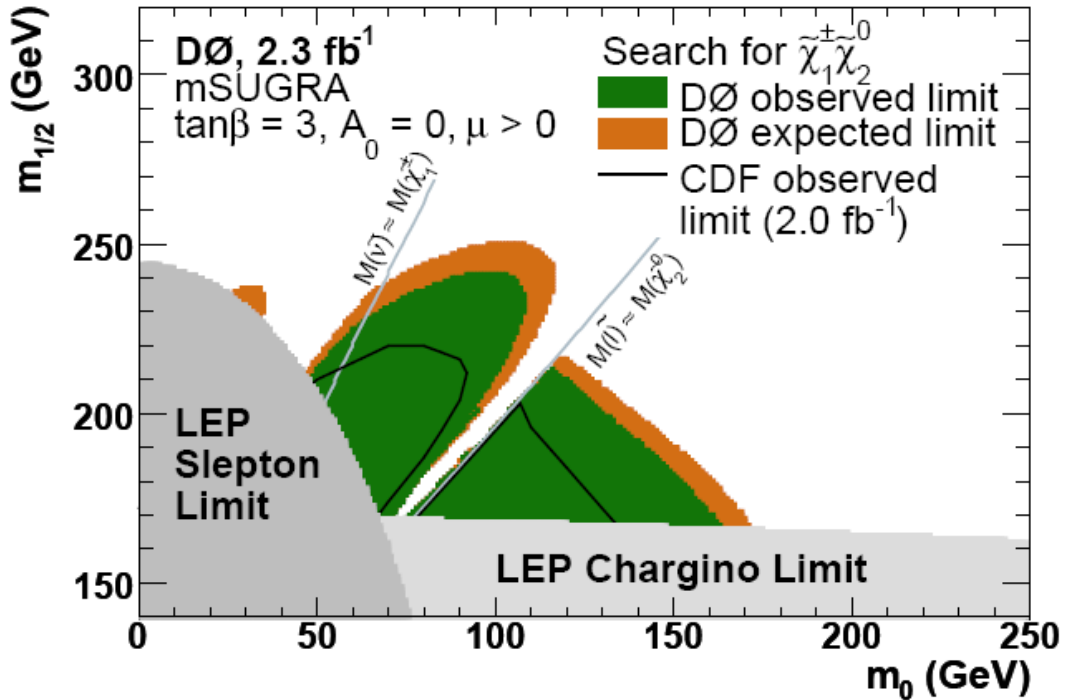


Figure 2.3: Region in the  $m_0$ - $m_{1/2}$ -plane excluded by the combination of the D0 analyses (green), by LEP searches for charginos (light gray) and sleptons (dark gray) and CDF (black line) [45]

Cosmological measurements and indirect observations of dark matter suggest a color-neutral and electromagnetic neutral and stable lightest supersymmetric particle. Recent measurements from the satellite experiment WMAP [36], which was employed to explore the cosmic microwave background, have shown that our universe contains a large and significant amount of dark matter. The relic density of a non-charged LSP that was produced in great quantities in the early universe and has been reduced by pair annihilation, is a good explanation for the observed dark matter density distribution. WMAP measurements yield an upper limit for the relic LSP density. A lower limit is not reasonable, as the LSP might not be the only explanation for dark matter.

For a part of the mSUGRA parameter space, the Higgs potential is not capable of causing electroweak symmetry breaking, as the square-mass term of the

Higgs potential remains positive. This region is therefore excluded by theory.

Figure 2.4 [30] shows the mSUGRA  $m_0$ - $m_{1/2}$ -plane for fixed values of  $\tan(\beta)$ ,  $\text{sgn}(\mu)$ ,  $m_H$  and  $m_t$ .

In the pink area, the stau ( $\tilde{\tau}$ ) is the LSP, which carries electromagnetic charge and is therefore no dark matter candidate.

In the green area, despite the lightest neutralino is the LSP, the relic density is too large to explain the dark matter observations.

In the red area, no electroweak symmetry breaking takes place.

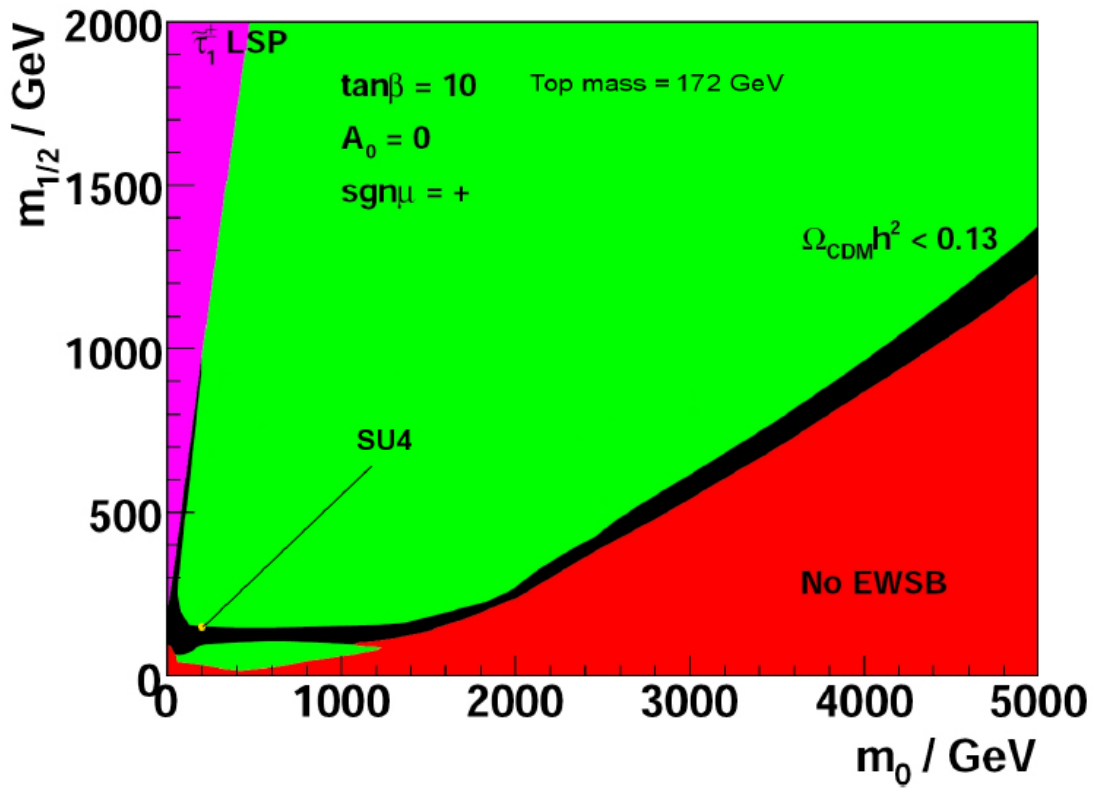


Figure 2.4: The mSUGRA  $m_0$ - $m_{1/2}$ -plane with its allowed and forbidden regions for a given set of parameters [30]

## 2.3 Decay of supersymmetric particles

This section contains an overview of possible decays of supersymmetric particles. It is assumed that the lightest Neutralino is the LSP and that the R-parity is

conserved.

### 2.3.1 Charginos and Neutralinos

Charginos and Neutralinos usually contain contributions from the electroweak gauginos, i.e.  $\tilde{W}^{\pm,0}$  and  $\tilde{B}$ , and thus inherit couplings of weak interaction to scalar fermion-sfermion pairs, as shown in Figure 2.5. Therefore, Charginos and Neutralinos can decay into lepton+slepton or quark+squark, unless sleptons and squarks are too massive [11].



Figure 2.5: Couplings of Wino and Bino to fermion-sfermion pairs

Furthermore, charginos and neutralinos can decay into lighter charginos/neutralinos and a Higgs boson or an electroweak gauge boson.

The most important two-body decay modes for charginos and neutralinos are:

- $\tilde{\chi}_i^0 \rightarrow Z^0 + \tilde{\chi}_j^0$
- $\tilde{\chi}^\pm \rightarrow W^\pm + \tilde{\chi}^0$
- $\tilde{\chi}^0 \rightarrow W^\pm + \tilde{\chi}^\pm$
- $\tilde{\chi}_i^\pm \rightarrow Z^0 + \tilde{\chi}_j^\pm$
- $\tilde{\chi}_i^0 \rightarrow h^0 + \tilde{\chi}_j^0$
- $\tilde{\chi}_i^\pm \rightarrow h^0 + \tilde{\chi}_j^\pm$
- $\tilde{\chi}_i^0 \rightarrow l + \tilde{l}$
- $\tilde{\chi}_i^\pm \rightarrow l + \tilde{\nu}$
- $\tilde{\chi}_i^0 \rightarrow \nu + \tilde{\nu}$
- $\tilde{\chi}_i^\pm \rightarrow \tilde{l} + \nu$

If these two-body modes are kinematically forbidden for certain charginos or neutralinos, the latter have a three-body decay, e.g.:

- $\tilde{\chi}_i^0 \rightarrow f + f + \tilde{\chi}_j^0$
- $\tilde{\chi}^\pm \rightarrow f + f' + \tilde{\chi}^0$
- $\tilde{\chi}^0 \rightarrow f + f' + \tilde{\chi}^\pm$
- $\tilde{\chi}_2^\pm \rightarrow f + f + \tilde{\chi}_1^\pm$

Here,  $f$  denotes a lepton or a quark.  $f$  and  $f'$  are different members of the same  $SU(2)_L$ -multiplet.

Phenomenologically, especially the following decays are important:

- $\tilde{\chi}_1^\pm \rightarrow l + \nu + \tilde{\chi}_1^0$
- $\tilde{\chi}_2^0 \rightarrow l + l + \tilde{\chi}_1^0$

### 2.3.2 Sleptons

Sleptons can have two-body decays into a lepton plus a chargino or a neutralino, i.e.

- $\tilde{l} \rightarrow l + \tilde{\chi}^0$
- $\tilde{\nu} \rightarrow \nu + \tilde{\chi}^0$
- $\tilde{l} \rightarrow \nu + \tilde{\chi}^\pm$
- $\tilde{\nu} \rightarrow l + \tilde{\chi}^\pm$

Usually, direct decays into the LSP are kinematically allowed, as long as the LSP is the lightest neutralino:

- $\tilde{l} \rightarrow l + \tilde{\chi}_1^0$
- $\tilde{\nu} \rightarrow \nu + \tilde{\chi}_1^\pm$

Right- and left-handed sleptons have different preferred decay modes. The right-handed sleptons prefer the direct decay into the LSP if the latter is bino-like. The left-handed sleptons, in contrast, prefer the decay into the lightest chargino or the next-to-lightest neutralino if these gauginos have enough contribution from wino.

### 2.3.3 Squarks

The dominant decay mode of a squark is  $\tilde{q} \rightarrow q + \tilde{g}$  as it has a strong interaction vertex [11] (see Figure 2.6).

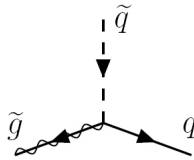


Figure 2.6: The coupling of squarks, quarks and gluinos

In addition, squarks can decay into a quark plus a chargino or a neutralino:

- $\tilde{q} \rightarrow q + \tilde{\chi}^0$
- $\tilde{q} \rightarrow q' + \tilde{\chi}^\pm$

Again, left- and right-handed squarks prefer different decay modes. For right-handed squarks the direct decay into the LSP is preferred, whereas left-handed squarks prefer decays into the light charginos and the heavier neutralinos.

### 2.3.4 Gluinos

Gluinos decay into squark-quark pairs ( $\tilde{g} \rightarrow q + \tilde{q}$ ). If the squarks are too heavy, the gluinos decay into quark-pairs plus a chargino or a neutralino [11]. The consecutive decays of the gluino products can yield a variety of long decay chains.

## 2.4 Production of sparticles

Most collisions at the LHC are gluon-gluon collisions and quark-gluon collisions. The most important production modes for supersymmetric particles are strong interaction processes [11]:

- $g + g \rightarrow \tilde{g} + \tilde{g}$
- $g + q \rightarrow \tilde{g} + \tilde{q}$
- $g + g \rightarrow \tilde{q}_i + \tilde{q}_j$

Nevertheless, parton collisions of all types can occur, e.g. gluino- or squark pair production by quark-quark annihilation. Weak interaction can yield a direct production of charginos and neutralinos or even sleptons from quark-quark reactions. Figure 2.7 shows Feynman graphs for the most important production channels [11].

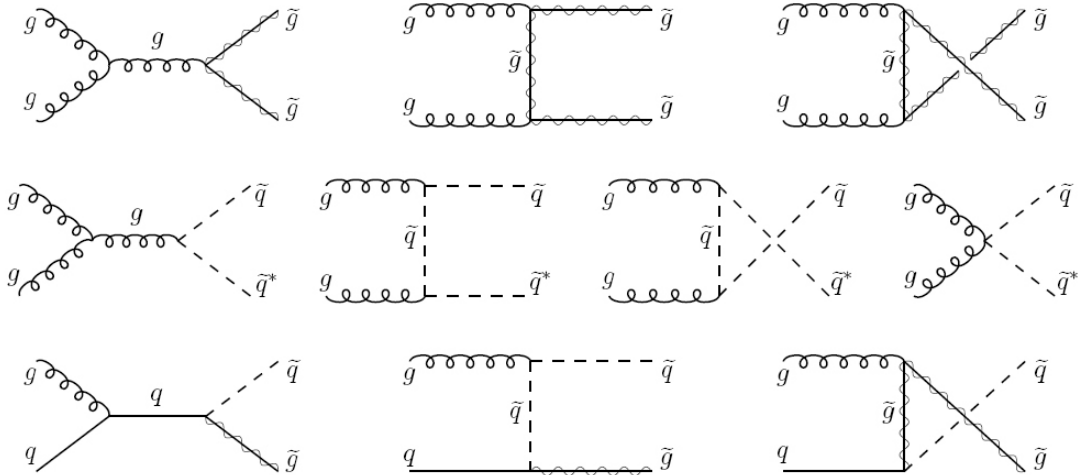


Figure 2.7: Sparticle production by gluon-gluon- and quark-gluon reactions

## 2.5 Supersymmetric signatures

Because of R-parity conservation, supersymmetric particles are produced in pairs. Each of these sparticles has consecutive decays, which end as soon as a LSP is produced with an additional SM particle. The LSPs leave the detector without interaction and carry away energy. At the LHC, the total energy of an event is not known, so that the missing energy can only be determined by vectorially adding up the momenta of all objects. ATLAS can only measure the momentum components that are perpendicular to the beam axis. Hence, the measurement

of the missing energy is restricted to the transverse component, the so called *missing transverse energy*,  $E_T^{\text{miss}}$ .

Note that a back-to-back configuration of not-interacting particles can yield low values for  $E_T^{\text{miss}}$ .

Supersymmetric events with squarks and/or gluinos have quarks in their decay chains, and hence jets are a common SUSY signature, too.

All lepton multiplicities can occur in supersymmetric events, offering a variety of distinct channels for analysis. Especially event types that rarely occur in Standard Model processes are of great interest, for instance events with two leptons in the final state that contain same signs of charge.

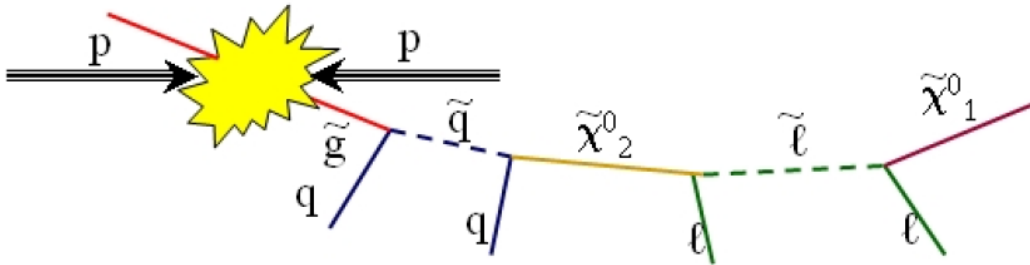


Figure 2.8: An typical supersymmetric cascade decay [30]

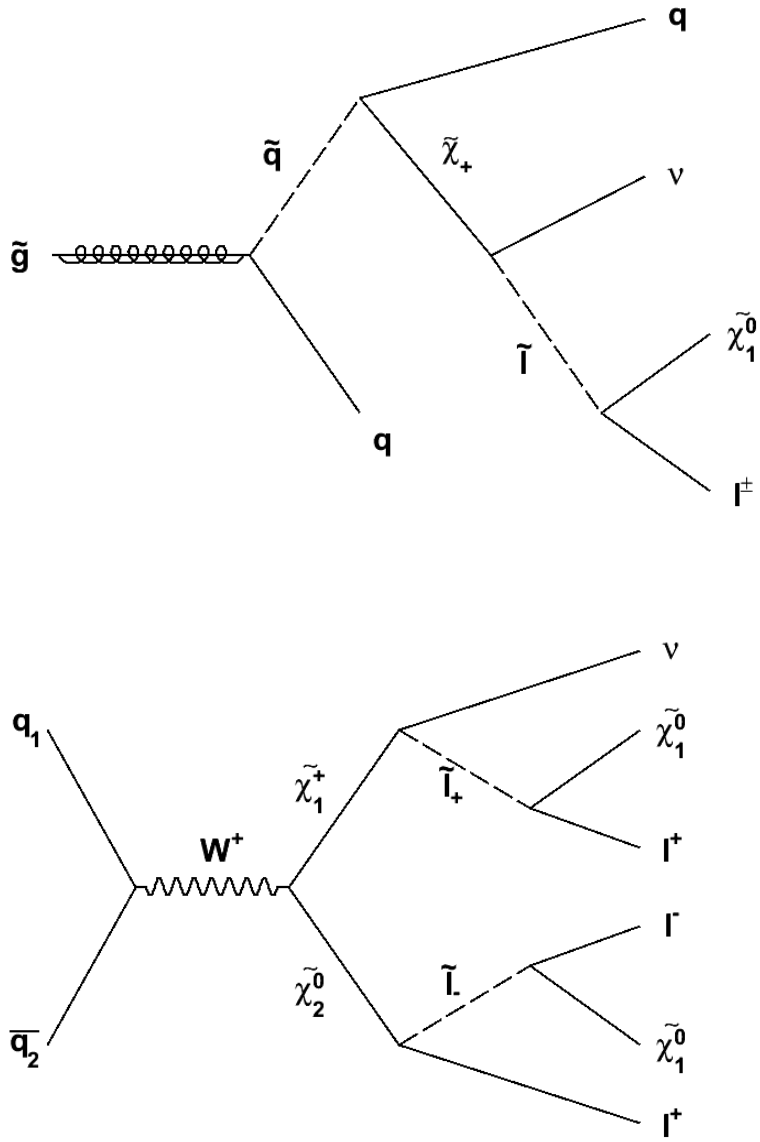


Figure 2.9: An example for a gluino cascade decay (upper) and the direct chargino-neutralino-production (lower)



# Chapter 3

## Experimental setup

### 3.1 The Large Hadron Collider (LHC)

The new particle accelerator at CERN (European Organization for Nuclear Research) is the successor of the former collider experiment LEP (Large Electron-Positron Collider) in the same tunnel with a circumference of about 27 km. In LEP, collisions took place from 1989 to 2000. Its center-of-mass energy  $\sqrt{s} \approx 200$  GeV was limited by synchrotron radiation [50]. This will not be the case at the LHC, where protons are accelerated in two oppositely circulating beams and brought to collision at a design center-of-mass energy of  $\sqrt{s} = 14$  TeV [41]. Due to the comparatively high proton mass, energy loss by synchrotron radiation is negligible there. In return, new difficulties arise from the fact that protons are composite particles. The center-of-mass energy of the LHC is mainly constrained by the performance of the superconducting beam bending magnets.

Predominantly, the aim of the LHC is the discovery of new physics, e.g. the Higgs boson(s), supersymmetric particles or leptoquarks. Therefore, many analyses are event counting experiments, that require a sufficiently high statistical significance, i.e. a large integrated luminosity. The luminosity is defined as:

$$L = \frac{n^2 f}{4\pi\sigma} \quad (3.1)$$

where  $n$  is the number of particles (bunch size) per beam,  $f$  is the frequency and  $\sigma$  is the cross-section of the beam. The integrated luminosity is then:

$$L_{int} = \int L \cdot dt \quad (3.2)$$

The cross-section is a quantity describing the probability for an interaction between two particles. A common unit for the cross section is the *barn*  $b$ , where  $1b = 10^{-24} \text{ cm}^2$ .

At the LHC, the high design luminosity of  $10^{34} \frac{1}{\text{cm}^2\text{s}}$  is achieved by collimating the proton beams into thin bunches of  $r \approx 15 \mu\text{m}$ , each of them containing  $N_i \approx$

$10^{11}$  protons. Bunches cross every 25 ns [41].

During the first years of LHC collisions, the luminosity will be one order of magnitude lower than the design luminosity.

The bunch crossings can occur at different points of the LHC. At these points, the following particle detectors are positioned: ATLAS, CMS, ALICE, LHCb, TOTEM and LHCf. Figure 3.1 shows an overview of the LHC with its experiments. The two largest experiments are ATLAS and CMS (Compact Muon Solenoid). Both of them are designed to cover a wide range of physics scenarios.

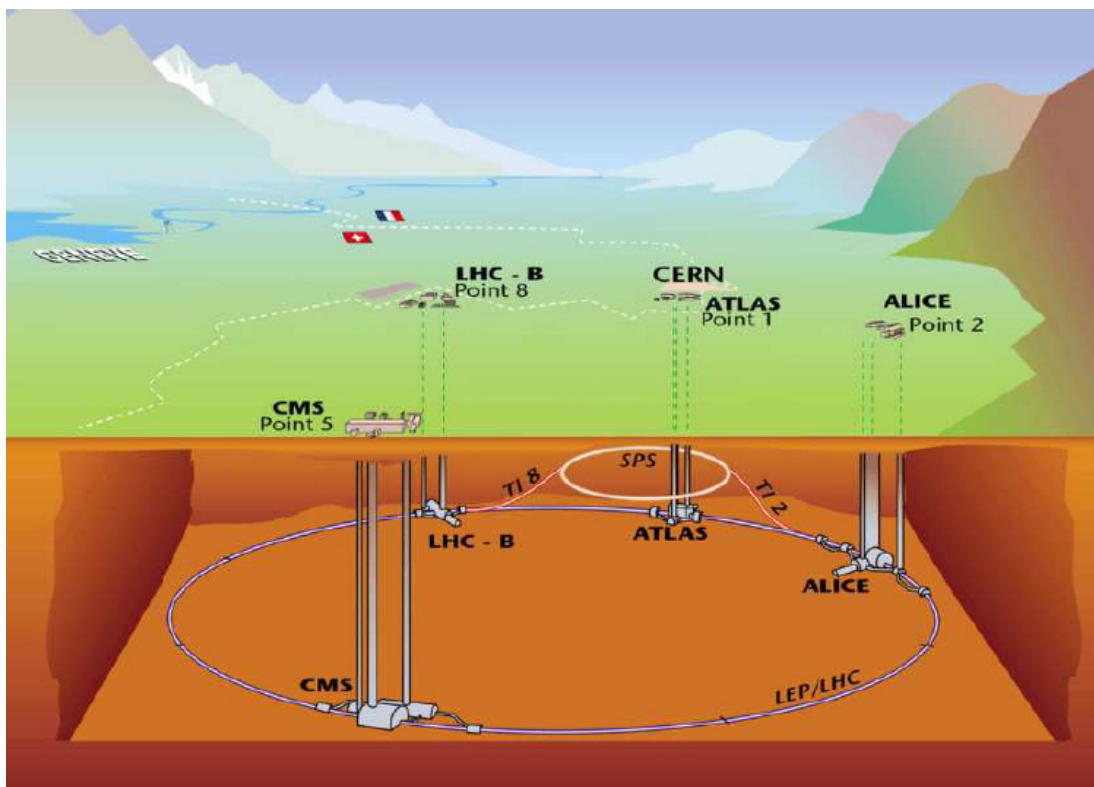


Figure 3.1: The LHC at CERN with some experiments

In the following, the ATLAS detector will be described in detail.

## 3.2 The ATLAS detector

The ATLAS (A Toroidal LHC ApparatuS) detector is a classical universal particle detector for collider experiments. It consists of several cylindrical subdetectors with a concentric arrangement around the LHC's beam axis. The innermost detector is the inner track detector, followed by the electromagnetic calorimeter,

the hadronic calorimeter and the muon detector system. The inner detector is embedded in a solenoid magnet, the muon system is inside a large toroidal magnet. Each subdetector consists of a barrel region and two endcap regions. In total, ATLAS has a length of 46 m, a diameter of 25 m and a mass of about  $7 \cdot 10^6$  kg.

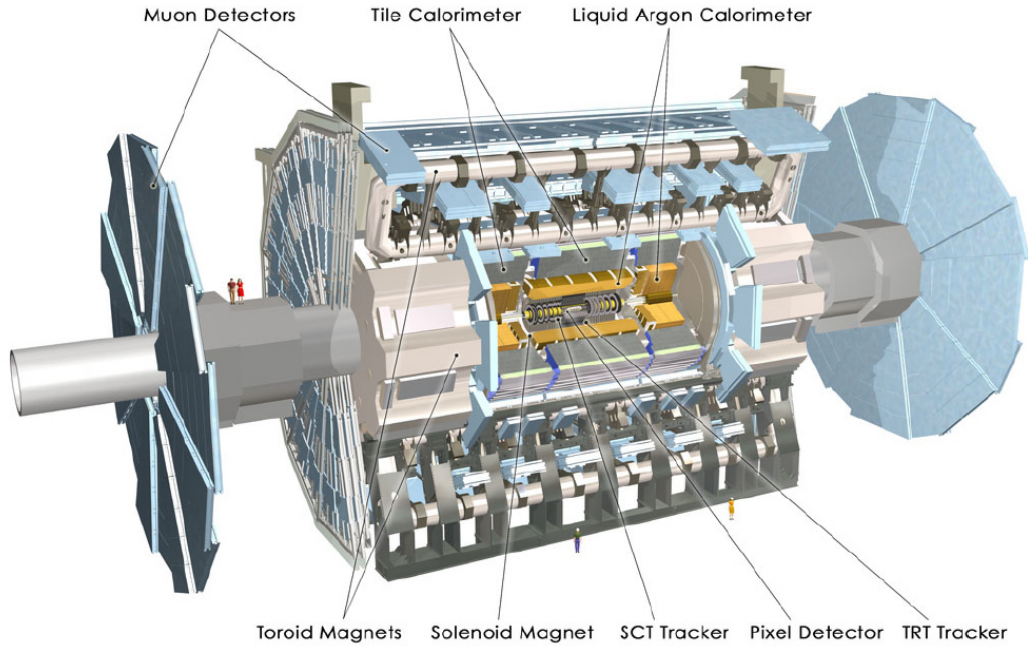


Figure 3.2: The ATLAS detector

### 3.2.1 The ATLAS coordinate system

The ATLAS x-axis is defined to be perpendicular to the beam-axis and to point towards the center of the LHC. The y-axis is also perpendicular to the beam-axis and points upwards. The z axis is the beam axis, with positive numbers according to a right-handed Cartesian coordinate system.

Furthermore, the cylindrical shape suggests the use of cylindrical coordinates, i.e. an azimuthal angle  $\phi$ , a polar angle  $\theta$  and a radius  $r$ . Instead of  $\theta$ , defined by  $\tan(\theta) = \frac{\sqrt{x^2+y^2}}{z}$ , the pseudorapidity  $\eta$  is used. The latter is defined as

$$\eta = -\log\left(\tan\left(\frac{\theta}{2}\right)\right) \quad (3.3)$$

which is in a good approximation additive with respect to a Lorentz boost in the z-direction.

The distance  $\Delta R$  in the  $\eta$ - $\phi$ -plane is defined as

$$\Delta R = \sqrt{\Delta\eta^2 + \Delta\phi^2} \quad (3.4)$$

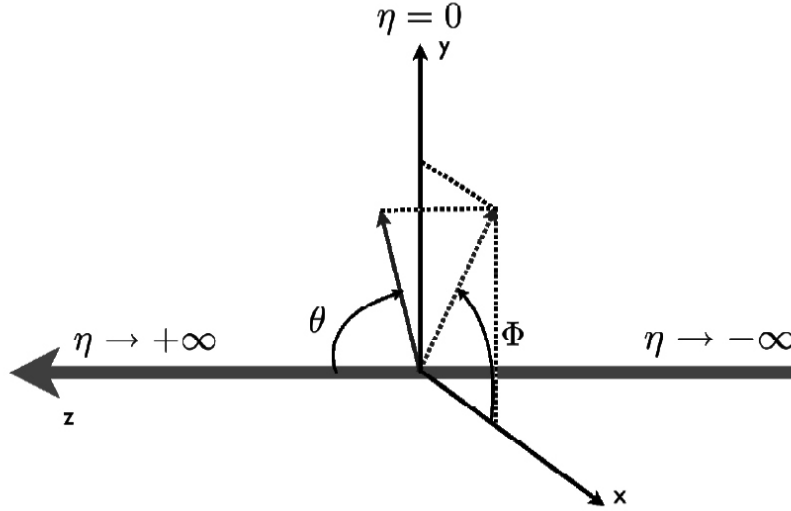


Figure 3.3: The ATLAS coordinate system

### 3.2.2 The Inner Detector

The Inner Detector (ID) consists of the Silicon Pixel Detector, the Semiconductor Tracker (strip sensors) and the Transition Radiation Tracker (gas detector), where the latter provides a good separation of pions from electrons.

The aim of the Inner Detector is the precise reconstruction of the tracks of the charged particles, in order to calculate the momenta from the curvatures of the tracks and the strength of the magnetic field.

The Inner Detector is placed closely to the LHC's beam axis and is surrounded by the solenoid magnet.

Geometrically, the Inner Detector's range is limited to  $|\eta| < 2.5$ .

### 3.2.3 The electromagnetic calorimeter

The aim of the electromagnetic calorimeter (ECAL) is to measure the energy of electromagnetic interacting particles, mainly electrons, positrons and photons. It absorbs and detects the showering particles. Muons and charged hadrons are comparatively massive and usually lose only a small fraction of their energy in the ECAL.

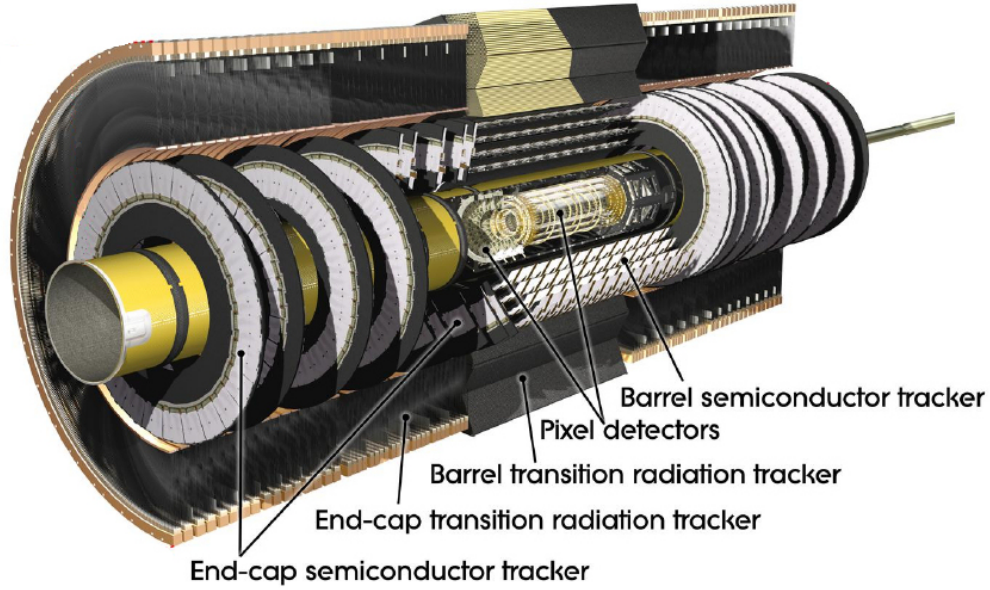


Figure 3.4: The ATLAS Inner Detector

The ECAL consists of consecutively arranged layers of lead as an absorber material and liquid argon as an active material.

Geometrically, the ECAL's range is limited to  $|\eta| < 3.2$ .

The spatial resolution is  $\Delta R_{min}^2 = 0.025^2$ , the energy resolution is

$$\frac{\Delta E}{E} \approx \frac{0.1}{\sqrt{\frac{E}{[GeV]}}} \oplus 0.01 \quad (3.5)$$

### 3.2.4 The hadronic calorimeter

The hadronic calorimeter (HCAL) surrounds the electromagnetic calorimeter. Its aim is to measure the energy of hadrons, both charged and neutral. Their energy is absorbed by hadronic showers which are caused by strong interactions with the absorber material. The HCAL's geometrical range is limited to  $|\eta| < 3.2$ .

The spatial resolution is  $\Delta R_{min}^2 = 0.1^2$  for  $|\eta| < 2.5$  and  $\Delta R_{min}^2 = 0.2^2$  for  $2.5 < |\eta| < 3.2$ .

The energy resolution of the HCAL is

$$\frac{\Delta E}{E} \approx \frac{0.5}{\sqrt{\frac{E}{[GeV]}}} \oplus 0.03 \quad (3.6)$$

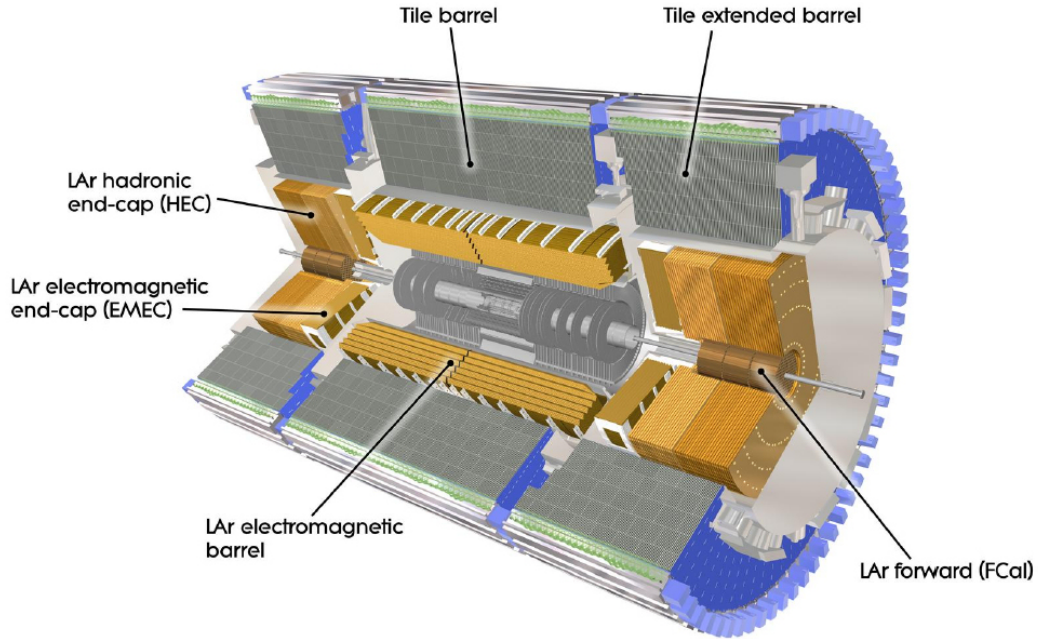


Figure 3.5: The ATLAS calorimeter system

### 3.2.5 The muon system

Outside the calorimeter system is the muon spectrometer (MS). Its aim is to precisely measure the energy of the muons. It consists of three layers of monitored drift tube chambers (MDT) and additional cathode strip chambers for high  $\eta$  values.

The energy resolution ranges from 10% up to 4%, depending on the transverse momenta of the muons.

Usually, only muons can reach the MS (both muons from collisions and from cosmics), but in rare cases, soft particles from calorimeter showers can reach the innermost parts of the MS.

### 3.2.6 Particle visibility

Table 3.1 shows a list of stable particles and the ATLAS subdetectors in which these particles are visible [35]. Note that neutrinos can escape ATLAS without being detected. Figure 3.7 shows a cross-section of the ATLAS detector detecting a variety of particles.

### 3.2.7 The trigger system

The design bunch crossing rate at the LHC is 40 MHz. This is far beyond the technical possibilities of recording and storing. Therefore the ATLAS detector

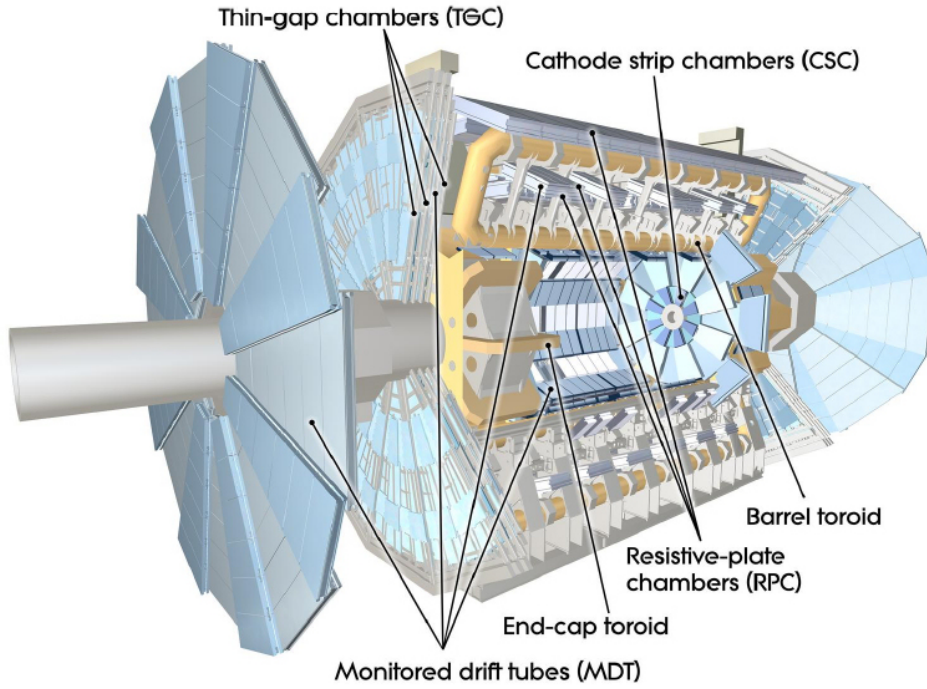


Figure 3.6: The ATLAS muon system

Particle	Subdetector
Electron	ID, ECAL
Muon	ID, MS
Charged Hadrons	ID, HCAL
Neutral Hadrons	HCAL
Photons	ECAL

Table 3.1: List of stable particles and the corresponding sensitivity of the ATLAS subdetectors

has to distinguish between processes that are of physical interest and those that are not.

The ATLAS trigger system consists of three hierarchically arranged subsystems: the Level One Trigger, the Level Two Trigger, and the Event Filter.

The Level One trigger is a hardware trigger. It divides each event into regions of interest (ROI). The events are filtered using low-resolution information from the calorimeter system and from the faster part of the muon system. All data passing the Level One Trigger is passed to the Level Two trigger in a pipeline

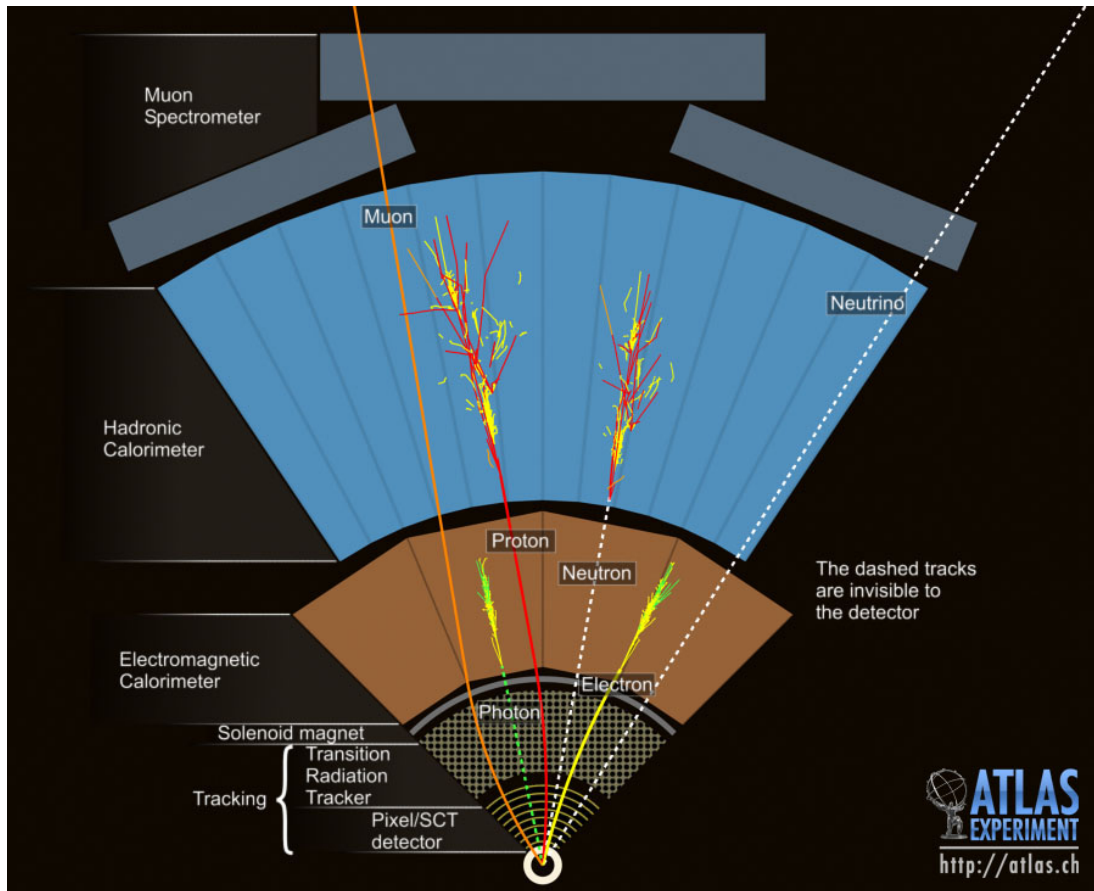


Figure 3.7: Particle detection in ATLAS

stream with an expected event rate of 75 kHz.

The Level Two trigger is a software trigger, which filters the events using information from the Inner Detector and from all previously defined regions of interest. The average event rate is reduced to 1 kHz.

The Event Filter is again a software trigger. It finally decides whether the event is rejected or permanently stored. The expected average event rate is 100 Hz.

### 3.3 Grid Computing

The LHC with its enormous design luminosity will produce roughly  $1.5 \cdot 10^{16}$  bytes per year. This huge amount of information has to be stored and accessed by thousands of physicists with a variety of analysis programs.

Therefore, a new data storage and analysis infrastructure is needed. The Worldwide LHC Computing Grid is a global collaboration of more than 170 computing centers (sites) in 34 countries. It provides more than 100,000 processors.

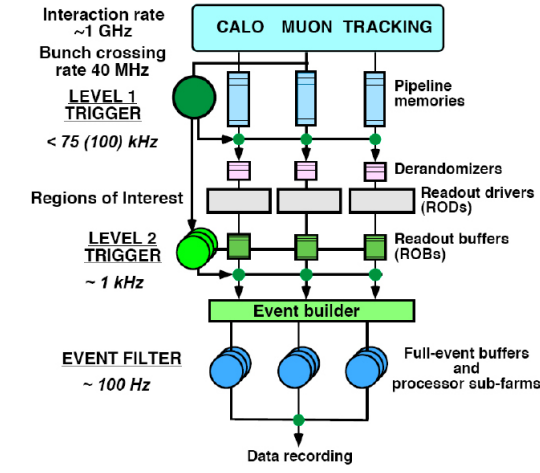


Figure 3.8: The ATLAS trigger system

The network is built up in TIER layers (see image 3.9).

The TIER-0 center is located at CERN. It contains all of the ATLAS datasets and will do the first data processing and subsequent distributing to the other TIER sites.

The TIER-1 centers are responsible for the different regions in the world, e.g. the US or Germany. Their aim is to store, distribute and process data.

The TIER-2 centers are smaller than the TIER-1 centers. Their aim is to perform the large physics jobs, i.e. analyses and MC production, and to store some datasets [38] [34].

## 3.4 The software framework ATHENA

ATHENA is a multi-purpose software framework for ATLAS. It is able to control the Monte-Carlo simulation of physics processes by other programs, e.g. PYTHIA, and the simulation of the detector response for these generated events by GEANT. Furthermore, it is a powerful tool for the analysis of artificial and real ATLAS data.

ATHENA consists of C++ programs and PYTHON scrips and is based on the software framework GAUDI [47].

### 3.4.1 Monte-Carlo simulation

Simulated events are used to prepare the analysis of real data. If the aim of an analysis is the discovery or exclusion of new physics, the analysis can be designed as a counting experiment. With Monte-Carlo (MC) data, the number of observed

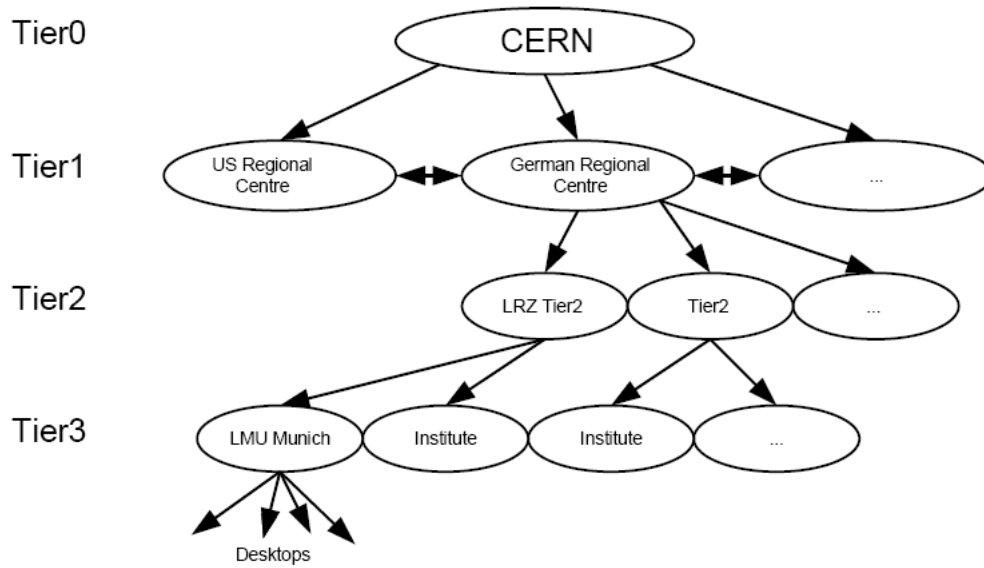


Figure 3.9: The structure of the LHC computing grid

background events, usually all kinds of Standard Model processes, can be estimated. With real data, the physicist might (or might not) observe more events than the MC prediction for the background, and then has to decide whether this excess is significant or not. In addition, if MC samples with the new physics processes are available, filter programs can be designed to improve the signal-to-background ratio. These programs accept or reject events depending on a variety of event parameters, like for instance angles between article jets or the momenta of certain particles.

The chain of the production of MC events consists of the following steps:

- Generation: a physics event is generated by a Monte-Carlo generator program, with vertices and 4-vectors of all particles of this event
- Simulation: the interactions of the particles of an event with the detector material are calculated along the particle tracks, with a minimum step width of at least  $20 \mu\text{m}$
- Digitization: the response of the detector components on the simulated interactions is calculated
- Reconstruction: the tracks of the particles are reconstructed and particles are identified

### 3.4.2 Data formats

There is a variety of data formats used for ATLAS analysis. In this subsection, the most important data formats will be briefly presented [48].

#### RAW

The *Raw Bytestream Data* (RAW) directly comes from the ATLAS triggers and online event reconstruction. This format contains very detailed event information. Each event needs about 1.6MB of disk space and is stored at CERN.

#### ESD

The *Event Summary Data* (ESD) is derived from RAW data by an offline reconstruction software. Each event needs about 500kB of storage. The ESDs have an object-oriented representation. Usually, ESDs are only used for calibration or for the analysis of reconstruction algorithms.

#### AOD

The *Analysis Object Data* (AOD) is derived from ESDs and contains only information needed for most physics analyses. In the AOD format, each event needs about 100kB of storage. The AODs have, like the ESDs, an object-oriented representation.

#### DPD

The *Derived Physics Data* (DPD) is derived from AODs, comprising a further data reduction. Usually, only a fraction of the events and/or a fraction of the events from an AOD are stored into a DPD. A special type of DPD is the so called *D3PD* with an own, table-like data structure (a so called *ntuple*) that is easily accessible from the ROOT framework. The D3PD format is the most convenient data format to work with.

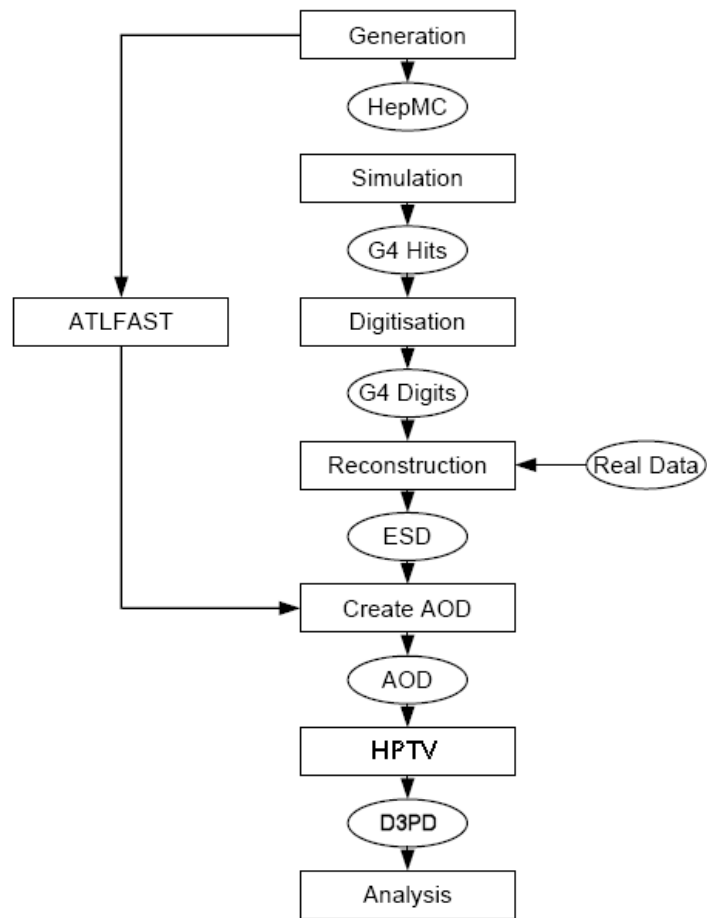


Figure 3.10: The full analysis chain for ATLAS Monte-Carlo data and real data in the ATHENA framework

# Chapter 4

## Search for $l^\pm l^\pm$ SUSY events

### 4.1 Introduction

This analysis focuses on the search for supersymmetric events with two charged leptons in the final state that contain the same sign of charge, i.e.  $e^\pm + e^\pm + X$ ,  $\mu^\pm + \mu^\pm + X$  and  $e^\pm + \mu^\pm + X$ . Additional leptons are allowed, but not required. In SUSY events, charged leptons are produced in slepton decays or by chargino and neutralino decays. Gluinos or squarks are produced in pairs due to R-parity conservation. Their decay chains can contain charginos and neutralinos, which can further decay into final states containing leptons. This is an efficient source of same-sign lepton pairs as well as other multilepton final states. Also, a direct chargino-neutralino production is a source of dilepton and trilepton final states [26], [28] [44]. Figure 2.5 shows a typical decay chain for a gluino and a multilepton final state from a direct chargino-neutralino-production. The decay of squarks and gluinos produces energetic jets. The neutrinos and the lightest neutralinos, where the latter are assumed to be the lightest supersymmetric particles and therefore stable, escape ATLAS without detection and cause a missing transverse energy signature.

In this chapter, after a brief discussion of the signal and background samples, a Monte-Carlo cut-based analysis is presented. To improve the background estimation, the contributions from QCD are estimated by using previous single-lepton QCD fake studies [25].

A method to normalize the background from real data is presented. The discovery and exclusion potential for SUSY with real data, based on this analysis, is discussed.

## 4.2 SUSY benchmark points

In ATLAS, a set of different benchmark points in the mSUGRA parameter space is commonly used. A definition of these points is given in table 4.1.

Name	$m_0$ (GeV)	$m_{1/2}$ (GeV)	$A_0$ (GeV)	$\tan(\beta)$	$\text{sgn}(\mu)$
SU1	70	350	0	10	1
SU2	3550	300	0	10	1
SU3	100	300	-300	6	1
SU4	200	160	-400	10	1
SU6	320	375	0	50	1
SU8	210	360	0	40	1
SU9	300	425	20	20	1

Table 4.1: The ATLAS SUSY benchmark points [24]

## 4.3 Sources of Standard Model background

There are only a few standard model sources of same-sign-dilepton final states with high- $p_T$  jets and missing transverse energy.

Sources of prompt charged leptons, that are likely to pass isolation cuts, are  $Z$  bosons and  $W$  bosons. In addition, semileptonic  $b$ - and  $c$ -decays can produce reconstructed leptons which pass the isolation criteria.

The only SM source of real missing transverse energy are neutrinos, originating from leptonic  $W$  decays, from  $\tau$ ,  $b$  or  $c$  decays, or from  $Z \rightarrow \nu\nu$ .

### 4.3.1 Top-antitop

It turns out that the top-antitop decays provide the most dominant background for the same-sign dilepton analysis. Therefore it will be described in more detail. Pairs of top-quarks are produced via gluon-gluon-fusion and quark-antiquark-annihilation. Figure 4.1 shows Feynman graphs of the different top-pair production modes. At the LHC, about 87% of all top-antitop pairs are produced via gluon-gluon-fusion [35].

Due to the very short lifetime of the top-quark ( $\tau \approx 10^{-24} s$ ) no hadronisation process takes place. Each top quark decays into a  $W$  boson and a  $b$ -quark. Each  $W$  boson can decay into a leptonic final state ( $W \rightarrow l + \nu$ ) or into a hadronic final state ( $W \rightarrow q + q'$ ) [03].

Thus, there are three distinct decay modes for top-antitop:



Figure 4.1: The production modes for top-antitop via gluon-gluon fusion and quark-antiquark annihilation [35]

- all-hadronic, where both W bosons decay hadronically. The branching ratio is 44.4% for this channel
- semileptonic, where one of the W bosons decays hadronically and the other W boson decays leptonically<sup>1</sup>. The branching ratio is 29.6% for this channel.
- fully leptonic, where both W bosons decay leptonically. The branching ratio is 4.9% for this channel

Figure 4.2 shows Feynman graphs for the three decay modes. Possible consecutive decays of the b-quarks are not shown there.

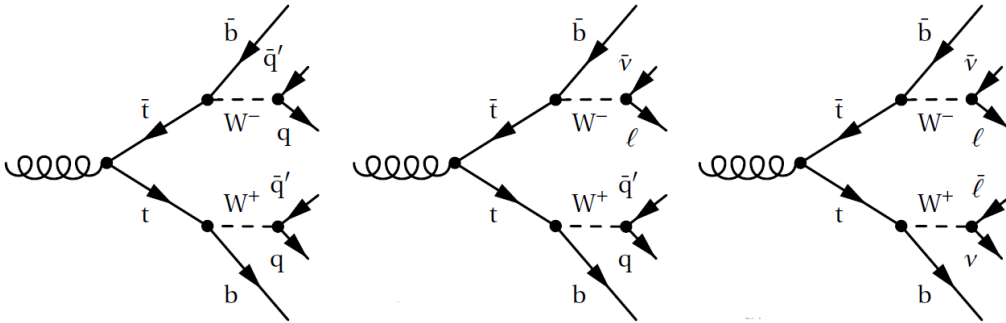
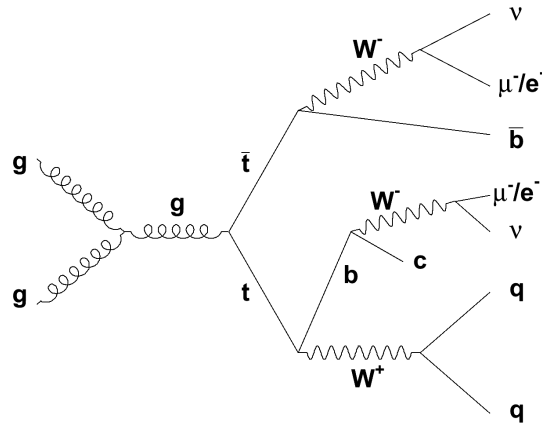


Figure 4.2: The three decay modes for top-antitop: all-hadronic (left), semileptonic (middle) and fully leptonic (right)

For this analysis, the most important decay mode is the semileptonic decay, which is shown in Figure 4.3. Each top quark decays into a W boson and a b quark. One charged lepton originates from the leptonic decay of W boson, the second lepton originates from the b-jet in the hadronic branch. The hadronically decay of W produces jets, and the neutrinos cause a missing transverse energy signature [27].

<sup>1</sup>Decays into  $\tau$  leptons are not counted here, as they have complex consecutive decay modes.

Figure 4.3: Semileptonic  $t\bar{t}$  decay

### 4.3.2 Other Standard Model processes

There is a variety of SM processes that can produce same-sign lepton pairs:

- WW, where one lepton is faked by a jet from the hadronic branch
- WZ can produce up to three charged leptons (which surely contains two same-sign leptons)
- ZZ can produce up to four charged leptons
- Z + jets, where two opposite-charged leptons arise from the Z, and a third lepton is faked by a jet
- W + jets, where the W decays leptonically, and a second lepton is faked by a jet
- QCD, where both leptons are faked by jets
- single-top events with a variety of leptonic final states (s-channel, t-channel and  $Wt$ -channel)

In addition, opposite-sign dilepton final states can turn into a same-sign dilepton final state if the charge of one lepton is misidentified.

## 4.4 Monte-Carlo-Samples

Table 4.2 lists the Athena version 14 Monte-Carlo signal samples which are used for this analysis. The tables with the background samples are shown in the Appendix (tables A.1, A.2, and A.3).

Sample	CSC ID	Integrated luminosity ( $\text{fb}^{-1}$ ) of MC sample	MC events
SU1	105401	4.14	10000
SU3	105403	1.83	9999
SU4	106400	1.58	99608
SU6	105404	8.00	9971
SU8	105406	5.52	9966

Table 4.2: Signal MC samples

## 4.5 Object definition and reconstruction

### 4.5.1 Muon reconstruction

In ATLAS, there are two Muon reconstruction methods, the *MuID* algorithm and the *Staco* algorithm. Each of these methods consists of several algorithms that cover different muon reconstruction strategies. These strategies are:

- Standalone reconstruction, where only data from the Muon System is used
- Combined reconstruction, where tracks from the Muon System are matched and combined with tracks from the Inner Detector
- Tagging, where Inner Detector tracks are identified as muons with additional information from the Calorimeter or Muon System

In the following, the *Staco* algorithm will be briefly presented.

The standalone muon reconstruction is performed by the so called muonboy algorithm. It starts building the track with the parameters from the outer MS regions and iteratively adds data from detector segments in the middle and the inner layers until a complete track is obtained. The complete tracks are fitted and extrapolated through the different detector parts, using a parametrized energy loss for the calorimeters.

The combined reconstruction is performed via a statistical combination of track vectors and covariance matrices of the muonboy tracks at the vertices and tracks from the Inner Detector.

The tagger used for *Staco* muons is called *MuTag*. A track from the Inner Detector is tagged with the innermost available segment from muonboy. *MuTag* is mainly used for 'difficult' muons, i.e. low-energy muons and muons from regions where the Muon System is inefficient for geometrical reasons. Furthermore, additional taggers called *CaloMuonTag* and *CaloMuonLH* use data from the outermost calorimeter layers for energy deposits corresponding to the minimum-ionizing pattern of muons to tag tracks from the Inner Detector [22].

### 4.5.2 Electron reconstruction

In ATLAS, information both from the Electromagnetic Calorimeter clusters and from the Inner Detector tracks are used for the reconstruction of electrons. An electron entering the ECAL causes an electromagnetic shower that distributes the electron energy over a certain space inside the ECAL. Different particle types can be distinguished by variables that describe the shape of the electromagnetic shower, allowing an identification of electrons. Each electron which is identified is required to have a matching track from the ID with a consistent track momentum, i.e. a  $p/E$ -ratio  $< 10$ . If there is no matching track, the object can be identified as a photon, depending on the shower shape.

There are two algorithms used for electron reconstruction, the *track based* algorithm and the *cluster based* algorithm. In the following, the cluster-based algorithm will be described.

The algorithm starts with a cluster in the ECAL and consists of three steps, tower building, pre-cluster finding, and cluster filling. For the first step, the ECAL is geometrically divided into elements with respect to  $\eta$  and  $\phi$ . The tower energy is then calculated from energy inside these elements, summed over the calorimeter layers. Pre-clusters are built by sliding a  $\eta$ - $\phi$ -window over the elements and checking if the transverse energy inside the window exceeds a given energy threshold. If pre-clusters are very close to each other, only the pre-cluster with the highest energy sum is accepted. The final electromagnetic clusters include all cells that are located inside a given rectangle size, centered on the positions of the pre-clusters. Finally, tracks from the Inner Detector are matched to the clusters. The matching requires that the direction of the ECAL shower is in agreement with the direction of the track.

Electrons that are reconstructed with this cluster-based algorithm are called *eGamma* electrons [31] [37].

### 4.5.3 Jet algorithm

Jets consist of hadrons. Hadron showers originate from high-energy quarks and gluons that carry color charge and that are confined by the strong interaction. A jet itself is defined by a jet algorithm which is applied to hadrons.

There is a variety of jet algorithms, but for brevity only the so called *Cone algorithm*, which is shown in Figure 4.4, is presented here.

The cone algorithm starts with a list of hadrons above a given energy threshold. From this list, the object with highest transverse momentum is chosen and a cone with a given radius with respect to the  $\eta$ - $\phi$ -plane is built around this object. From all objects inside this cone, a new centroid is calculated by weighting the objects according to their transverse energies. A new cone is built around the new centroid. This is repeated until the cone converges to a stable configuration. If all hadrons are assigned to stable cone-jets, jets with overlapping cones are

merged or split, depending on the fraction of shared energy. If overlapping cones are split, the overlap energy is assigned to the higher-energetic jet [33].

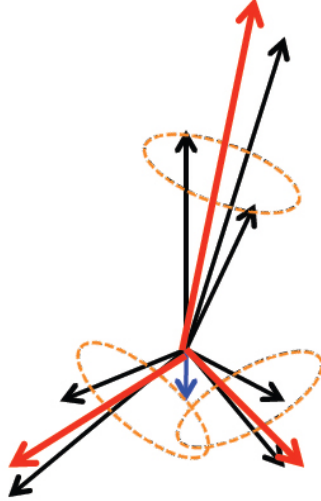


Figure 4.4: Hadrons assigned to jets by a cone algorithm with two overlapping cones

## 4.6 Preselection

The cuts presented in this section select objects (electrons, muons and jets) that fulfill a set of quality criteria. For instance, each selected object has a transverse momentum above a certain threshold value. Furthermore, the preselection has to ensure that objects are as unique as possible, so that no physical object is identified as two different objects at the same time. This so called *overlap removal* is done by applying cuts to the relative distance with respect to the  $\eta$ - $\phi$ -plane between objects, that means some spatial isolation criteria are applied to each object of an event. For charged leptons, additional energetic isolation cuts can be applied, namely the calorimeter energy around the particles track inside a cone with a given radius in the  $\eta$ - $\phi$ -plane.

The event with its remaining objects is only accepted if the same-sign dilepton criterion is fulfilled.

The preselection described below selects signal events with two isolated same-sign leptons. Isolation criteria strongly reduce SM background events where the

second lepton is nonprompt<sup>2</sup> or is a fake lepton<sup>3</sup>.

### 4.6.1 Electrons

Electrons are reconstructed with the eGamma algorithm and are required to fulfill the medium quality criteria. The transverse momentum has to be at least 20 GeV. Electrons from  $|\eta| > 2.5$  as well as from  $1.37 < |\eta| < 1.52$  are rejected. The calorimeter energy deposited inside a cone with  $R = 0.2$  in the  $\eta$ - $\phi$ -plane around the electron's track (*etcone20*) is required to be less than 10 GeV.

### 4.6.2 Muons

Muons are reconstructed with the Staco algorithm, where the matching  $\chi^2$  is required to be less than 100. The transverse momentum has to be at least 20 GeV. Muons with an  $|\eta| > 2.5$  are rejected. The calorimeter energy inside  $R = 0.2$  around the muon's track is required to be lower than 10 GeV.

### 4.6.3 Jets

Jets are defined by the Cone4 algorithm. A jet is rejected if  $|\eta| > 2.5$  or if  $p_T < 20$  GeV.

### 4.6.4 Spatial Isolation

For all jet-lepton pairs and jet-muon pairs, the distance  $\Delta R = \sqrt{(\Delta\eta)^2 + (\Delta\phi)^2}$  is calculated. If  $\Delta R(\text{e,jet}) < 0.2$ , the jet is rejected, if  $0.2 < \Delta R(\text{e,jet}) < 0.4$ , the electron is rejected.

If  $\Delta R(\mu,\text{jet}) < 0.4$  the muon is rejected.

In a few cases, two reconstructed leptons can be very close to each other, e.g. if a  $\gamma$  from lepton bremsstrahlung can fake an electron. Therefore, if  $\Delta R$  of a muon and an electron is below 0.1, the electron is rejected, if  $\Delta R$  of two electrons is below 0.1, the electron with the lower transverse momentum is rejected.

### 4.6.5 Event preselection

After the object preselection described above, the event is accepted only if it contains at least two leptons with the same sign of charge. Additional leptons are allowed.

---

<sup>2</sup>*Nonprompt* leptons originate from a b or c decay

<sup>3</sup>*Fake* leptons are jets which are misidentified in the detector

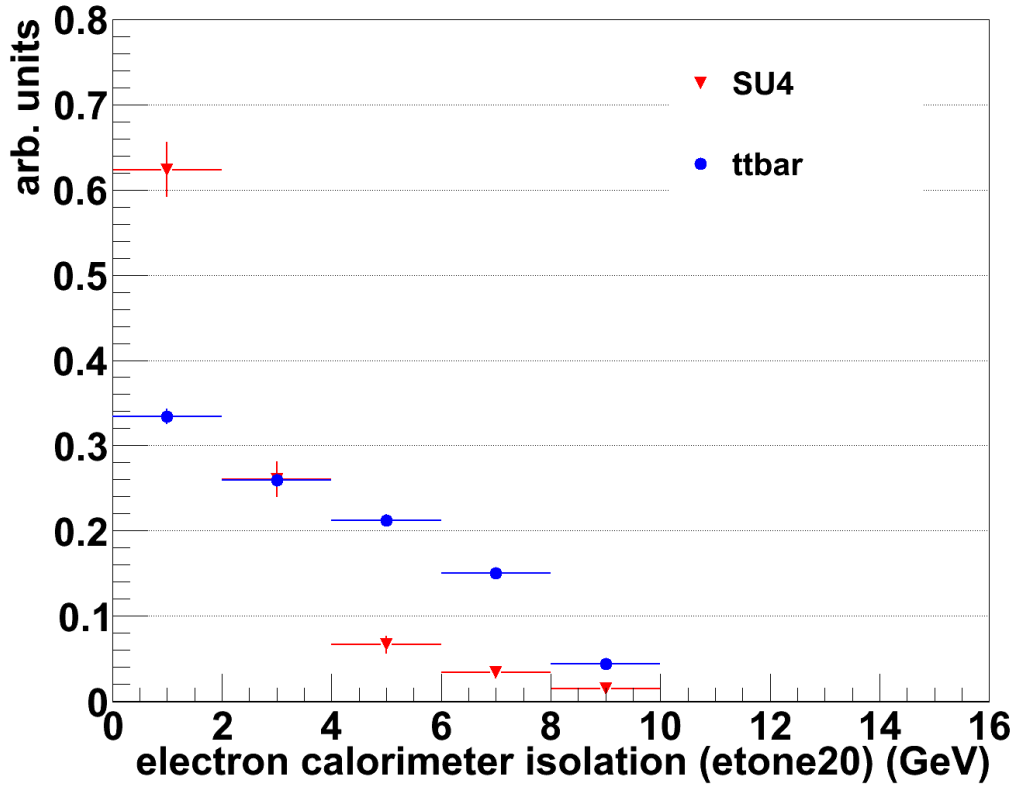


Figure 4.5: The calorimeter isolation etcone20 for all electrons after the preselection. Both histograms are normalized to  $\sum(\text{entries}) = 1$ .

#### 4.6.6 Results

After the preselection, the background is strongly dominated by QCD and other multijet events. All event numbers, uncertainties from MC statistics and significances are calculated for an integrated luminosity of  $200 \text{ pb}^{-1}$ , the numbers given for the QCD background refer to the results from section 4.8. The significance is defined as  $S/\sqrt{B}$ , where S is the number of signal events and B is the total number of background events. SU4 yields the highest significance compared to other signal processes considered in this study.

For most SUSY points, the preselection keeps less than 10 events for an integrated luminosity of  $200 \text{ pb}^{-1}$ . A 'discovery' can be defined by a significance of at least 5 with at least 10 signal events; the SU4 point is the only ATLAS SUSY point being able to fulfill these criteria at  $\sqrt{s} = 10 \text{ TeV}$  in the same-sign dilepton channel. But even less than ten signal events will provide interesting information if a signal is observed in a different channel, e.g. inclusive SUSY searches with 0 or 1 leptons.

Sample	Events for $200 \text{ pb}^{-1}$	MC uncert.	Significance
Signal			
SU1	5.28	0.5	0.06
SU3	4.91	0.7	0.06
SU4	117.7	5.0	1.39
SU6	2.11	0.2	0.02
SU8	1.53	0.2	0.02
Background			
$t\bar{t}$	68.3	1.5	
WZ	28.6	0.4	
WW	1.2	0.4	
ZZ	5.2	0.4	
Z + jets	692.6	19.9	
W + jets	158.7	12.8	
$b\bar{b}$	140.1	53.0	
single top	6.9	0.9	
Z + $\gamma$	3.7	0.2	
W + $\gamma$	3.4	0.8	
<i>QCD multijet</i>	6164.2	33.2	
total background	7272.9	66.9	

Table 4.3: Effects of the preselection cuts on signal and background. The values given for QCD refer to the method described below.

## 4.7 Analysis cuts

The analysis cuts described below further reduce the SM background. A Z-veto on all opposite-sign lepton pairs and all same-sign electron pairs is applied in order to reduce the WZ and Z+jets background. In section 4.9 a method is presented to estimate the SM background from data by spanning a 2-dimensional 'cut-space', which is divided into four regions; one signal- and three control regions (see Table 4.4). The background in the signal region D is then estimated by measuring the background in the control regions A, B, and C. The three cuts on the transverse mass, the transverse momentum of the leading jet and the missing transverse energy are optimized in combination to ensure that a real observation yields enough events to estimate the background from data with acceptable statistical uncertainties. The following criteria have to be fulfilled:

- For  $200 \text{ pb}^{-1}$ , there are at least 10 SUSY events in the signal region (see below)

- Each control region contains at least 4 background events
- Each control region contains less SUSY events than background events
- From all combinations that fulfill the criteria above, the one with the highest  $S/\sqrt{B}$  in the signal region is chosen

<b>Control region A</b>	Z-Veto, $M_T > \text{mtcut}$ , $1^{\text{st}} \text{ jet } p_T > 1^{\text{st}} \text{ jet } p_{T\text{upper}}$ , $E_{\text{T}}^{\text{miss}}{}_{\text{lower}} < E_{\text{T}}^{\text{miss}} < E_{\text{T}}^{\text{miss}}{}_{\text{upper}}$
<b>Control region B</b>	Z-Veto, $M_T > \text{mtcut}$ , $1^{\text{st}} \text{ jet } p_{T\text{lower}} < 1^{\text{st}} \text{ jet } p_T < 1^{\text{st}} \text{ jet } p_{T\text{upper}}$ , $E_{\text{T}}^{\text{miss}}{}_{\text{lower}} < E_{\text{T}}^{\text{miss}} < E_{\text{T}}^{\text{miss}}{}_{\text{upper}}$
<b>Control region C</b>	Z-Veto, $M_T > \text{mtcut}$ , $1^{\text{st}} \text{ jet } p_{T\text{lower}} < 1^{\text{st}} \text{ jet } p_T < 1^{\text{st}} \text{ jet } p_{T\text{upper}}$ , $E_{\text{T}}^{\text{miss}} > \text{cut on } E_{\text{T}}^{\text{miss}}$
<b>Signal region D</b>	Z-Veto, $M_T > \text{mtcut}$ , $1^{\text{st}} \text{ jet } p_T > 1^{\text{st}} \text{ jet } p_{T\text{upper}}$ , $E_{\text{T}}^{\text{miss}} > \text{cut on } E_{\text{T}}^{\text{miss}}$

Table 4.4: The definition of the A,B,C and D region

The values given for QCD refer to the reweighted samples as described below.

### 4.7.1 Z-Veto

The invariant mass is the length of the relativistic 4-vector of a system or subsystem. It is independent of the frame of reference and is a measure for the total mass of the system or subsystem. Here, the invariant mass  $m_{ll}$  is calculated for all electron pairs as well as for all opposite-sign muon pairs.<sup>4</sup> from the sum of the 4-vectors of the two leptons:

$$m_{ll} = \sqrt{\sum_{i=1}^2 E_i^2 - \sum_{j=1}^3 (\sum_{i=1}^2 p_{ij})^2} \quad (4.1)$$

The index  $i$  ( $i = 1, 2$ ) identifies each of the two leptons, the index  $j$  ( $j = 1, 2, 3$ ) refers to the spatial components  $x$ ,  $y$ , and  $z$  of the momentum  $p$ .  $E$  is the energy of the lepton.

If at least one of these lepton pairs has  $|m_{ll} - m_Z| < 10$  GeV, the two leptons are likely to originate from a  $Z$  boson and the event is rejected. Figure 4.6 shows the invariant dilepton-mass distribution for SUSY, all  $Z$  background samples and for

<sup>4</sup>If the muon charge is misidentified, the momentum will be mismeasured, too.

the total background. This cut mainly affects events with three charged leptons with two of the leptons originating from a Z boson. Table 4.5 shows the effect of the Z-veto on signal and background. Events without a Z boson can be rejected by random. The Z-Veto efficiency, i.e. the number of events after the cut divided by the number of events before the cut, is higher than 85% for these events. The Z-Veto and cut efficiencies on the total background are defined as:

$$\text{eff} = \frac{\text{sum of background events after cut or Z-Veto}}{\text{sum of background events before cut or Z-Veto}}$$

. The number of events where leptons originate from a Z boson, i.e. WZ, ZZ, Z+jets and Z+ $\gamma$ , is strongly reduced by this cut.

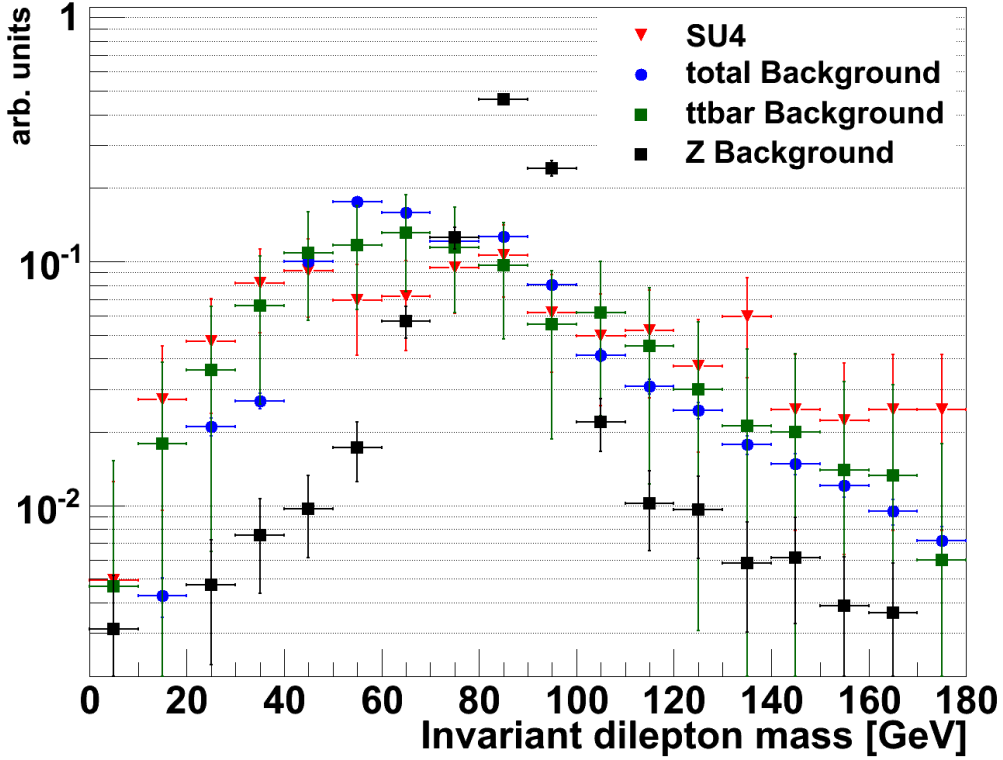


Figure 4.6: Invariant dilepton mass distribution. All histograms are normalized to  $\sum(\text{entries}) = 1$ .

#### 4.7.2 Transverse mass cut

The transverse mass is  $M_T = \sqrt{2\cancel{E}_T \cdot p_{t,l} \cdot (1 - \cos(\phi(l, \cancel{E}_T)))}$  where  $l$  is the lepton with the highest transverse momentum, and  $p_{t,l}$  is its transverse momentum.

Sample	Z-Veto eff.	Events for 200 pb <sup>-1</sup>	MC unc.
SU4	0.89	104.4	4.7
$t\bar{t}$	0.91	62.1	1.5
WZ	0.35	9.9	0.2
WW	1.00	1.2	0.4
ZZ	0.18	0.9	0.2
Z + jets	0.30	206.4	10.8
W + jets	0.92	145.5	12.2
QCD	0.86	5301.2	30.7
$b\bar{b}$	1.00	140.1	53.0
single top	0.94	6.4	1.4
Z + $\gamma$	0.46	1.7	0.2
W + $\gamma$	1.00	3.4	0.8
total background	0.81	5878.9	63.4

Table 4.5: Z-Veto efficiencies and surviving events

Figure 4.7 shows the  $M_T$  distribution for signal and background. A clear peak is visible at the W mass for many of the background events. Requiring  $M_T > m_W$  strongly reduces the background from leptonic W decays. Table 4.6 shows the cut efficiencies as well as the number of events surviving both Z veto and the cut on the transverse mass. The cut efficiencies are defined here as the ratio of events after Z veto and  $M_T$  cut to the events after the Z veto.

As expected, this cut reduces the number of events with W bosons. As this cut implicitly contains a cut on the missing transverse energy, it has a strong effect on all background processes where there is no real missing energy from neutrinos. After preselection, Z veto and transverse mass cut, the significance for SU4 signal is 4.7.

### 4.7.3 Cut on Missing transverse Energy

Because of the LSPs and the neutrinos which are produced in the decay chains, SUSY events usually cause more missing transverse energy in the detector than all SM backgrounds (see Figure 4.8). For this analysis, a cut at  $E_T^{\text{miss}} = 60$  GeV is applied, further suppressing the SM background with respect to the SU4 signal. Table 4.7 shows the results. From the SUSY signal, still 91 % are selected. The signal significance after this cut is 5.5.

Having a look at Figure 4.8 again, it becomes clear that for harder cuts on the missing transverse energy, i.e.  $E_T^{\text{miss}} > 100$  GeV, the significance could be strongly increased, but then it would be much harder and more imprecise to estimate the background from real data.

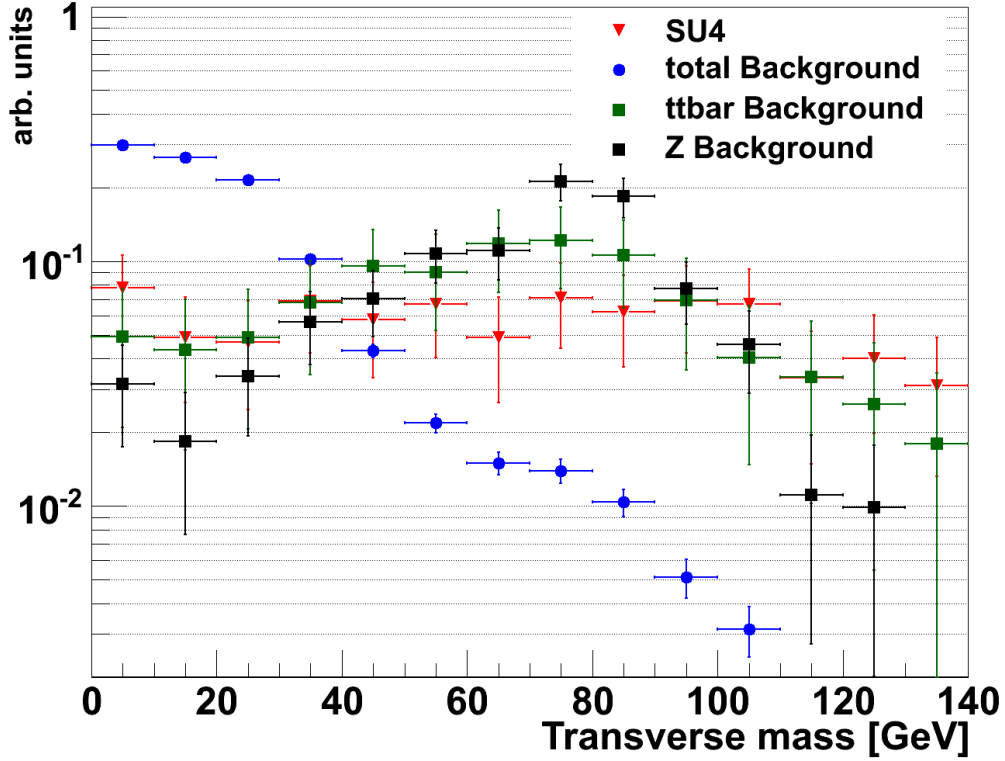


Figure 4.7: Transverse mass distribution. All histograms are normalized to  $\sum(\text{entries}) = 1$ .

#### 4.7.4 Cut on $p_T$ of the leading Jet

As Figure 4.9 shows, the leading jet  $p_T$ s of SUSY events tend to be higher than those of SM background events. By accepting only events with at least one jet above 100 GeV, the SM background is significantly reduced. Table 4.8 shows the cut efficiencies, defined here as the ratio of events after Z veto,  $M_T$  cut and jet  $p_T$  cut to the events after the Z veto and  $M_T$  cut.

The cut efficiency on the SM background is 7 %, whereas 77 % of the SUSY signal are kept, leading to a final SU4 significance of 17.2.

Sample	$M_T$ cut eff.	Events for $200 \text{ pb}^{-1}$	MC unc.
SU4	0.55	57.0	3.5
$t\bar{t}$	0.37	22.9	0.9
WZ	0.46	4.5	0.1
WW	0.40	0.5	0.2
ZZ	0.12	0.1	0.1
Z + jets	0.02	3.9	1.2
W + jets	0.35	51.4	7.1
QCD	0.01	52.5	1.7
$b\bar{b}$	0	0	0
single top	0.27	1.7	0.5
Z + $\gamma$	0.03	0.04	0.03
W + $\gamma$	0.37	1.3	0.5
total background	0.02	138.9	7.5

Table 4.6: Transverse mass cut efficiencies and surviving events

Sample	$E_T^{\text{miss}}$ cut eff.	Events for $200 \text{ pb}^{-1}$	MC unc.
SU4	0.91	51.6	3.3
$t\bar{t}$	0.59	13.6	0.7
WZ	0.40	1.8	0.1
WW	0.25	0.1	0.1
ZZ	0.5	0.1	0.1
Z + jets	0.05	0.2	0.1
W + jets	0.28	14.6	4.0
QCD	0.91	40.8	1.5
$b\bar{b}$	-	0	0
single top	0.52	0.9	0.4
Z + $\gamma$	0	0	0
W + $\gamma$	0.37	0.4	0.3
total background	0.29	87.4	13.9

Table 4.7: Missing transverse energy cut efficiencies and surviving events

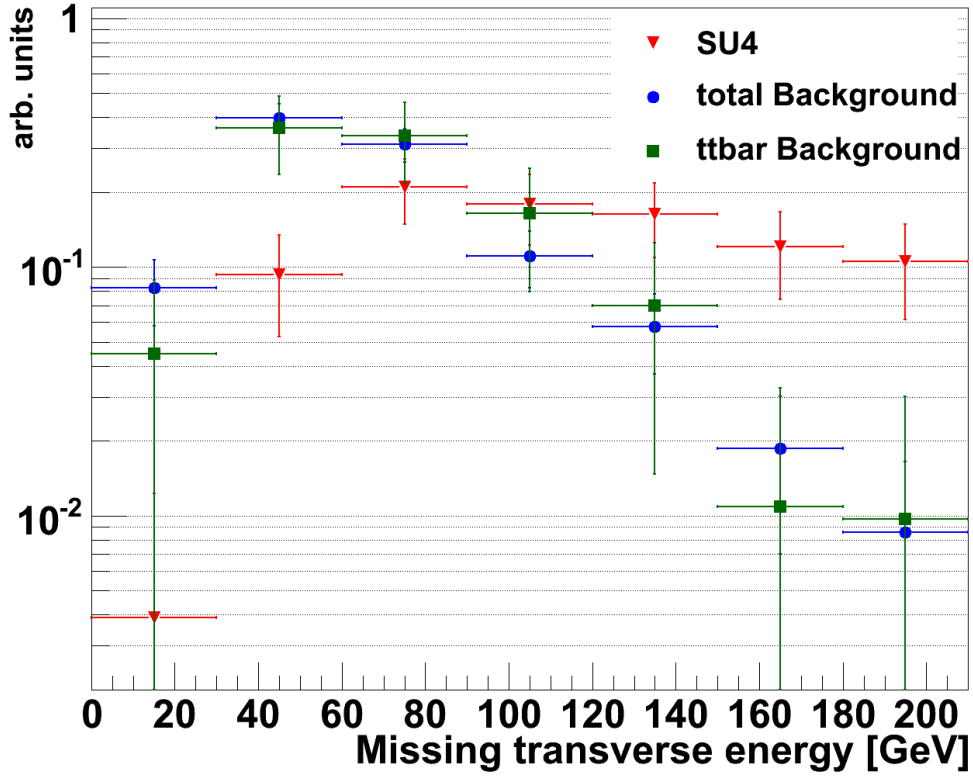


Figure 4.8: Missing transverse energy distribution. All histograms are normalized to  $\sum(\text{entries}) = 1$ .

Sample	Jet cut eff.	Events for $200 \text{ pb}^{-1}$	MC unc.
SU4	0.77	39.5	2.9
$t\bar{t}$	0.28	3.8	0.4
WZ	0.16	0.3	$\approx 0$
WW	0	0	0
ZZ	0	0	0
Z + jets	0.04	0.01	$\approx 0$
W + jets	0.05	0.75	0.4
QCD	$\approx 0$	$\approx 0$	$\approx 0$
$b\bar{b}$	-	0	0
single top	0.51	0.5	0.4
Z + $\gamma$	-	0	0
W + $\gamma$	0	0	0
total background	0.07	5.3	0.7

Table 4.8: Leading jet  $p_T$  cut efficiencies and surviving events

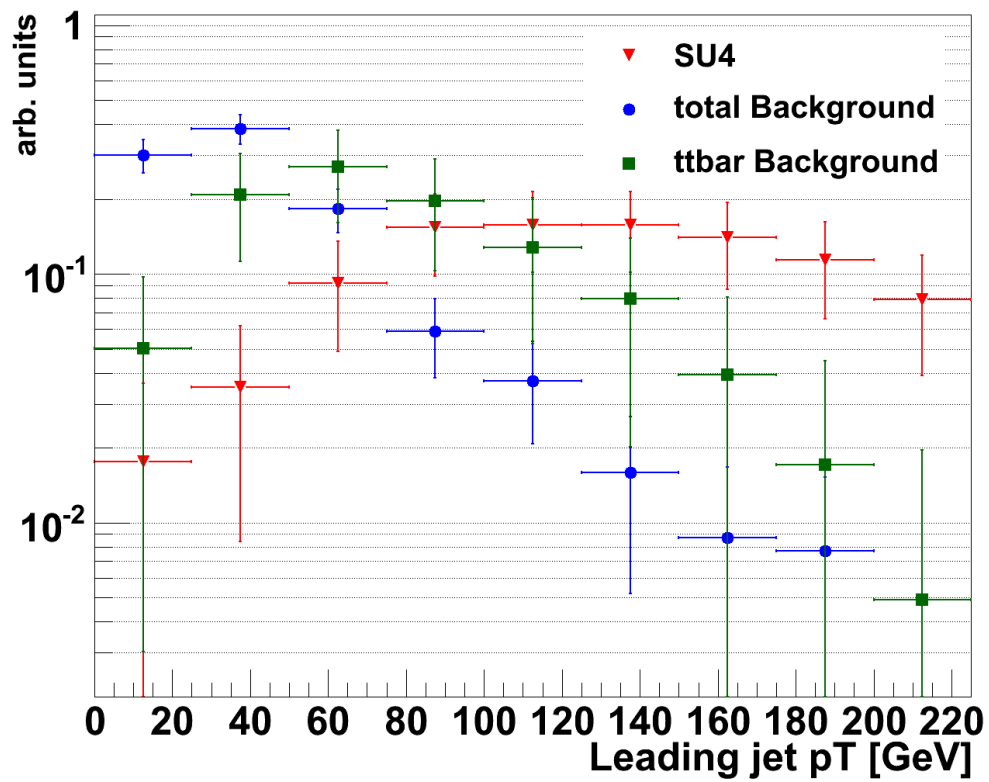


Figure 4.9: Leading jet  $p_T$  distribution. All histograms are normalized to  $\sum(\text{entries}) = 1$ .

## 4.8 QCD background

The QCD cross-section is high, but the available statistics, i.e. number of MC events and a low fake-rate for two jets faking leptons, is too low for this analysis. Therefore, additional analysis of fake leptons is required. For a first estimation, only fake electrons are taken into account. This is valid, as the muon fake probabilities are known to be significantly smaller than those of electrons [25].

The idea is to insert two fake electrons into the sample, depending on the properties of the truth-jets, so that the event will survive the preselection cuts, and reweight the event with the probability that this fake scenario occurs. Therefore, it is assumed that the fake probabilities for different jets in an event only depend on jet properties like  $p_T$  and are otherwise independent. Of course, this is a rough estimation, but it yields first results with an improved statistical precision, now limited by the single-electron fake-rate, for which the statistics is good enough, instead of the two-lepton fake-rate.

Two reconstructed jets that match truth-jets are replaced by electrons, and the event is reweighted with the combined fake-probability. This is done for every jet combination in an event. This method creates multiple events out of a single 'normal' Monte-Carlo event.

In order to replace a jet by a fake electron, a transverse momentum depending on the truth-jet properties needs to be assigned and the missing transverse energy must be recalculated. Therefore, the properties of the fake electrons and their dependencies on the properties of the truth jets are obtained from the Monte-Carlo QCD multijet (J0-J6) samples. The same object preselection as shown above is applied, but in this case no same-sign dilepton requirement is applied, in order to get the fake electrons that are relevant for our analysis with a sufficient fake statistics. For every reco-electron - truth-jet combination,  $\Delta R$  is calculated. If at least one of the  $\Delta R$ s is below 0.1, the event is selected.

The probability to find a fake electron after the object preselection as a function of the transverse momentum on the truth jet is shown in Figure 4.10.

Figure 4.11 shows the dependence of the transverse momenta of fake electrons on the transverse momenta of truth-jets. Obviously, there is a medium correlation. Figure 4.12 shows a histogram of  $\frac{p_{T,fakeel}}{p_{T,truthjet}}$  with a Gaussian fit to the data, The parameters of the Gaussian fit are: Mean=0.63 and  $\sigma=0.18$ .

The Missing Energy is not only caused by the misidentification of a jet as an electron. The contribution of the object misidentification (i.e. the electron fake) to the missing transverse energy is estimated by subtracting the  $p_x$  and  $p_y$  components of the replaced reconstructed jets from the missing transverse energy and adding the  $p_T$  components of the new electrons.

In the following, an event is assumed to contain N 'good' jets, where good means that the jet matches a truth jet and survives our object preselection cuts. Then

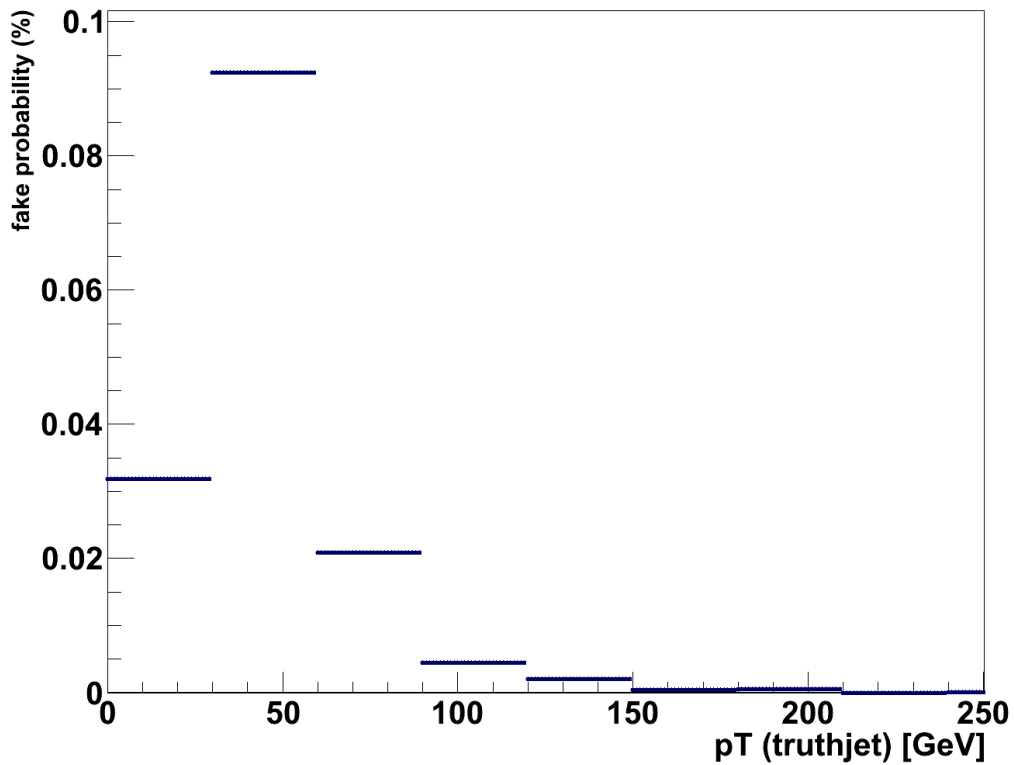


Figure 4.10: The probability to find a fake electron as a function of the truth jet  $p_T$

the following steps are performed for every jet pair:

- replace the jets by same-sign electrons
- assign  $p_T$ -values to the electrons
- recalculate the missing energy
- assign a weight to the event
- save the event

The  $p_T$ -values are assigned to the constructed fake electrons as follows:

$$p_T(el) = \text{gaus}(0.63 \cdot p_T(\text{truthjet}), 0.18 \cdot p_T(\text{truthjet})) \quad (4.2)$$

where  $gaus(mean, sigma)$  provides random numbers with a Gaussian distribution, with the passed parameters for the mean value and the standard deviation.

The weight assigned to each of the newly created events is:

$$w = P = \frac{1}{2} \cdot P_F(jet_n) \cdot P_F(jet_m) \quad (4.3)$$

where  $P_F$  denotes the fake probability for a single electron, and n,m are the two indices of the replaced jets. The factor of  $\frac{1}{2}$  refers to the same-sign requirement. Table 4.9 shows the results.

preselection	Z-veto	$M_T$	$E_T^{\text{miss}}$	jet $p_T$
$6164.2 \pm 33.2$	$5301.2 \pm 30.7$	$52.5 \pm 1.7$	$40.8 \pm 1.5$	$0.05 \pm 0.004$

Table 4.9: Cut flow table for QCD. The event numbers and MC uncertainties are calculated for  $200 \text{ pb}^{-1}$ .

After all cuts, the QCD contribution to the SM background is less than 1%.

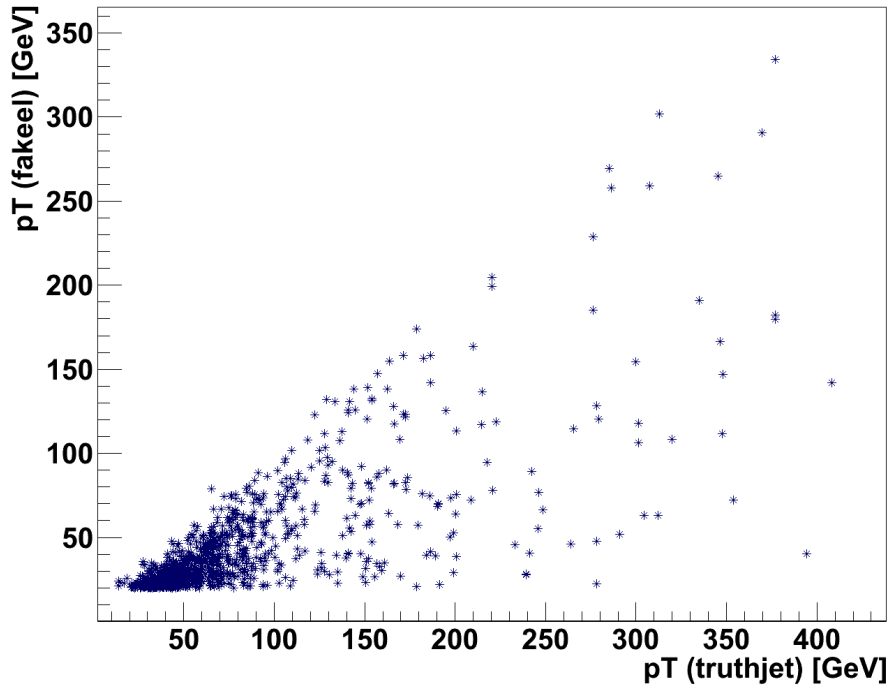


Figure 4.11: The dependence of the fake electron  $p_T$ s on the truth jet  $p_T$ s

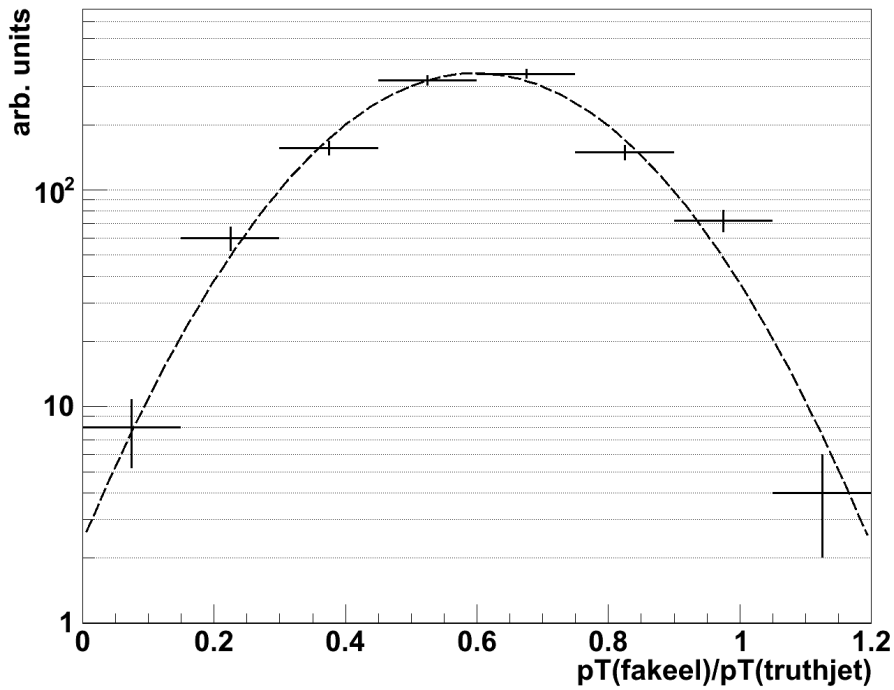


Figure 4.12: The distribution of  $\frac{p_T(\text{fakeel})}{p_T(\text{truthjet})}$  with a gaussian fit. The fit parameters are: Mean = 0.63,  $\sigma=0.19$

## 4.9 Background estimation from data

In order to find SUSY, it is crucial to have a Monte-Carlo-independent method to estimate the SM background in the signal region. Therefore, four regions in a multidimensional 'cut-space' are defined, where the control regions shall be dominated by background events, whereas one other region is defined by the analysis cuts and dominated by SUSY signal events [29].

For this analysis, the four regions A,B,C and D are defined according to Table 4.10.

<b>Control region A</b>	Z-Veto, $M_T > 80$ GeV, 1 <sup>st</sup> jet $p_T > 100$ GeV $30 \text{ GeV} < E_T^{\text{miss}} < 60$ GeV
<b>Control region B</b>	Z-Veto, $M_T > 80$ GeV, $50 \text{ GeV} < 1^{\text{st}} \text{ jet } p_T < 100$ GeV, $30 \text{ GeV} < E_T^{\text{miss}} < 60$ GeV
<b>Control region C</b>	Z-Veto, $M_T > 80$ GeV, $50 \text{ GeV} < 1^{\text{st}} \text{ jet } p_T < 100$ GeV, $E_T^{\text{miss}} > 60$ GeV
<b>Signal region D</b>	Z-Veto, $M_T > 80$ GeV, 1 <sup>st</sup> jet $p_T > 100$ GeV, $E_T^{\text{miss}} > 60$ GeV

Table 4.10: The definition of the A,B,C and D region

Figure 4.14 shows the distribution of the leading jet  $p_T$  for  $30 \text{ GeV} < E_T^{\text{miss}} < 60$  GeV and for  $E_T^{\text{miss}} > 60$  GeV. Figure 4.15 shows the distribution of the  $E_T^{\text{miss}}$  for  $50 \text{ GeV} < \text{leading jet } p_T < 100$  GeV and for leading jet  $p_T > 100$  GeV. The distributions do not show a significant dependence on the parameter they are compared with. The correlation factor of the  $E_T^{\text{miss}}$  and the leading jet  $p_T$  is 0.12.

It is assumed that with real data, the number of background events in the signal region  $D$  can be estimated from the measured number of background events in the other three regions with  $D_{BG} = \frac{A+C}{B}$ . This method is tested by applying it to the Monte-Carlo data. Table 4.11 shows the four regions with the numbers and errors from Monte-Carlo, scaled to an integrated luminosity of  $200 \text{ pb}^{-1}$ . In the following, the method is tested with MC data and MC uncertainties for two scenarios (SUSY exists or does not exist). If there is no SUSY, i.e there is only SM background in the four regions, one obtains  $\frac{A+C}{B} = 6.5 \pm 1.1$  and  $D = 5.3 \pm 0.3$ . If SUSY exists, it contaminates the A,B and C regions, as the cuts do not perfectly separate signal from background. In this case, the method predicts  $13.6 \pm 2.6$  events. The analysis provides  $44.8 \pm 2.9$  events (SUSY + background). As expected, the SM background in the region D is overestimated, but a clear

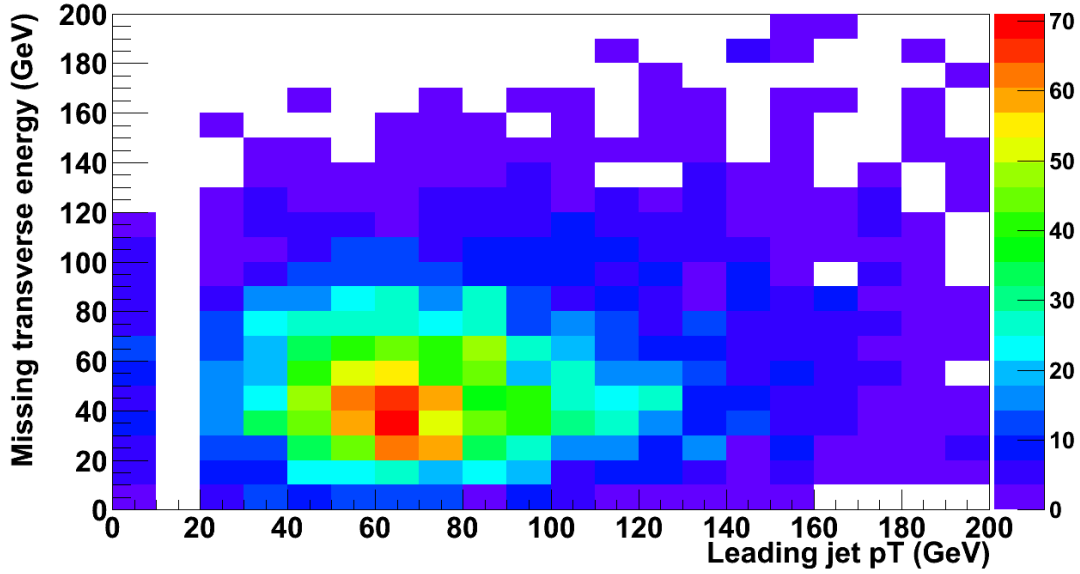


Figure 4.13: The missing transverse energy and the transverse momentum of the leading jet for the  $t\bar{t}$  sample after preselection. The entries in the 0 GeV bin for the jet momenta correspond to events without reconstructed jets.

excess of SUSY events is still observed. To estimate the number of background events and to estimate the expected excess of events if SUSY exists, systematic uncertainties are taken into account, and the probability distribution for the number of expected background events in the SUSY signal regions as well as a prediction for an observed signal significance are calculated.

<b>A</b>	<b>D</b>
Background $4.2 \pm 0.3$	Background $5.3 \pm 0.3$
SUSY $2.6 \pm 0.7$	SUSY $39.5 \pm 2.9$
<b>B</b>	<b>C</b>
Background $12.2 \pm 1.9$	Background $18.9 \pm 0.6$
SUSY $2.2 \pm 0.7$	SUSY $9.9 \pm 1.5$

Table 4.11: Four regions in a 2-dim cut space. The values for signal and background are scaled to an integrated luminosity of  $200 \text{ pb}^{-1}$ . The errors refer to the uncertainties from MC statistics.

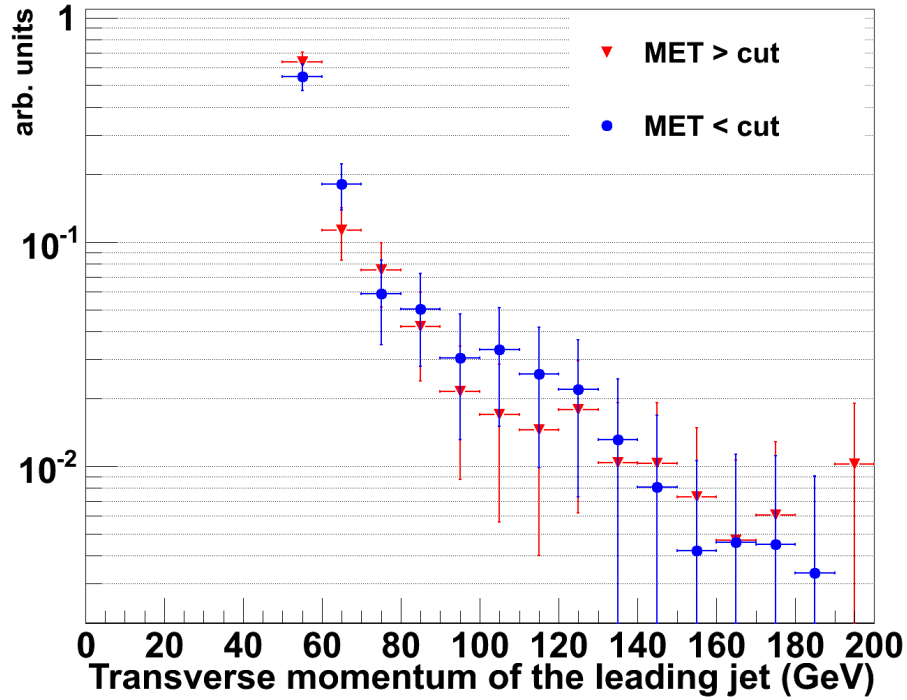


Figure 4.14: The transverse momentum of the leading jet for all background samples, shown for  $E_T^{\text{miss}} > \text{cut}$  and for  $E_T^{\text{miss}} < \text{cut}$

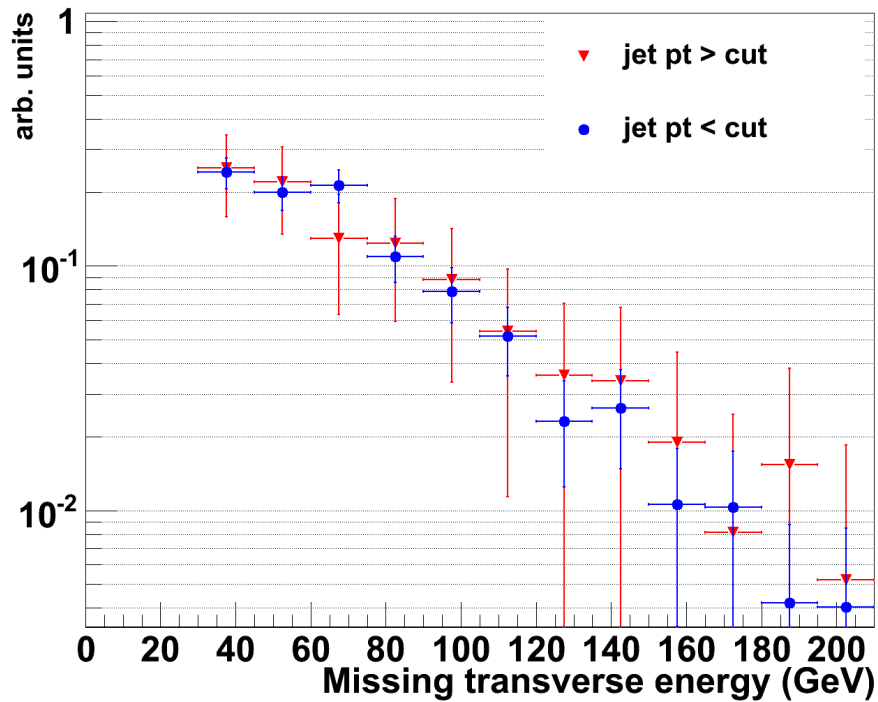


Figure 4.15: The missing transverse energy for all background samples, shown for  $\text{Jet}_{1st} p_T > \text{cut}$  and for  $\text{Jet}_{1st} p_T < \text{cut}$

## 4.10 Systematic uncertainties

The measurement of jet energies relies on the calibration and on the understanding of the calorimeter system. Therefore, the jet energy scale (JES) is subject to systematic uncertainties. The efficiencies of all cuts involving jet energies depend on the JES. The uncertainty of the JES is assumed to be 10%. First, the transverse momenta of all jets are multiplied by a factor of 1.1. The missing transverse energy is recalculated by vectorially subtracting the old (unchanged) transverse momenta and adding the rescaled transverse momenta [24]. Then, all cuts are applied. The difference of the event numbers with and without rescaling the transverse momenta, divided by the number of events without a change of the JES, is assumed as the relative uncertainty. Second, the transverse momenta of all jets are multiplied by a factor of 0.9 and the relative uncertainties are calculated again. The higher value for the relative uncertainty is considered as the total relative uncertainty due to the JES uncertainty. Figure ?? shows the distribution of the transverse momentum of the leading jet for different JES scale factors. In region A, the JES uncertainty leads to a relative uncertainty of the SU4 signal of about 20%, and about 18% for the SM background. In region B, the SU4 uncertainty is 25%, and the background uncertainty is about 20%. In region C, the SU4 uncertainty is roughly 15%, and the background uncertainty is about 30%. In the D region, the SU4 uncertainty is about 6%, and the background uncertainty is roughly 13%.

The systematic uncertainty due to the jet energy resolution is determined by smearing the transverse momenta of the jets. For each jet, a Gaussian random number is calculated with a mean value corresponding to the transverse momentum of the jet, and a standard deviation of 10% of the transverse momentum of the jet. The missing transverse energy is recalculated by vectorially subtracting the unsmearred transverse momenta and adding the smeared transverse momenta [24]. After applying all cuts, the difference of the event numbers with and without smearing the transverse momenta, divided by the number of events without smearing, is assumed as the relative uncertainty. In region A, the jet energy resolution leads to a relative uncertainty of the SU4 signal of about 17%, and about 3% for the SM background. In region B, the SU4 uncertainty is 20%, and the background uncertainty is about 2%. In region C, the SU4 uncertainty is roughly 4%, and the background uncertainty is 0.3%. In the D region, the SU4 uncertainty is about 4%, and the background uncertainty is roughly 3%.

The effects of the resolution of the missing energy is determined as follows: the transverse momenta of all muons, electrons and jets are vectorially subtracted from the missing transverse energy. For the remnant, a Gaussian random number is calculated with a mean value corresponding to the remaining missing transverse energy, and a standard deviation of 10% of the remaining missing transverse

energy. Then, the transverse momenta of all muons, electrons and jets are vectorially added [24]. Then, all cuts are applied, and the difference of the event numbers with and without smearing the missing transverse energy, divided by the number of events without smearing, is assumed as the relative uncertainty. In region A, the missing transverse energy resolution leads to a relative uncertainty of the SU4 signal of about 17%, and about 10% for the SM background. In region B, the SU4 uncertainty is 10%, and the background uncertainty is negligible here. In region C, the SU4 uncertainty is roughly 4%, and the background uncertainty is about 1%. In the D region, the SU4 uncertainty is about 2%, and the background uncertainty is roughly 5%.

The systematic uncertainty due to the muon energy resolution is determined by smearing the transverse momenta of the muons. For each muon, a Gaussian random number is calculated with a mean value corresponding to the transverse momentum of the jet, and a standard deviation of 4% of the transverse momentum of the muon, if the latter is lower than 100 GeV, or 10% of the transverse momentum of the muon, if the latter is higher than 100 GeV. The missing transverse energy is recalculated by vectorially subtracting the unsmeared transverse momenta and adding the smeared transverse momenta [24]. After applying all cuts, the difference of the event numbers with and without smearing the transverse momenta of the muons, divided by the number of events without smearing, is assumed as the relative uncertainty. In region A, the muon energy resolution leads to a negligible relative uncertainty of the SU4 signal, and an uncertainty of about 1% for the SM background. In region B, the SU4 uncertainty is roughly 0, and the background uncertainty is 0.3%. In region C, the SU4 uncertainty is 0 again, and the background uncertainty is about 1%. In the D region, the SU4 uncertainty is about 1%, and the background uncertainty is roughly 1%, too.

The relative uncertainty due to a finite number of available Monte-Carlo events is estimated to be  $\frac{\sqrt{N}}{N}$  for each sample, where N is the number of Monte-Carlo events in the considered region.

The relative uncertainties of the cross-sections are assumed to be 12%, and the uncertainty of the determination of the integrated luminosity is assumed to be 20%.

The overall relative uncertainty in each region is calculated by quadratically adding the relative uncertainties due to the various sources. Table 4.12 lists all the numbers and results.

Source	uncertainty	A		B	
		S (%)	B (%)	S (%)	B (%)
Jet energy scale	10 %	20.1	17.8	25.0	20.4
Jet energy resolution	10 %	16.7	3.0	20.0	2.0
MET resolution	10 %	16.7	9.5	10	0.2
$\mu$ energy resolution	4% - 11%	0	0.9	0	0.3
cross-section		-	12	-	12
MC statistics	$\sqrt{(N)}$	33.4	6.9	14.1	16.0
Integrated luminosity	20 %	20	20	20	20
total		49.8	31.8	41.5	34.9

Source	uncertainty	C		D	
		S (%)	B (%)	S (%)	B (%)
Jet energy scale	10 %	15.3	29.5	5.8	12.7
Jet energy resolution	10 %	4.3	0.3	4.3	3.0
MET resolution	10 %	4.3	0.9	1.6	4.9
$\mu$ energy resolution	4% - 11%	0	1.2	1.1	0.8
cross-section		-	12	-	12
MC statistics	$\sqrt{(N)}$	12.2	3.1	4.3	5.2
Integrated luminosity	20 %	20	20	20	20
total		28.6	37.8	21.8	27.7

Table 4.12: Systematic uncertainties

## 4.11 Statistical analysis

The real numbers of events in each region are integer numbers which are expected to follow Poisson distributions. The mean values for these Poisson distributions are the values derived from the MC analysis. As the mean values are subject to systematic uncertainties, the predicted distributions for the numbers of expected events in the four regions are combinations of Poisson distributions with several Gaussian distributions.

### 4.11.1 Significance

Many feasibility studies use a comparatively simple definition of the signal significance [34]:

$$\text{Significance} = \frac{\text{Signal}}{\sqrt{\text{Background}}} \quad (4.4)$$

This definition assumes that both signal and background have symmetric Gaussian probability distributions.

But, for instance, the number of observed events in any counting experiment does not follow a symmetrical probability distribution, as negative event numbers are obviously forbidden. Therefore, the significance has to be defined for this analysis, where a variety of symmetric and asymmetric sources of uncertainties are combined. An observation of an excess is the more significant, the more unlikely it is to be a statistical fluctuation of the background. For a given expected number of background events  $B$ , a probability distribution  $P_B(n)$  to observe  $n$  events has to be built (see Figure 4.16), with  $B$  being the mean value of the distribution. For a measured number of events  $M$ , where  $M$  might consist of background and signal, or background only, the probability  $p(M)$  to observe  $M$  or less events has to be calculated:

$$p(M) = \sum_0^M P_B(n) \quad (4.5)$$

Usually, this probability is transformed into the number of Gaussian standard deviations it corresponds to. Therefore, the inverse Gauss Error Function has to be calculated. The Gauss Error Function is:

$$\text{Erf}(x) = \frac{2}{\sqrt{\pi}} \int_0^x e^{-t^2} \cdot dt \quad (4.6)$$

The signal significance is:

$$\sigma(M) = \sqrt{2} \text{Erf}^{-1}(p) \quad (4.7)$$

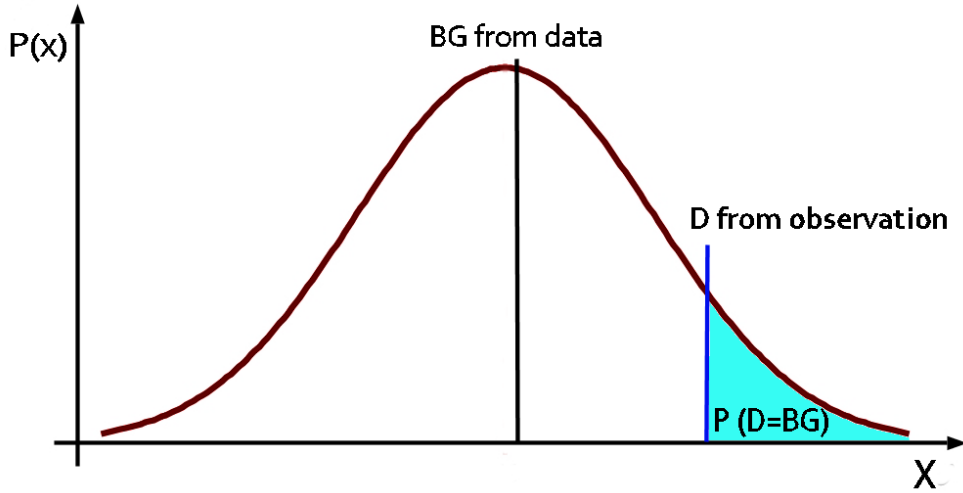


Figure 4.16: The probability for an observed number of events to be a fluctuation of the expected background (example)

$\sigma(M)$  is the number of standard deviations of a Gaussian distributed experiment with the same probability  $p(M)$ .

### 4.11.2 Simulation of pseudo-observations

For further statistical analyses, real observations are simulated. Therefore, for each pseudo-observation, eight random numbers are calculated (separately for signal and background):  $B_A, B_B, B_C, B_D, S_A, S_B, S_C,$  and  $S_D$ , which correspond to the expected numbers of events in each region. The indices represent the four regions and B and S refer to background and signal. The Gaussian mean values are derived from the Monte-Carlo cut analysis, and the standard deviations correspond to the systematic uncertainty of the Monte-Carlo data.

Then, to take the statistical uncertainty for an observation into account, a Poisson distributed random number  $P_i$  is calculated for the signal and the background in each region, with the Gaussian random numbers the parameter for the mean value. The Gaussian and Poisson distributed random numbers are calculated with functions implemented in the ROOT framework.

Most systematic uncertainties in the four regions are correlated, e.g. the jet energy scale is the same for all four regions. To take the correlations into account, for each source of systematic uncertainty a Gaussian distributed random number is computed around a mean value of 0 and a standard deviation of 1. This number is multiplied by the corresponding uncertainties shown in table 4.12 and then added to the corresponding mean value.

For the statistical uncertainties of the Monte-Carlo event numbers, this is done separately for each region.

These pseudo-experiments are performed several times. Figures 4.17, 4.18, 4.19 and 4.20 show the distribution of the pseudo-observed events in the four regions. In the control regions A, B, and C, the SUSY content is comparatively low by construction. In contrast, in the signal region D the background+SU4 scenario clearly differs from the background-only scenario, which is the aimed-for case.

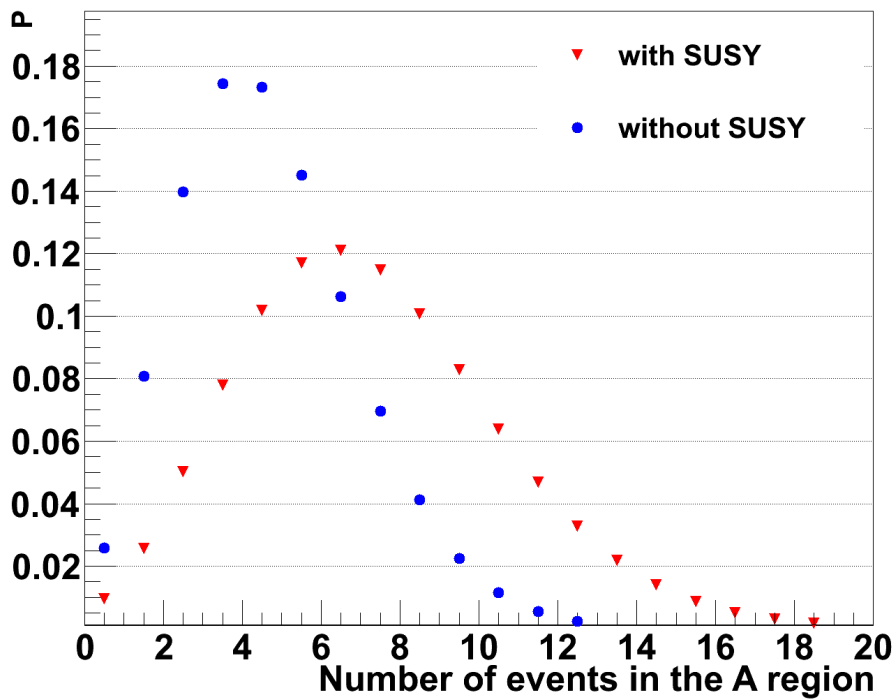


Figure 4.17: The predicted number of observed events in region A for  $200 \text{ pb}^{-1}$ , with and without SU4 contamination

### 4.11.3 Analysis of observations

Each pseudo- or real experiment yields four values  $A_{obs}$ ,  $B_{obs}$ ,  $C_{obs}$ , and  $D_{obs}$ . From these numbers, one has to decide if there is a significant excess in the signal region. Therefore, the number of background events in the signal region has to be estimated via (see section 4.9)

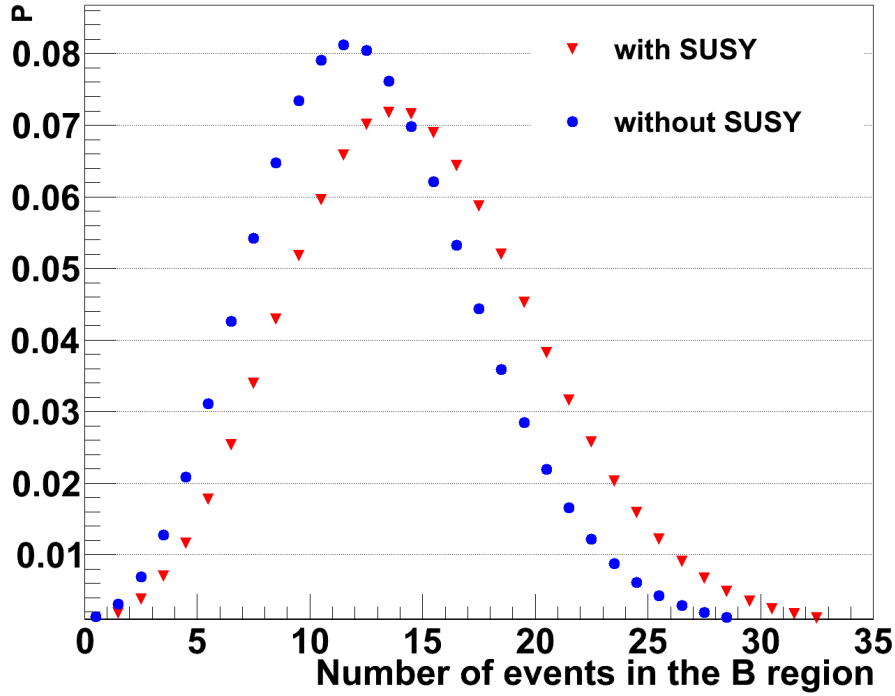


Figure 4.18: The predicted number of observed events in region B for  $200 \text{ pb}^{-1}$ , with and without SU4 contamination

$$D_{BG} = \frac{A_{obs} \cdot C_{obs}}{B_{obs}}$$

Then, a Poisson distribution is built with a mean value of  $D_{BG}$ , and the significance is calculated with respect to  $D_{obs}$ . Figure 4.21 shows the distribution of  $D_{BG}$  for several million pseudo-experiments. For a first glance, the systematic uncertainty of the ABCD method is not taken into account in this subsection, but will be in section 4.11.4. Figure 4.22 shows the integral of the frequency distribution of the calculated significance, i.e. the probability to observe at least a given significance. The green circles correspond to the significance probability if SUSY doesn't exist, the red triangles correspond to the significance probability if SUSY exists at the SU4 point. For the SU4 point at  $200 \text{ pb}^{-1}$ , a significance of at least 5.5 is observed with a probability of 68%.

#### 4.11.4 Uncertainty of the ABCD method

The ABCD method of background estimation from data is based on the assumption that  $\frac{A}{B} = \frac{D}{C}$ . The method was tested with Monte-Carlo data and has

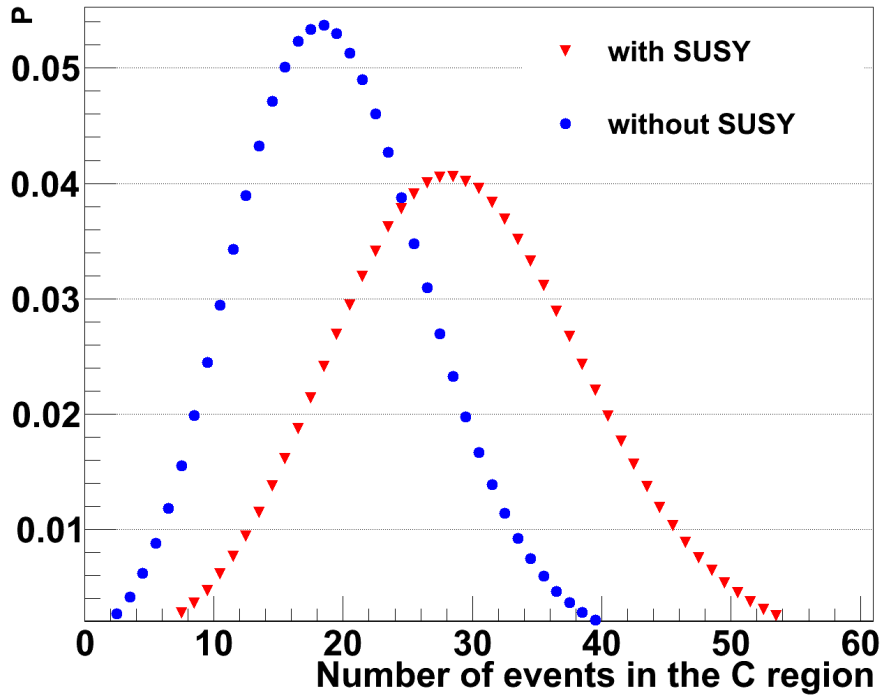


Figure 4.19: The predicted number of observed events in region C for  $200 \text{ pb}^{-1}$ , with and without SU4 contamination

systematic uncertainties. If one wants to be exact, these uncertainties have to be taken into account again when deciding whether a real observation is significant or not.

Therefore, a formula correction parameter  $f$  is determined, which is calculated as follows:

$$f = \frac{B_f \cdot D_f}{A_f \cdot C_f} \quad (4.8)$$

Here,  $A_f$ ,  $B_f$ ,  $C_f$ , and  $D_f$  are random numbers following a Gaussian distribution, with mean values according to the Monte-Carlo numbers for the background, and standard deviations corresponding to their systematic uncertainties. Again, the correlations of the uncertainties in A-D are taken into account by calculating a single Gaussian random number per source of systematic uncertainty for all four regions (see subsection 4.11.2).

If  $f$  is calculated several times, a frequency distribution for  $f$  is obtained, shown in Figure 4.23. From this distribution, the mean value  $f_{mean}$  and the standard deviation  $f_{sigma}$  are determined.

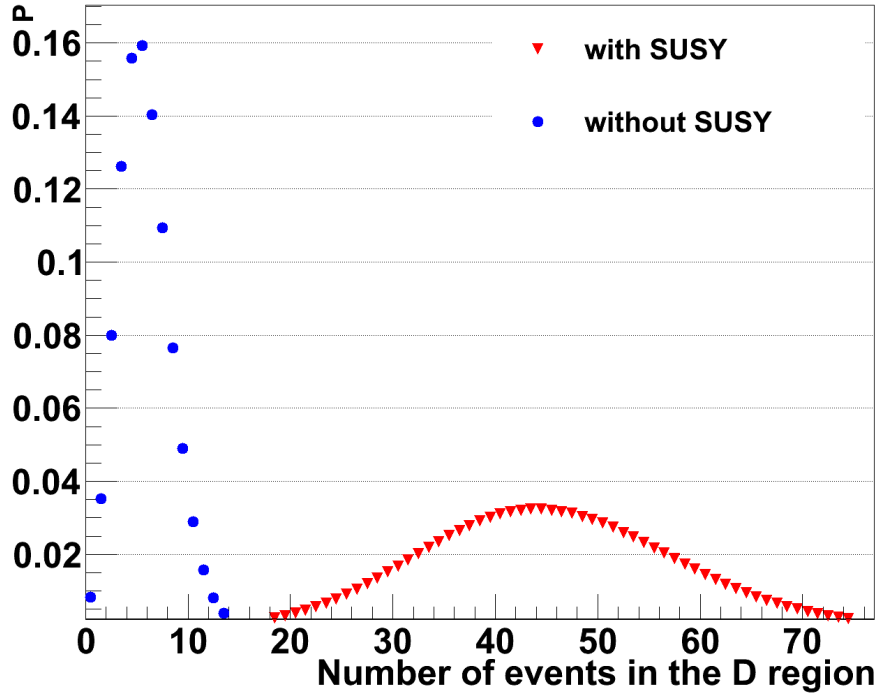


Figure 4.20: The predicted number of observed events in region D for  $200 \text{ pb}^{-1}$ , with and without SU4 and SM background

Instead of building a single Poisson distribution for the significance calculation, Gaussian random numbers are computed with a mean of  $\frac{A_{obs} \cdot C_{obs}}{B_{obs}} \cdot f_{mean}$  and a standard deviation of  $\frac{A_{obs} \cdot C_{obs}}{B_{obs}} \cdot f_{\sigma}$ , where the index *obs* indicates that A, B, C, and D are the event numbers obtained from a real or a simulated observation. These random numbers are the mean values for consecutively calculated Poisson distributions, which are all added up. The sum of all Poisson distributions is normalized in order to obtain a new probability distribution, from which the significance is calculated.

Figure 4.24 shows the effect of this method on an example Poisson distribution.

Integrating these smeared Poisson distributions yields lower values for the significance compared to pure Poisson distributions. Figure 4.25 shows the probability to observe at least a given significance when the correction parameter *f* is applied, compared to the significance from unsmeared Poisson distributions.

### Limit by integrated luminosity

The integrated luminosity is a scale factor which affects all regions equally. A lower luminosity increases the statistical uncertainty and the signal significance

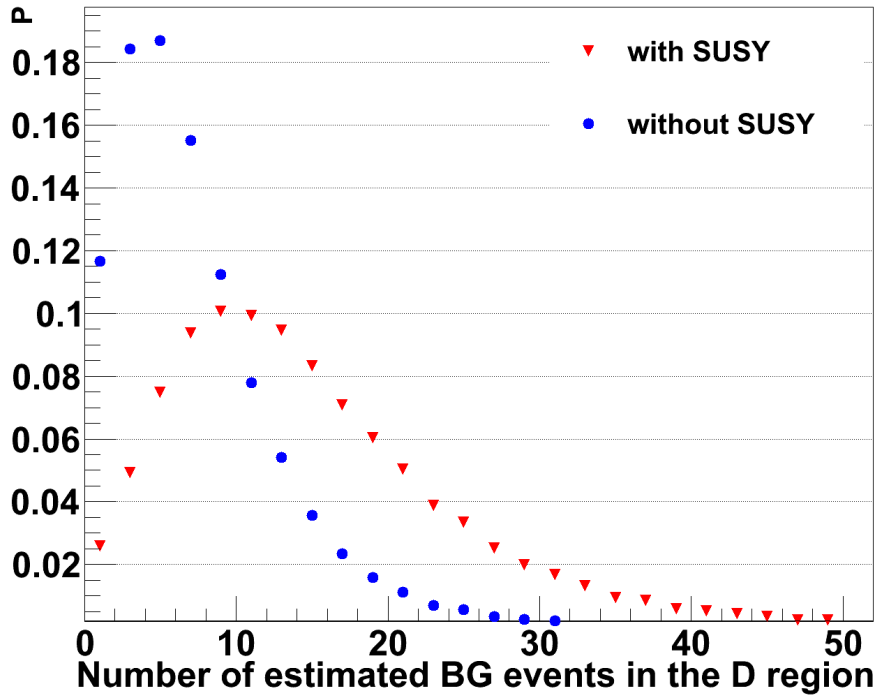


Figure 4.21: The predicted estimated background in region D

decreases. Figure 4.26 shows the probability to observe a SU4 signal significance of at least 5 sigma, as a function of the integrated luminosity. If the latter is about  $160 \text{ pb}^{-1}$ , the probability for at least 5 sigma is about 50% for the SU4 point.

A 3 sigma discovery has a probability of 50%, if the integrated luminosity is  $30 \text{ pb}^{-1}$  (see Figure 4.27).

### SUSY cross section limit

If SUSY exists, but does not exactly match the SU4 point, the apparent SU4 cross-section will be different than expected here. For a lower SUSY cross-section, the number of events in D decreases, but also the SUSY contamination in the control regions, and thus the overestimation of background in D decreases. Figure 4.28 shows the probability to observe at least 5 sigma as a function of the SU4 cross-section scale-factor. Figure 4.29 is a similar plot for a minimum of 3 sigma. If the SU4 cross-section is scaled by a factor of 0.8, the probability to observe at least 5 sigma is 50%, if the factor is 0.4, the probability to observe at least 3 sigma is 50%.

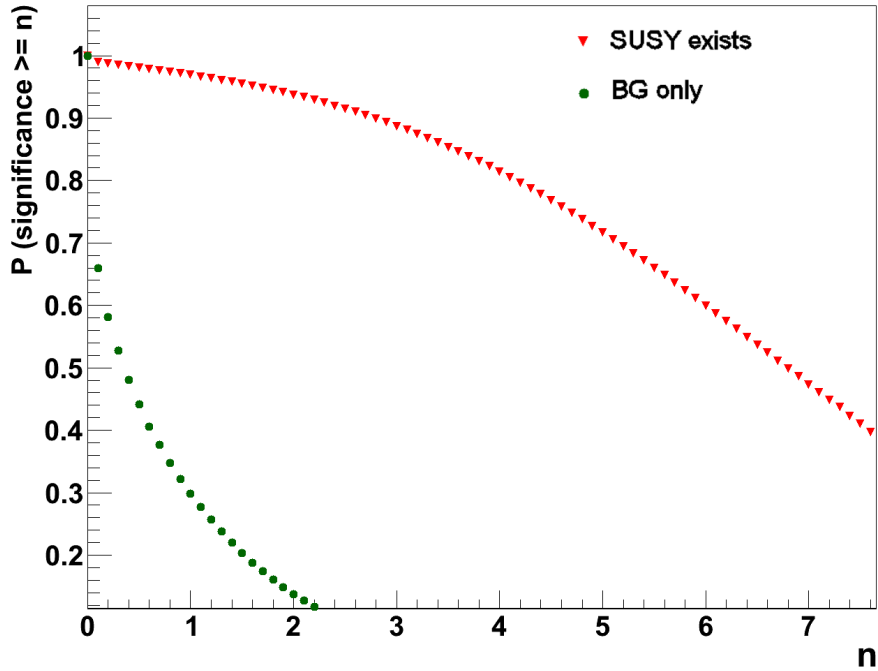
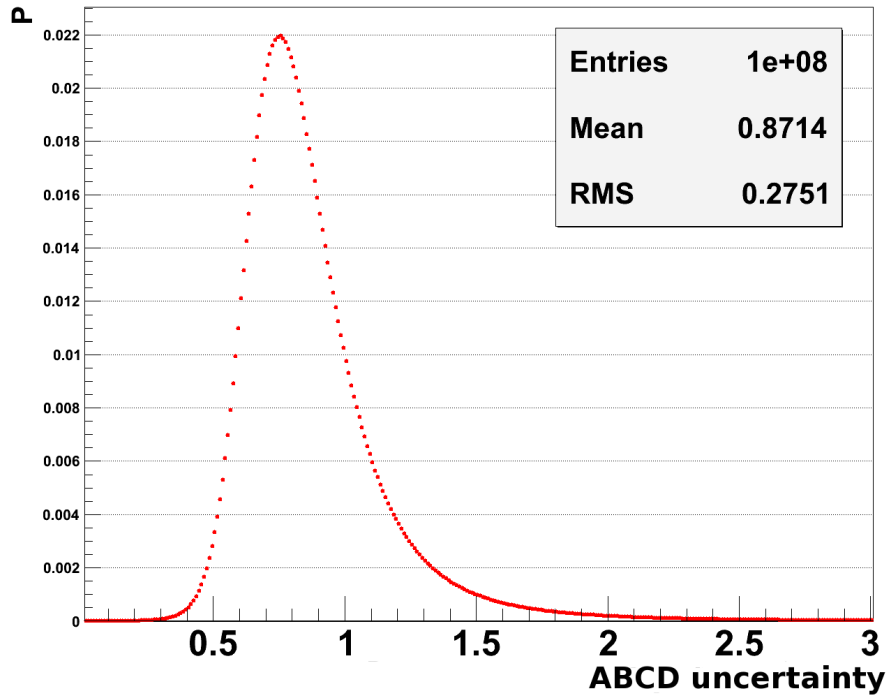


Figure 4.22: The probability to observe at least a given significance with (red triangles) and without (green circles) SU4 at  $200 \text{ pb}^{-1}$

#### 4.11.5 Testing additional points in the $m_0$ - $m_{1/2}$ -plane

The analysis presented in this thesis is optimized for the SU4 point. Nonetheless, other points in the mSUGRA plane could be within reach of this analysis. Table 4.13 lists the available ATLFEST samples for different SUSY points in the  $m_0$ - $m_{1/2}$ -plane. Applying the preselection and analysis cuts to the ATLFEST samples yields the results shown in table 4.14.

For these SUSY points, the significance probability distribution is calculated as described before. To simplify matters, it is assumed that the systematic uncertainties are the same as for the SU4 point, except the uncertainties from Monte-Carlo statistics. Figures 4.30, 4.31, 4.32 and 4.33 exemplarily show the probabilities to observe at least a given significance. The blue squares correspond to the significance from Poisson distributions, the red triangles correspond to the significance where the uncertainty of the ABCD method is taken into account. The discovery potential is the highest for the  $m_0 = 120 \text{ GeV}$  -  $m_{1/2} = 140 \text{ GeV}$  point. With a probability of 50%, the signal significance is at least  $5\sigma$ . For the other points, a 'standalone'  $5\sigma$  discovery is comparatively unlikely (25% and lower), but despite the channels can be interesting in combination with other channels.

Figure 4.23: The probability distribution for the ABCD uncertainty parameter  $f$ 

$m_0$ (GeV)	$m_{1/2}$ (GeV)	Integrated luminosity ( $\text{fb}^{-1}$ )	MC events
120	140	0.96	199249
250	100	0.11	199749
305	135	0.72	99750
360	170	1.14	49647
550	100	0.44	198904
1240	120	0.20	50000
1380	140	0.22	20000
1520	160	0.41	19750
1660	180	0.46	20000
1800	200	0.08	10000

Table 4.13: ATLFAST SUSY samples

$m_0$ (GeV)	A	B	C	D	$P(5\sigma)$
120	$2.9 \pm 0.8$	$0.8 \pm 0.4$	$10.0 \pm 1.4$	$39.9 \pm 2.9$	0.50
250	$3.8 \pm 2.7$	0	$7.6 \pm 3.8$	$13.3 \pm 5.0$	0.08
305	$0.6 \pm 0,4$	$0.6 \pm 0.4$	$1.7 \pm 0.7$	$14.1 \pm 2.0$	0.25
360	$0.9 \pm 0.4$	$0.2 \pm 0.2$	$1.4 \pm 0.5$	$7.9 \pm 1.2$	0.08
550	$1.8 \pm 0.9$	$1.4 \pm 0.8$	$1.8 \pm 0.9$	$14.0 \pm 2.5$	0.17
1240	0	0	$2.0 \pm 1.4$	$8.1 \pm 2.9$	0.12
1380	$0.9 \pm 0.9$	0	$0.9 \pm 0.9$	$1.8 \pm 1.3$	0.03
1520	$0.5 \pm 0.5$	$1.9 \pm 0.7$	0	$5.4 \pm 1.6$	0.07
1660	0	0	$0.4 \pm 0.4$	$3.0 \pm 1.1$	0.04
1800	0	0	0	$7.5 \pm 4.3$	0.14

Table 4.14: The number of events for  $200 \text{ pb}^{-1}$  for the ATLFASST SUSY samples and the probability for a  $5\sigma$  discovery. The errors correspond to the uncertainties from MC statistics.

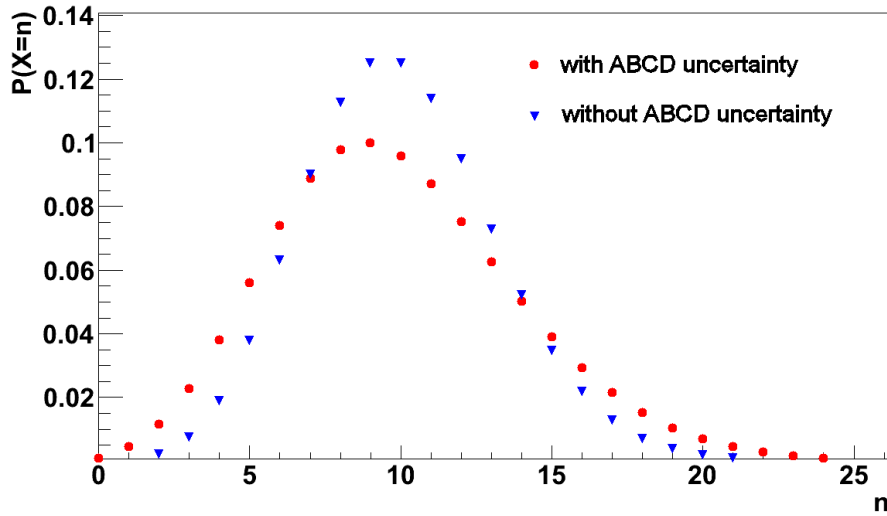


Figure 4.24: The change of the probability distribution, when systematic uncertainties of the ABCD method are taken into account. An example Poisson distribution and its smeared version is shown

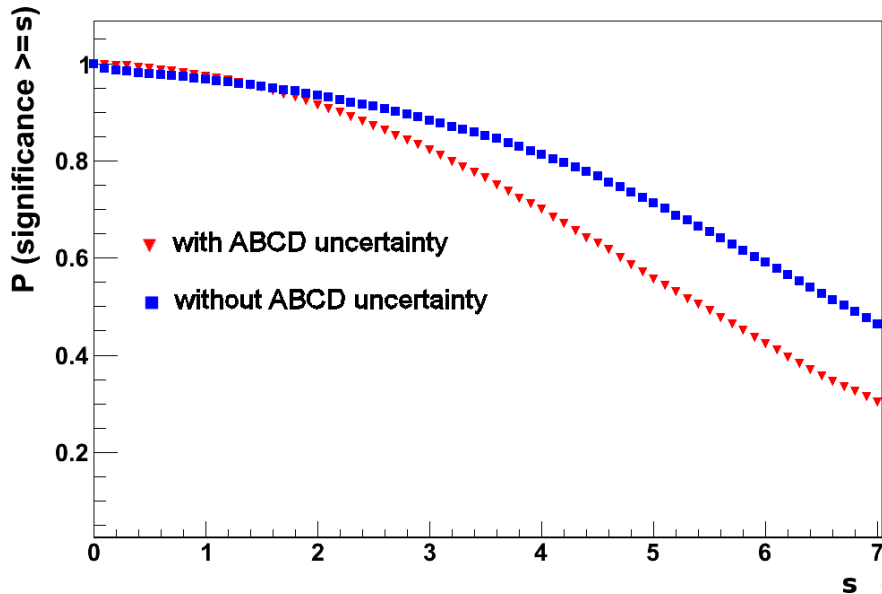


Figure 4.25: The probability to observe at least a given significance for the SU4 point at  $200 \text{ pb}^{-1}$ . The blue squares correspond to the significance calculation from a pure Poisson distribution, the red triangles correspond to the significance calculation, where the systematic uncertainties of the background estimation method is taken into account

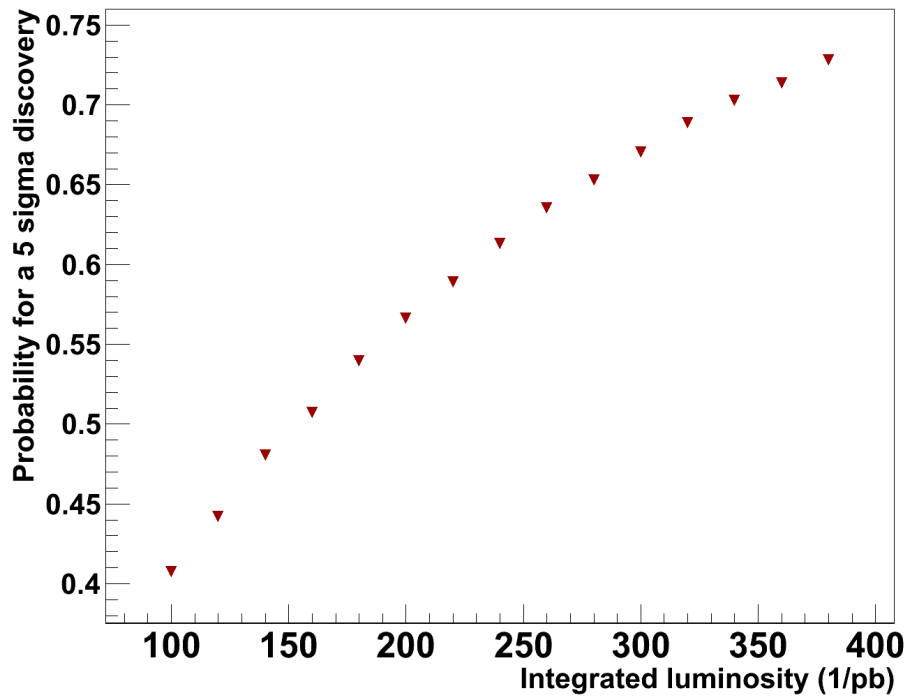


Figure 4.26: The probability to observe at least a 5-sigma-significance as a function of the integrated luminosity

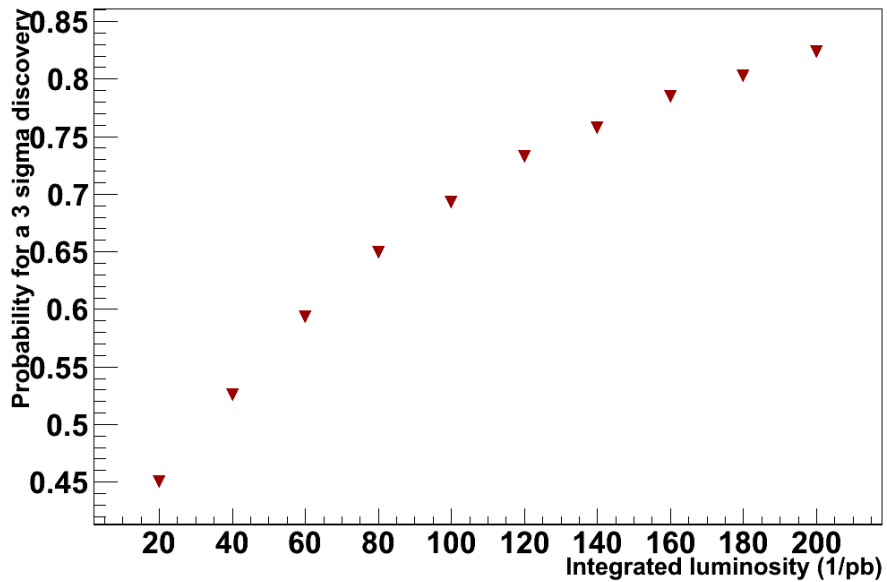


Figure 4.27: The probability to observe at least a 3-sigma-significance as a function of the integrated luminosity

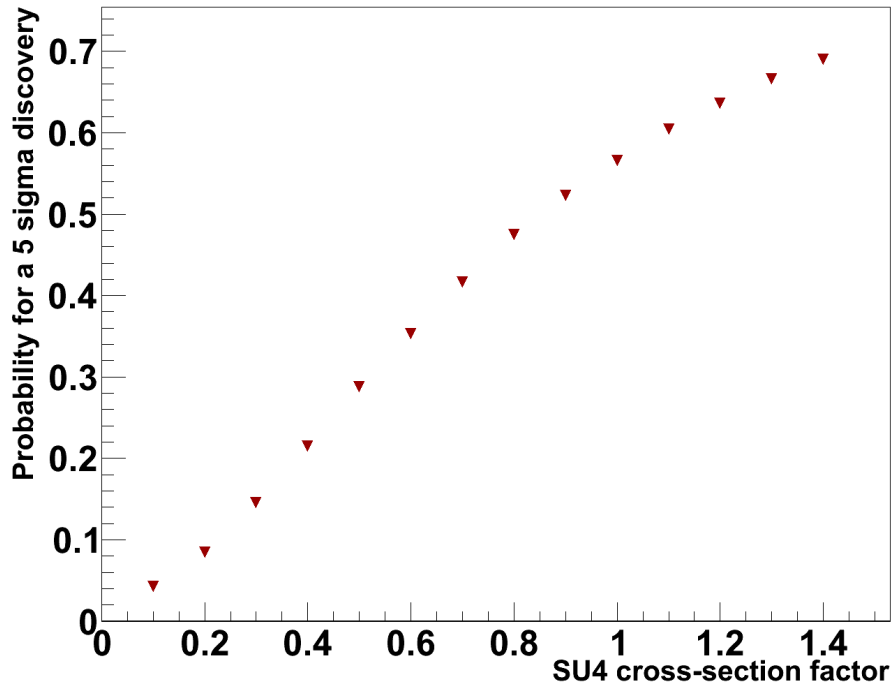


Figure 4.28: The probability to observe at least a 5-sigma significance as a function of the SU4 cross-section scale factor for  $200 \text{ pb}^{-1}$

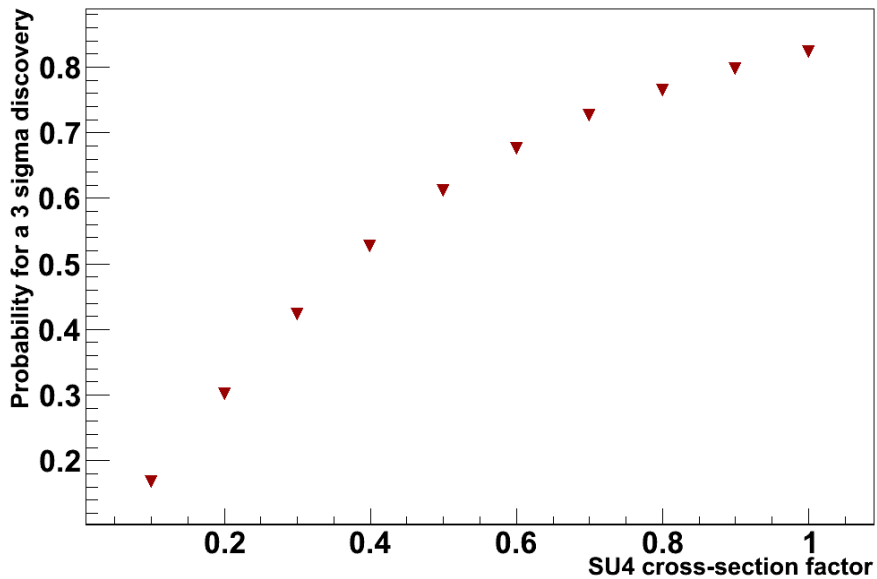


Figure 4.29: The probability to observe at least a 3-sigma significance as a function of the SU4 cross-section scale factor  $200 \text{ pb}^{-1}$

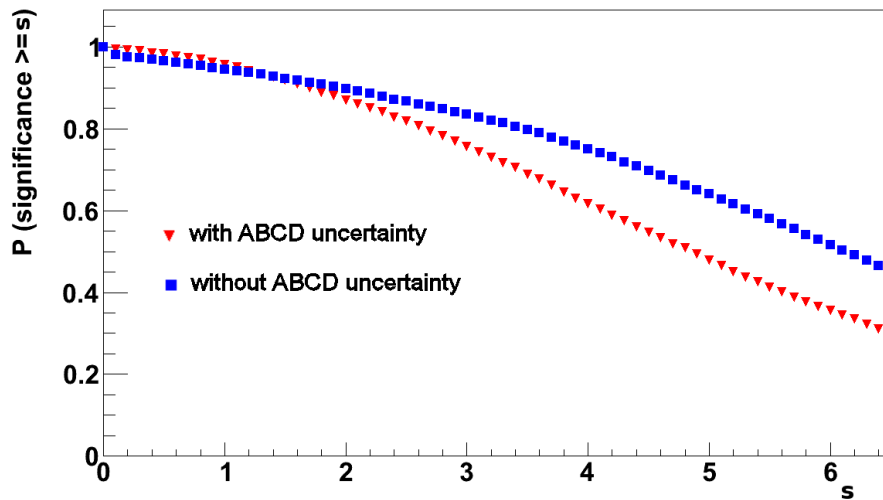


Figure 4.30: The probability to observe at least a given significance for the mSUGRA-point with  $m_0 = 120$  for  $200 \text{ pb}^{-1}$ . The blue squares correspond to the significance calculation from a pure Poisson distribution, the red triangles correspond to the significance calculation, where the systematic uncertainties of the background estimation method is taken into account

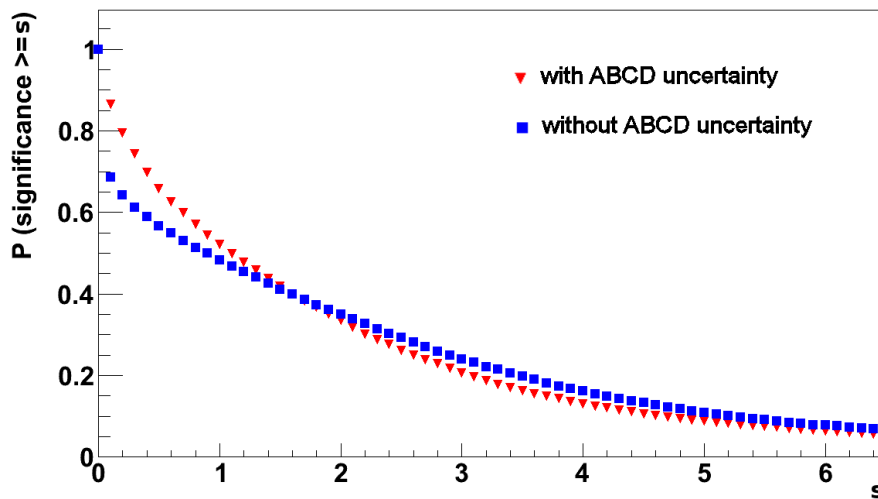


Figure 4.31: The probability to observe at least a given significance for the mSUGRA-point with  $m_0 = 250$  for  $200 \text{ pb}^{-1}$ . The blue squares correspond to the significance calculation from a pure Poisson distribution, the red triangles correspond to the significance calculation, where the systematic uncertainties of the background estimation method is taken into account

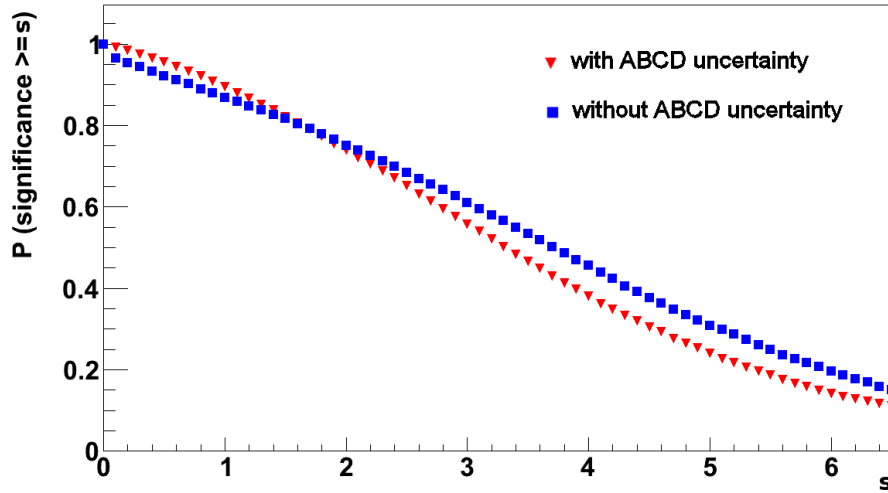


Figure 4.32: The probability to observe at least a given significance for the mSUGRA-point with  $m_0 = 305$  for  $200 \text{ pb}^{-1}$ . The blue squares correspond to the significance calculation from a pure Poisson distribution, the red triangles correspond to the significance calculation, where the systematic uncertainties of the background estimation method is taken into account

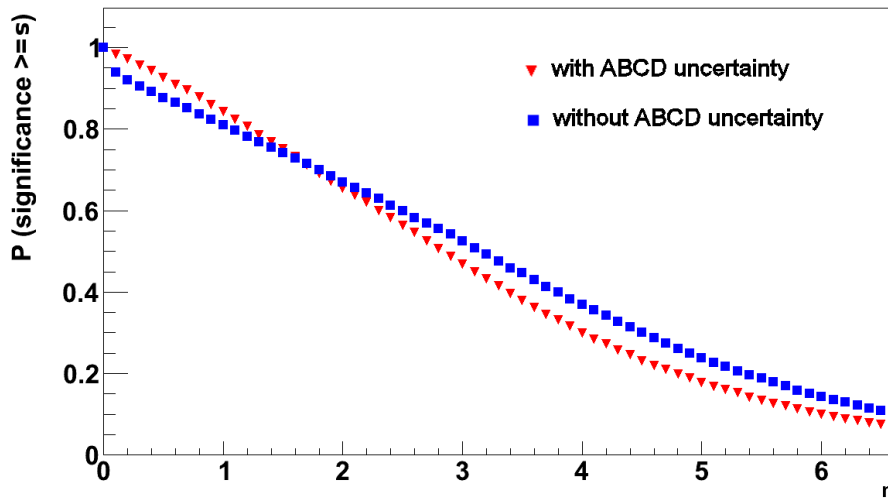


Figure 4.33: The probability to observe at least a given significance for the mSUGRA-point with  $m_0 = 550$  for  $200 \text{ pb}^{-1}$ . The blue squares correspond to the significance calculation from a pure Poisson distribution, the red triangles correspond to the significance calculation, where the systematic uncertainties of the background estimation method is taken into account

### 4.11.6 Exclusion

In order to exclude a specific parameter point of a SUSY model, one has to show, that the observed number of events in the signal region is unlikely to be a statistical fluctuation of the expected number of background plus SUSY events in the signal region. In contrast to statistical analyses with the aim of a discovery, this probability is not transformed into the the corresponding number of Gaussian standard deviations. If the probability, that the observed value is a downward fluctuation of the expected value, is 5% or less, the signal is excluded by definition.

For an exclusion, the method to estimate the background from data as presented in this thesis may not be applied. If SUSY exists, this method tends to overestimate the background, so that an exclusion by mistake becomes more likely.

Instead, the background is simply estimated from the Monte-Carlo data. For a measured number of events in the D region  $D_{obs}$ , the following procedure is performed several times:

Two Gaussian random numbers  $G_{BG}$  and  $G_S$  are computed, with mean values  $D_{BG, MC}$  and  $D_{SU4, MC}$  from Monte-Carlo data, and standard deviations corresponding to the systematic uncertainties of  $D_{BG, MC}$  and  $D_{SU4, MC}$ . Then a Poisson distribution is built with mean value of  $G_{BG} + G_S$ .

All these Poisson distributions are added up, and the resulting distribution  $P_S(n)$  is normalized in order to obtain a probability distribution from which the decision can be made, whether SUSY is excluded or not (see Figure 4.34). Therefore, the probability  $p_S$  that  $D_{obs}$  is a fluctuation of  $D_{BG, MC} + D_{SU4, MC}$  is calculated as follows:

$$p_S = \sum_0^{D_{obs}} P_S(n) \quad (4.9)$$

Now, if  $p$  is lower than a certain threshold value, SUSY at the SU4 point is defined to be excluded. For this thesis, an exclusion at a 95% confidence level is required, so that  $p$  has to be 0.05 or lower.

This method is tested by applying it to the following two scenarios: first, a background-only scenario is analyzed, and second, a scenario where SUSY exists at the SU4 point is analyzed. Performing several pseudo-experiments yields frequency distributions of  $p_S$ . Figures 4.35 and 4.36 show the integral  $\int_0^X p_S$  as a function of the aimed-for exclusion confidence level  $(1-X)$ , where it is assumed that there is no SUSY. The probabilities for a failing exclusion are all lower than the plot resolution (1%). Therefore, the exclusion of the SU4 point works very well.

Figure 4.37 shows a similar plot, this time assuming that SUSY exists at the SU4 point. The curve is a nearly perfect line through origin, with a gradient of 1.

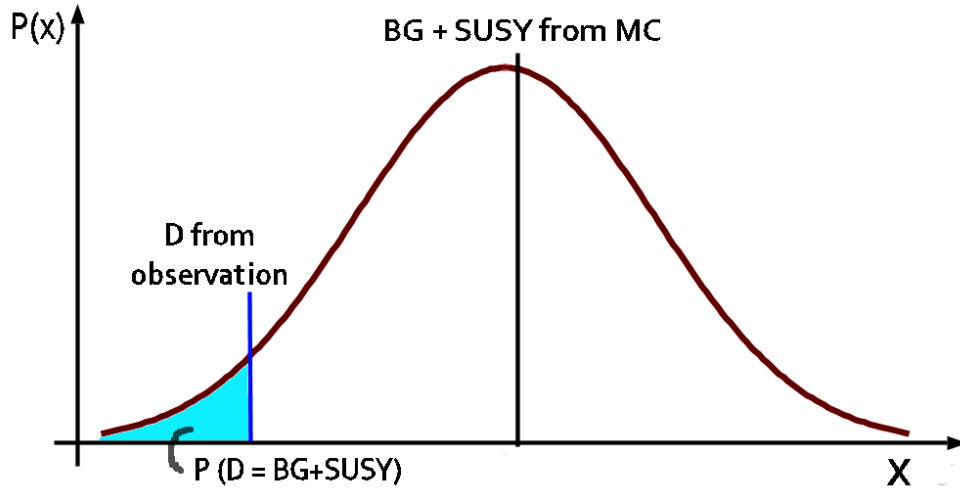


Figure 4.34: The probability for an observed number of events to be a fluctuation of the expected background+signal (example)

This means that for a required confidence level of  $C\%$ , the probability for a false exclusion is  $(100-C)\%$ , demonstrating that the statistical analysis presented here works consistently.

Figure 4.38 is the resulting curve if the background is estimated from data. Here, the probability for a fake exclusion is larger than  $(100-C)\%$ , so that this estimation is indeed not applicable for an exclusion.

In contrast, if the background is underestimated, the probability for a fake exclusion decreases, so that the exclusion still works. The most extreme case is tested here: the background in the signal region is estimated to be 0. Figure 4.39 shows the resulting probability distribution.

#### 4.11.7 Exclusion limit

As shown above, the exclusion reliably works for the SU4 point. The exclusion limit is determined by scaling the SU4 cross-section, assuming that the branching ratios and the systematic uncertainties do not change. For a lower tested cross-section, the expected number of events in the D region decreases, so that an exclusion at a 95% CL becomes less likely. Figure 4.40 shows the probability for a 95% CL exclusion as a function of the SU4 cross-section scale factor, if SUSY doesn't exist. If a minimum probability of 50% is required, SUSY points with a cross-section higher than 16 pb can be excluded.

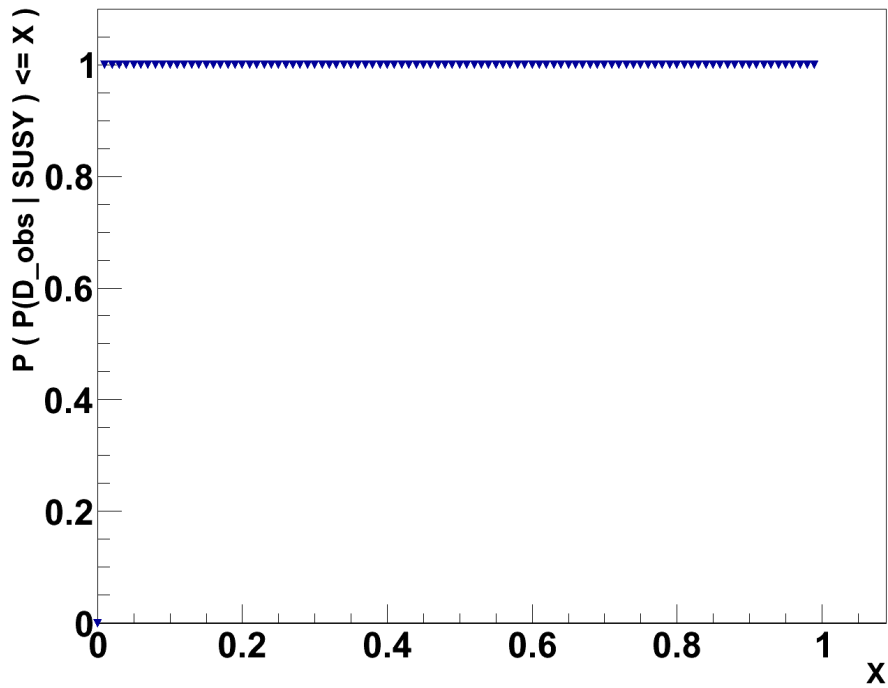


Figure 4.35: The probability, that SU4 is excluded in an observation for  $200 \text{ pb}^{-1}$ , as a function of the required  $(1 - \text{confidence level})$ , if SUSY doesn't exist

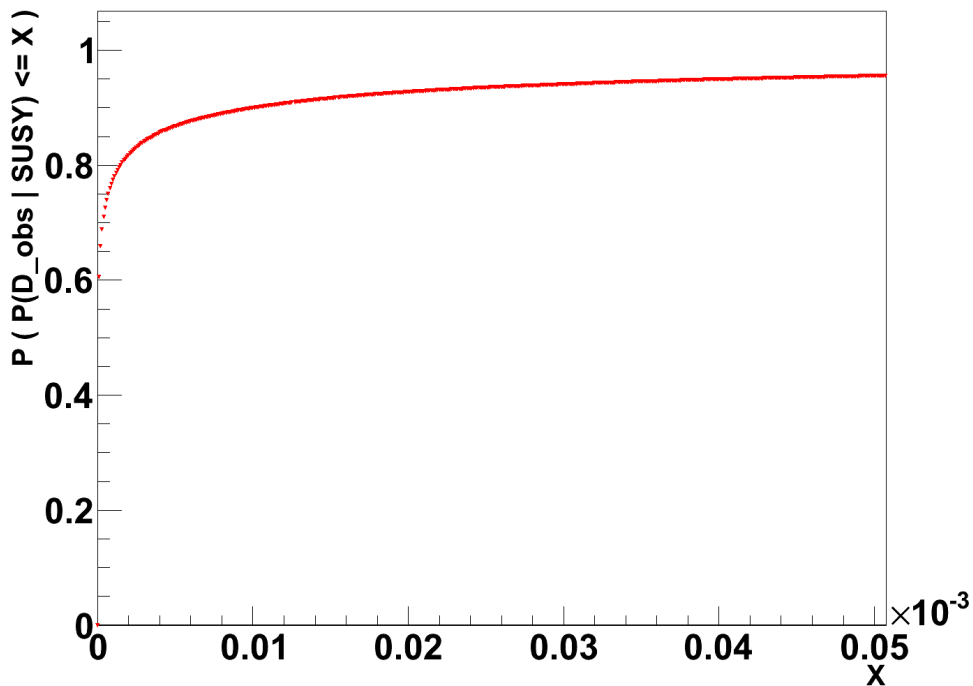


Figure 4.36: The same plot as above, zoomed in to low  $(1 - \text{confidence level})$  values

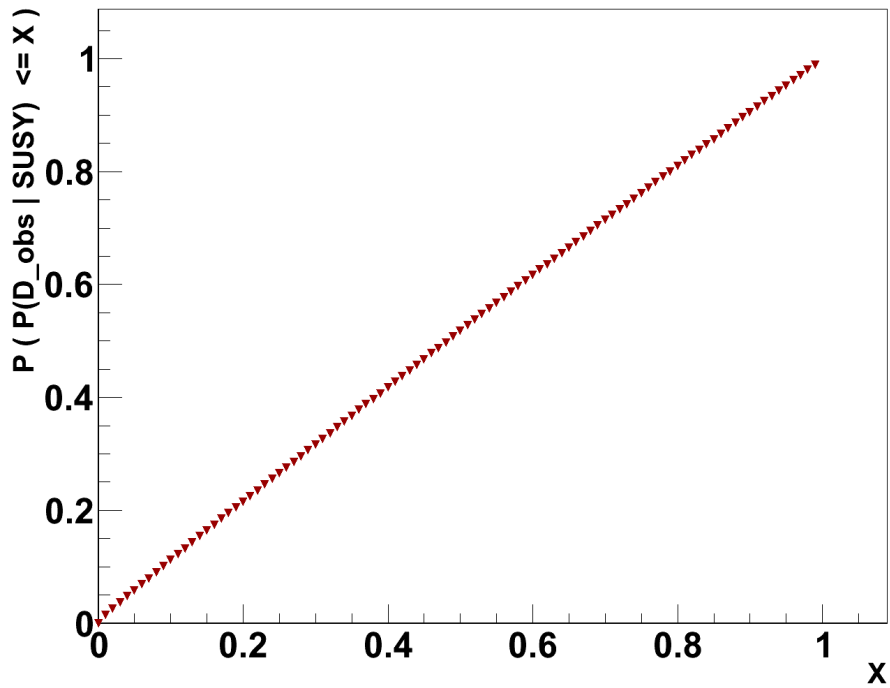


Figure 4.37: The probability, that SU4 is excluded in an observation with  $200 \text{ pb}^{-1}$ , as a function of the required  $(1 - \text{confidence level})$ , if SUSY exists at the SU4 point

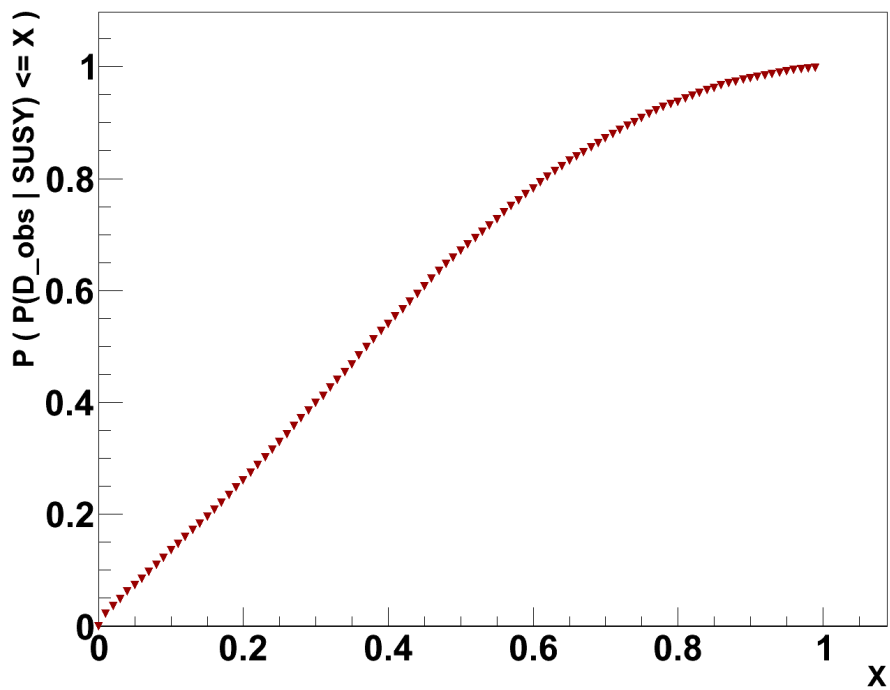


Figure 4.38: The probability, that SU4 is excluded in an observation with  $200 \text{ pb}^{-1}$ , as a function of the required  $(1 - \text{confidence level})$ , if SUSY exists at the SU4 point and the background is estimated from data

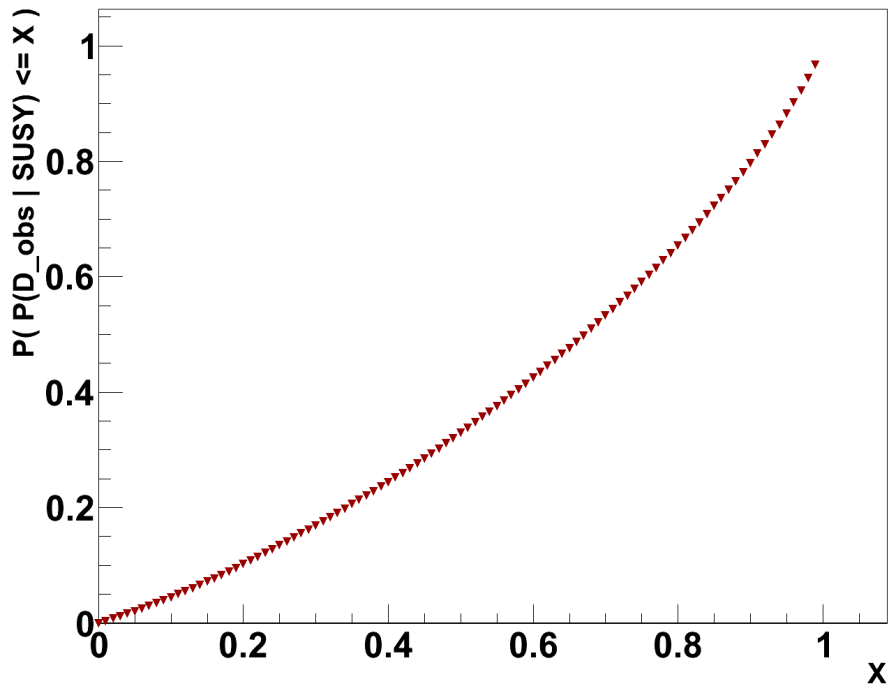


Figure 4.39: The probability, that SU4 is excluded in an observation for  $200 \text{ pb}^{-1}$ , as a function of the required  $(1 - \text{confidence level})$ , if SUSY exists at the SU4 point and the background is estimated to be 0

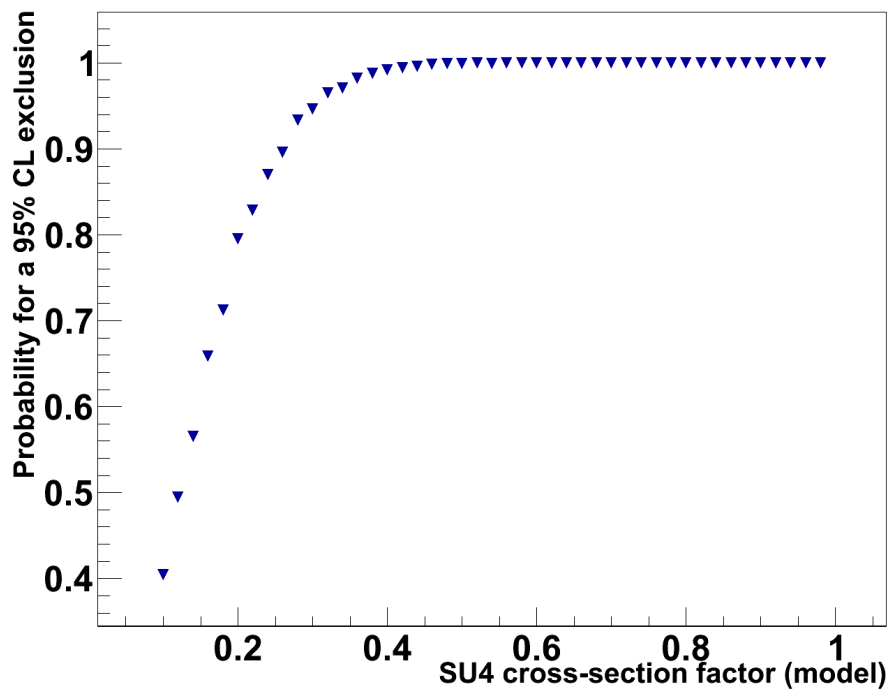


Figure 4.40: The probability, that SU4 is excluded with a 95% CL in an observation with  $200 \text{ pb}^{-1}$ , as a function of the factor the SU4 cross-section is scaled with



# Chapter 5

## Summary and Conclusions

The analysis presented in this thesis is suitable for a discovery of SUSY at the SU4 point with an integrated luminosity of  $200 \text{ pb}^{-1}$  of early ATLAS/LHC data with  $\sqrt{s} = 10 \text{ TeV}$ .

After the object- and event preselection, four analysis cuts define the signal region: First, a Z-veto applied to the invariant dilepton mass reduces contributions from all Z backgrounds. A cut on the transverse mass ( $M_T$  cut = 80 GeV), calculated from the leading lepton and the missing transverse energy, strongly reduces contributions from leptonic W decays and from processes without neutrinos and neutralinos. Third, a cut on the missing transverse energy can efficiently separate SUSY from SM. If the cuts are optimized for the background estimation from data method to work, a comparatively loose cut of  $E_T^{\text{miss}}\text{-cut} = 60 \text{ GeV}$  is applied. Nevertheless, this is still a powerful cut. Finally, requiring at least one jet with a transverse momentum above 100 GeV defines a signal region where SUSY at the SU4 point clearly dominates the SM background. The Gaussian significance is  $\approx 17$ .

A method to improve the QCD background estimation from Monte-Carlo data is given. From single-lepton fake studies the fake rates and the truth-jet and fake electron properties are known. This method replaces jets by fake electrons and recalculates the momenta and the missing transverse energy. The new events are weighted with the estimated corresponding two-lepton fake probability. In the signal region, QCD turns out to play only a minor role compared to the dominant top-antitop background. Nevertheless, the QCD fake rates should be checked with real data.

The SM background can be estimated from data by dividing a 2-dimensional 'cut-space', defined by cuts on the missing transverse energy and cuts on the transverse momentum of the most energetic jet, into four regions: one signal-dominated region D, and three background-dominated control regions A, B, and C (*ABCD-method*). The background in D is then estimated by  $\frac{AC}{B}$ , which has been tested to work with Monte-Carlo data. The systematic uncertainty of the ABCD method, as well as the systematic uncertainties of the effective signal and

background cross-sections in the four regions, are determined.

A method to calculate the signal significance and an exclusion probability from a single observation, including the systematic uncertainty of the ABCD method, is given. With the simulation of observations, frequency distributions for the significance and the exclusion probability are determined, in order to derive discovery and exclusion probabilities, as well as discovery and exclusion limits of this analysis.

If SUSY exists at the SU4-point, the probability for a  $5\sigma$  discovery is roughly 60%. A minimum integrated luminosity of  $160\text{ pb}^{-1}$  is required to obtain a  $5\sigma$  discovery with a probability of more than 50%. For  $200\text{ pb}^{-1}$ , SUSY points with a cross-section above  $85\text{ pb}$  are within the discovery reach of this method, if the branching-ratios are the same as for the SU4 point. None of all tested points in the mSUGRA plane can be discovered with a probability of at least 50%, except the SU4 point.

For an exclusion, the background must not be estimated from data, as this method tends to overestimate the background, but can be estimated from Monte-Carlo data. If the background is estimated to be zero, which is the most conservative estimation, the exclusion method is still applicable. All SUSY models having branching ratios similar to the SU4 point and have cross-sections above  $16\text{ pb}$  can be excluded at 95% CL with a probability of at least 50%.

# Appendix A

## Background Monte-Carlo samples

Table A.1: SM background MC samples (part 1 of 3)

Sample	CSC ID	$\int L \cdot dt$ (fb <sup>-1</sup> )	MC events
Background (part 1 of 3)			
$t\bar{t}$ no all-had.	105200	9.8	1990389
W <sup>+</sup> Z	105941	76.9	20000
W <sup>-</sup> Z	105971	31.3	5000
WW	105985	1.6	25000
ZZ	105987	7.35	10000
Z $\mu\mu$ Np0	107660	0.3	270098
Z $\mu\mu$ Np1	107661	0.3	61686
Z $\mu\mu$ Np2	107662	2.8	197372
Z $\mu\mu$ Np3	107663	3.5	64706
Z $\mu\mu$ Np4	107664	3.7	18470
Z $\mu\mu$ Np5	107665	4.0	5471
ZeeNp0	107650	0.3	269280
ZeeNp1	107651	0.3	61767
ZeeNp2	107652	3.5	216945
ZeeNp3	107653	3.4	63412
ZeeNp4	107654	3.7	18314
ZeeNp5	107655	3.8	5500
Z $\tau\tau$ Np0	107670	0.3	270649
Z $\tau\tau$ Np1	107671	0.3	62678
Z $\tau\tau$ Np2	107672	3.4	210234
Z $\tau\tau$ Np3	107673	3.4	63434
Z $\tau\tau$ Np4	107674	3.7	18500
Z $\tau\tau$ Np5	107675	3.9	5479
ZeebbNp0	109300	24.5	299757

Table A.2: SM background MC samples (part 2 of 3)

Sample	CSC ID	$\int L \cdot dt$ (fb <sup>-1</sup> )	MC events
Background (part 2 of 3)			
ZeebbNp1	109301	30.2	149262
ZeebbNp2	109302	20.4	39985
ZeebbNp3	109303	10.5	10000
Z $\mu\mu$ bbNp0	109305	24.3	298964
Z $\mu\mu$ bbNp1	109306	29.9	147710
Z $\mu\mu$ bbNp2	109307	20.8	39952
Z $\mu\mu$ bbNp3	109308	10.7	10000
Z $\tau\tau$ bbNp0	109310	24.2	299664
Z $\tau\tau$ bbNp1	109311	30.6	149558
Z $\tau\tau$ bbNp2	109312	20.7	39968
Z $\tau\tau$ bbNp3	109313	10.9	10000
W $e\nu$ Np0	107680	0.1	1092217
W $e\nu$ Np1	107681	0.1	262424
W $e\nu$ Np2	107682	0.7	464965
W $e\nu$ Np3	107683	0.9	179450
W $e\nu$ Np4	107684	1.0	58872
W $e\nu$ Np5	107685	1.0	17492
W $\mu\nu$ Np0	107690	0.05	499016
W $\mu\nu$ Np1	107691	0.1	248220
W $\mu\nu$ Np2	107692	1.1	779540
W $\mu\nu$ Np3	107693	1.1	223087
W $\mu\nu$ Np4	107694	0.3	58928
W $\mu\nu$ Np5	107695	0.2	3500
w $\tau\nu$ Np0	107700	0.1	246827
w $\tau\nu$ Np1	107701	0.1	246827

Table A.3: SM background MC samples (part 3 of 3)

Sample	CSC ID	$\int L \cdot dt$ (fb <sup>-1</sup> )	MC events
Background (part 3 of 3)			
w $\tau\nu$ Np2	107702	1.2	793108
w $\tau\nu$ Np3	107703	1.1	223162
w $\tau\nu$ Np4	107704	1.0	58729
w $\tau\nu$ Np5	107705	0.9	17413
wbbNp0	106280	3.0	15500
wbbNp1	106281	3.1	15457
wbbNp2	106282	3.1	8953
wbbNp3	106283	3.1	5000
J0	105009	$8.5 \cdot 10^{-8}$	999266
J1	105010	$1.2 \cdot 10^{-6}$	997956
J2	105011	$1.7 \cdot 10^{-5}$	979316
J3	105012	$4.1 \cdot 10^{-4}$	1357129
J4	105013	$3.9 \cdot 10^{-3}$	598644
J5	105014	$2.7 \cdot 10^{-1}$	1390403
J6	105015	3.57	399269
bbNp0	107340	0.01	91380
bbNp1	107341	0.01	76707
bbNp2	107342	0.01	23250
bbNp3	107343	0.01	6500
stschanenu	108343	13.2	10000
stschan $\mu\nu$	108344	7.9	6000
stschan $\tau\nu$	108345	12.5	9522
sttchanenu	108340	0.8	12000
sttchan $\mu\nu$	108341	0.8	11982
sttchan $\mu\nu$	108342	0.4	6472
Wt	105508	8.7	124984
Z $\gamma$	105899	13.4	99892
W $\gamma$	10509	1.1	24991

# Appendix B

## Transverse Sphericity

The sphericity  $S$  is a measure for the isotropy of an event. A sphericity of 0 corresponds to a perfect back-to-back configuration, whereas a sphericity of 1 corresponds to a perfectly isotropic configuration. In ATLAS, the concept of the three-dimensional sphericity has to be reduced to a planar sphericity perpendicular to the beam axis, called the *Transverse Sphericity*  $S_T$ . Many SUSY searches use the transverse sphericity to discriminate SUSY events, where the detectable SM objects originate from long decay chains and therefore tend to be isotropic, from QCD dijet events, which tend to be in a back-to-back configuration [51]. From all reconstructed objects, i.e. electrons, muons and jets, the 2x2 transverse sphericity tensor  $S_{ij}$  is calculated as follows:

$$S_{ij} = \begin{pmatrix} \sum p_x^2 & \sum p_x p_y \\ \sum p_y p_x & \sum p_y^2 \end{pmatrix} \quad (\text{B.1})$$

With the eigenvalues  $\lambda_1$  and  $\lambda_2$  of the transverse spheric

$$S_T = \frac{2\lambda_1}{\lambda_1 + \lambda_2} \quad (\text{B.2})$$

A cut on  $S_T$  is important for SUSY searches in a 0- or 1-lepton mode, where QCD events comprise the dominant background.

This cut has also been tested for this analysis, but it turned out not to improve the overall signal significance. Figure B.1 shows the transverse sphericity for the SU4 signal and the QCD J4 dijet sample.

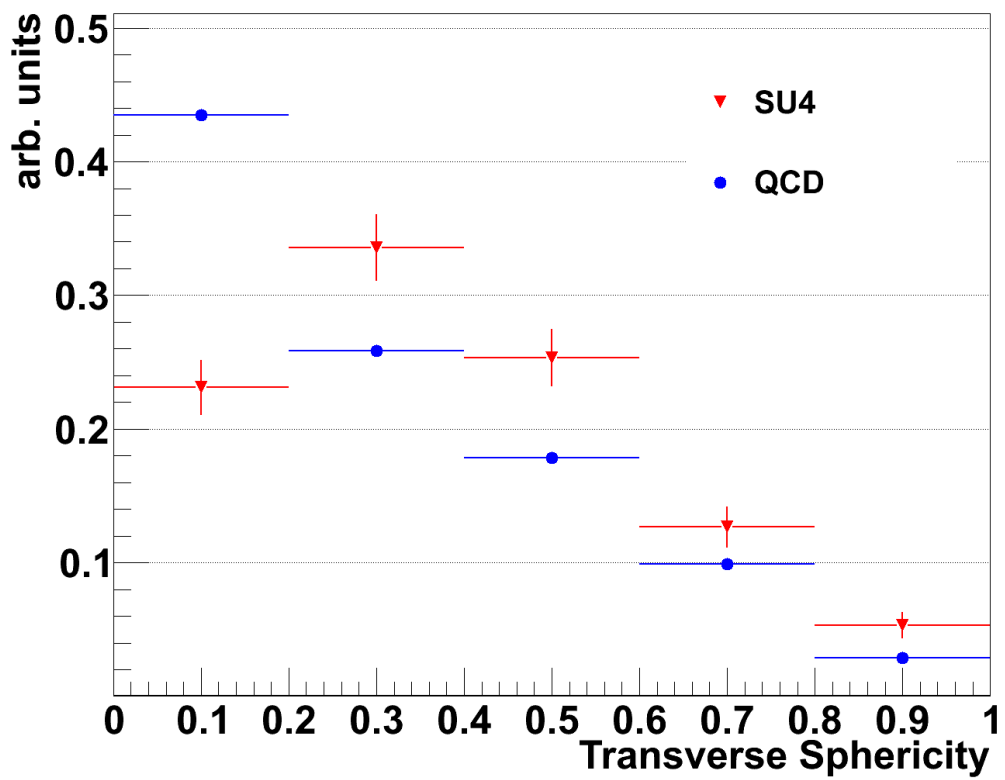


Figure B.1: The transverse sphericity for SU4 and QCD. Both histograms are normalized to  $\sum(\text{entries}) = 1$ .

# Bibliography

- [01] G.D. Coughlan, J.E. Dodd, B. Gripaios: *The Ideas of Particle Physics*, Cambridge University Press, 2006
- [02] C. Amsler: *Kern- und Teilchenphysik*, vdf Hochschulverlag AG, 2007
- [03] C. Berger: *Elementarteilchenphysik*, Springer-Verlag, 2002
- [04] D.H. Perkins: *Hochenergiephysik*, Addison-Wesley, 1991
- [05] R.N. Mohapatra: *Unification and Supersymmetry*, Springer, 1992
- [06] K. Kleinknecht: *Detektoren fuer Teilchenstrahlung*, B.G. Teubner, 1984
- [07] M. Drees, R. Godbole, P. Roy: *Theory and Phenomenology of Sparticles*, World Scientific, 2005
- [08] J. Ellis: *Supersymmetry for alp hikers*, arXiv, hep-ph/0203114, 2002
- [09] M. Dittmar: *SUSY discovery strategies at the LHC*, arXiv, hep-ex/9901004, 1999
- [10] X. Tata: *What is supersymmetry and how do we find it?*, arXiv, hep-ph/9706307, 1997
- [11] S.P. Martin: *A supersymmetry primer*, arXiv, hep-ph/9709356v5, 2008
- [12] M.L. Mangano: *Standard Model backgrounds to supersymmetry searches*, arXiv, hep-ph/0809.1567, 2008
- [13] P. de Jong: *Prospects for SUSY searches in CMS and ATLAS*, AIP Conference Proceedings, Volume 1078, pp. 21-29 (2008)
- [14] H. Baer, A. Lessa and H. Summy: *Early SUSY discovery at LHC via sparticle cascade decays to same-sign and multimuo states*, Physics Letters B Volume 674, Issue 1, 6 April 2009, Pages 49-53
- [15] J.L. Feng, J.-F. Grivaz, J. Nachtman: *Searches for Supersymmetry at High-Energy Colliders*, arXiv, hep-ex/0903.0046v2, 2009

- [16] H. Baer, V. Barger, A. Lessa, X. Tata: Supersymmetry discovery potential of the LHC at  $\sqrt{s} = 10$  and 14 TeV without and with missing ET, arXiv, hep-ph/0907.1922v2, 2009
- [17] H. Baer: Leptonic signatures for SUSY at the LHC, arXiv, hep-ph/0909.1515v1, 2009
- [18] I. Iashvili: MSSM SUSY SEARCHES AT LEP2, arXiv, hep-ex/0007001v1, 2000
- [19] J. Kraus, C. Schmitt, E. von Törne, N. Wermes: First observation of electrons in the ATLAS detector, ATLAS notes, ATL-PHYS-COM-2009-564, 2009
- [20] G. Belanger, F. Boudjema, A. Pukhov, A. Semenov: micrOMEGAs: Version 1.3, Computer Physics Communications, Volume 174, Issue 7, 1 April 2006, Pages 577-604
- [21] G. Belanger, F. Boudjema, A. Pukhov, A. Semenov: micrOMEGAs 2.0: a program to calculate the relic density of dark matter in a generic model, Computer Physics Communications, Volume 177, Issue 11, 1 December 2007, Pages 894-895
- [22] B. Resende: Muon identification algorithms in ATLAS, Proceedings of science, EPS-HEP 2009, 2009
- [23] The ATLAS Collaboration: The ATLAS Experiment at the CERN Large Hadron Collider, INSTITUTE OF PHYSICS PUBLISHING AND SISSA, JINST 3 S08003, 2008
- [24] The ATLAS Collaboration: Expected performance of the ATLAS experiment, CERN-OPEN-2008-020
- [25] J. Will, M.-H. Genest: Study of reconstructed leptons from QCD background in inclusive SUSY searches with ATLAS, ATLAS internal notes, ATL-PHYS-INT-2009-063, 2009
- [26] M.-H. Genest: Prospects for R-Parity Conserving SUSY searches at the LHC, Proceedings of Science, ATL-PHYS-PROC-2009-081, 2009
- [27] The ATLAS collaboration: Searching for Supersymmetry with two same-sign-leptons, multi-jets plus missing transverse energy in ATLAS at  $\sqrt{s} = 14TeV$ , ATLAS notes, ATL-PHYS-PUB-2009-085, 2009
- [28] S. Kawagoe and K. Komamiya: Search for Gluino Pair Production Through Their Cascade Decay Into Same Sign Dileptons, ATLAS internal notes, phys-93-014, 1993

- [29] H. Kroha, X. Zhuang and V. Zhurlov: Estimation of Top Background to SUSY Searches from Data, ATLAS slides, ATLAS-PHYS-SLIDE-2009-231, 2009
- [30] J. de Graat: Suche nach Gebieten auffälliger Signaturen im SUSY Parameterraum, Diplomarbeit, LS Schaile, 2008
- [31] M. Wichmann: Electron Charge Misidentification in the ATLAS Detector, Diplomarbeit, LS Schaile, 2008
- [32] M. Binder: Search for the Trilepton Signal of the Minimal Supergravity Model in D0 Run II, PhD Thesis, LS Schaile, 2005
- [33] The ATLAS Collaboration: Performance of Jet Algorithms in the ATLAS Detector, ATLAS Notes, ATLAS-PHYS-XXX-2009-XXX [SIC], 2009
- [34] G. Krobath: Search for Second Generation Leptoquarks with ATLAS at the LHC, PhD Thesis, LS Schaile, 2008
- [35] R. Mameghani: Semi- and Dileptonic Top Pair Decays at the ATLAS Experiment, PhD Thesis, LS Schaile, 2008
- [36] D. N. Spergel, L. Verde, H. V. Peiris, E. Komatsu, M. R.olta, C. L. Bennett, M. Halpern, G. Hinshaw, N. Jarosik, A. Kogut, M. Limon, S.S. Meyer, L. Page, G. S. Tucker, J. L. Weiland, E. Wollack, E. L. Wright: First Year Wilkinson Microwave Anisotropy Probe (WMAP ) Observations: Determination of Cosmological Parameters, *Astrophys.J.Suppl.*148:175-194,2003
- [37] O. Arnaez: Electron Reconstruction and Identification with the ATLAS Detector, Slides for SUSY09 conference (05-10/06/2009 in Northeastern University), ATLAS-COM-PHYS-2009-290, 2009
- [38] The LHC Computing Grid, URL: <http://lcg.web.cern.ch/LCG/>, accessed 02-December-2009
- [39] CERN press release, URL: <http://press.web.cern.ch/press/PressReleases/Releases2009/PR18.09E.html>, accessed 02-December-2009
- [40] LEP2 SUSY working group: Combined LEP chargino results, URL: [http://lepsusy.web.cern.ch/lepsusy/www/inos\\_moriond01/charginos\\_pub.html](http://lepsusy.web.cern.ch/lepsusy/www/inos_moriond01/charginos_pub.html), accessed 02-December-2009
- [41] LHC: BEAM PARAMETERS AND DEFINITIONS, URL: [https://edms.cern.ch/file/445830/5/Vol\\_1\\_Chapter\\_2.pdf](https://edms.cern.ch/file/445830/5/Vol_1_Chapter_2.pdf), accessed 08-December-2009

- [42] LHC: 2009 start-up procedure, URL: <http://user.web.cern.ch/user/news/2009/090806-LHC-restart-energy.html>, accessed 08-December-2009
- [43] J. Dietrich: ATLAS SUSY search prospects at 10 TeV, arXiv, hep-ex/0910.5653v1, 2009
- [44] The ATLAS Collaboration: Searching for Supersymmetry with two same-sign leptons, multi-jets plus missing transverse energy in ATLAS at  $\sqrt{s} = 10$  TeV, ATLAS note, ATL-COM-PHYS-2009-343, 2009
- [45] The D0 collaboration: Search for associated production of charginos and neutralinos in the trilepton final state using  $2.3 \text{ fb}^{-1}$  of data, Physics Letters B, Volume 680, Issue 1, p. 34-43, 2009
- [46] ROOT, URL: <http://root.cern.ch/drupal/>, accessed 08-December-2009
- [47] ATHENA, URL: <https://twiki.cern.ch/twiki/bin/view/Atlas/AthenaFramework>, accessed 08-December-2009
- [48] A. Farbin: ATLAS Analysis Model, Journal of Physics: Conference Series 119 (2008) 042012
- [49] J.T. Moscicki, F. Brochu, J. Ebke, U. Egede, J. Elmsheuser, K. Harrison, R.W.L. Jones, H.C. Lee, D. Liko, A. Maier, A. Muraru, G.N. Patrick, K. Pajchel, W. Reece, B.H. Samset, M.W. Slater, A. Soroko, C.L. Tan, D.C. van der Ster and M. Williams: Ganga: a tool for computational-task management and easy access to Grid resources, Computer Physics Communications, Volume 180, Issue 11, p. 2303-2316
- [50] URL: <http://public.web.cern.ch/public/en/Research/LEP-en.html>, accessed 11-December-2009
- [51] A. Richards: R-parity conserving SUSY studies with Jets and Missing Transverse Energy, URL: [http://www.hep.ucl.ac.uk/theses/1styear/2007/ar\\_report.pdf](http://www.hep.ucl.ac.uk/theses/1styear/2007/ar_report.pdf), accessed 11-December-2009
- [53] The particle data group: Dark Matter, URL: <http://pdg.lbl.gov/2009/reviews/rpp2009-rev-dark-matter.pdf>, accessed 11-December-2009
- [54] The particle data group: Statistics, URL: <http://pdg.lbl.gov/2009/reviews/rpp2009-rev-statistics.pdf>, accessed 11-December-2009

# List of Tables

2.1	Elementary fermions in the SM and their assigned quantum numbers. The signs refer to fermions (upper sign) and anti-fermions (lower sign). . . . .	8
2.2	The MSSM mass eigenstates . . . . .	11
3.1	List of stable particles and the corresponding sensitivity of the ATLAS subdetectors . . . . .	29
4.1	The ATLAS SUSY benchmark points [24] . . . . .	36
4.2	Signal MC samples . . . . .	39
4.3	Effects of the preselection cuts on signal and background. The values given for QCD refer to the method described below. . . . .	44
4.4	The definition of the A,B,C and D region . . . . .	45
4.5	Z-Veto efficiencies and surviving events . . . . .	47
4.6	Transverse mass cut efficiencies and surviving events . . . . .	49
4.7	Missing transverse energy cut efficiencies and surviving events . . . . .	49
4.8	Leading jet $p_T$ cut efficiencies and surviving events . . . . .	50
4.9	Cut flow table for QCD. The event numbers and MC uncertainties are calculated for $200 \text{ pb}^{-1}$ . . . . .	54
4.10	The definition of the A,B,C and D region . . . . .	56
4.11	Four regions in a 2-dim cut space. The values for signal and background are scaled to an integrated luminosity of $200 \text{ pb}^{-1}$ . The errors refer to the uncertainties from MC statistics. . . . .	57
4.12	Systematic uncertainties . . . . .	61
4.13	ATLFAST SUSY samples . . . . .	70
4.14	The number of events for $200 \text{ pb}^{-1}$ for the ATLFAST SUSY samples and the probability for a $5\sigma$ discovery. The errors correspond to the uncertainties from MC statistics. . . . .	71
A.1	SM background MC samples (part 1 of 3) . . . . .	86
A.2	SM background MC samples (part 2 of 3) . . . . .	87
A.3	SM background MC samples (part 3 of 3) . . . . .	88



# List of Figures

2.1	The dependence of the inverse couplings on the energy scale in the Standard Model (left) and in the MSSM (right) [32] . . . . .	12
2.2	RG evolution of the $m_0$ and $m_{\frac{1}{2}}$ mass parameters in the MSSM with typical mSUGRA boundary conditions [11] . . . . .	13
2.3	Region in the $m_0$ - $m_{1/2}$ -plane excluded by the combination of the D0 analyses (green), by LEP searches for charginos (light gray) and sleptons (dark gray) and CDF (black line) [45] . . . . .	14
2.4	The mSUGRA $m_0$ - $m_{1/2}$ -plane with its allowed and forbidden regions for a given set of parameters [30] . . . . .	15
2.5	Couplings of Wino and Bino to fermion-sfermion pairs . . . . .	16
2.6	The coupling of squarks, quarks and gluinos . . . . .	17
2.7	Sparticle production by gluon-gluon- and quark-gluon reactions . . . . .	19
2.8	An typical supersymmetric cascade decay [30] . . . . .	20
2.9	An example for a gluino cascade decay (upper) and the direct chargino-neutralino-production (lower) . . . . .	21
3.1	The LHC at CERN with some experiments . . . . .	24
3.2	The ATLAS detector . . . . .	25
3.3	The ATLAS coordinate system . . . . .	26
3.4	The ATLAS Inner Detector . . . . .	27
3.5	The ATLAS calorimeter system . . . . .	28
3.6	The ATLAS muon system . . . . .	29
3.7	Particle detection in ATLAS . . . . .	30
3.8	The ATLAS trigger system . . . . .	31
3.9	The structure of the LHC computing grid . . . . .	32
3.10	The full analysis chain for ATLAS Monte-Carlo data and real data in the ATHENA framework . . . . .	34
4.1	The production modes for top-antitop via gluon-gluon fusion and quark-antiquark annihilation [35] . . . . .	37
4.2	The three decay modes for top-antitop: all-hadronic (left), semileptonic (middle) and fully leptonic (right) . . . . .	37
4.3	Semileptonic $t\bar{t}$ decay . . . . .	38

4.4	Hadrons assigned to jets by a cone algorithm with two overlapping cones . . . . .	41
4.5	The calorimeter isolation <code>etcone20</code> for all electrons after the preselection. Both histograms are normalized to $\sum(\text{entries}) = 1$ . . . . .	43
4.6	Invariant dilepton mass distribution. All histograms are normalized to $\sum(\text{entries}) = 1$ . . . . .	46
4.7	Transverse mass distribution. All histograms are normalized to $\sum(\text{entries}) = 1$ . . . . .	48
4.8	Missing transverse energy distribution. All histograms are normalized to $\sum(\text{entries}) = 1$ . . . . .	50
4.9	Leading jet $p_T$ distribution. All histograms are normalized to $\sum(\text{entries}) = 1$ . . . . .	51
4.10	The probability to find a fake electron as a function of the truth jet $p_T$ . . . . .	53
4.11	The dependence of the fake electron $p_{Ts}$ on the truth jet $p_{Ts}$ . . . . .	55
4.12	The distribution of $\frac{p_{T,fakeel}}{p_{T,truthjet}}$ with a gaussian fit. The fit parameters are: Mean = 0.63, $\sigma=0.19$ . . . . .	55
4.13	The missing transverse energy and the transverse momentum of the leading jet for the $t\bar{t}$ sample after preselection. The entries in the 0 GeV bin for the jet momenta correspond to events without reconstructed jets. . . . .	57
4.14	The transverse momentum of the leading jet for all background samples, shown for $E_T^{\text{miss}} > \text{cut}$ and for $E_T^{\text{miss}} < \text{cut}$ . . . . .	58
4.15	The missing transverse energy for all background samples, shown for $\text{Jet}_{1st} p_T > \text{cut}$ and for $\text{Jet}_{1st} p_T < \text{cut}$ . . . . .	58
4.16	The probability for an observed number of events to be a fluctuation of the expected background (example) . . . . .	63
4.17	The predicted number of observed events in region A for $200 \text{ pb}^{-1}$ , with and without SU4 contamination . . . . .	64
4.18	The predicted number of observed events in region B for $200 \text{ pb}^{-1}$ , with and without SU4 contamination . . . . .	65
4.19	The predicted number of observed events in region C for $200 \text{ pb}^{-1}$ , with and without SU4 contamination . . . . .	66
4.20	The predicted number of observed events in region D for $200 \text{ pb}^{-1}$ , with and without SU4 and SM background . . . . .	67
4.21	The predicted estimated background in region D . . . . .	68
4.22	The probability to observe at least a given significance with (red triangles) and without (green circles) SU4 at $200 \text{ pb}^{-1}$ . . . . .	69
4.23	The probability distribution for the ABCD uncertainty parameter $f$ . . . . .	70
4.24	The change of the probability distribution, when systematic uncertainties of the ABCD method are taken into account. An example Poisson distribution and its smeared version is shown . . . . .	72

4.25 The probability to observe at least a given significance for the SU4 point at  $200 \text{ pb}^{-1}$ . The blue squares correspond to the significance calculation from a pure Poisson distribution, the red triangles correspond to the significance calculation, where the systematic uncertainties of the background estimation method is taken into account 72

4.26 The probability to observe at least a 5-sigma-significance as a function of the integrated luminosity . . . . . 73

4.27 The probability to observe at least a 3-sigma-significance as a function of the integrated luminosity . . . . . 73

4.28 The probability to observe at least a 5-sigma significance as a function of the SU4 cross-section scale factor for  $200 \text{ pb}^{-1}$  . . . . . 74

4.29 The probability to observe at least a 3-sigma significance as a function of the SU4 cross-section scale factor  $200 \text{ pb}^{-1}$  . . . . . 74

4.30 The probability to observe at least a given significance for the mSUGRA-point with  $m_0 = 120$  for  $200 \text{ pb}^{-1}$ . The blue squares correspond to the significance calculation from a pure Poisson distribution, the red triangles correspond to the significance calculation, where the systematic uncertainties of the background estimation method is taken into account . . . . . 75

4.31 The probability to observe at least a given significance for the mSUGRA-point with  $m_0 = 250$  for  $200 \text{ pb}^{-1}$ . The blue squares correspond to the significance calculation from a pure Poisson distribution, the red triangles correspond to the significance calculation, where the systematic uncertainties of the background estimation method is taken into account . . . . . 75

4.32 The probability to observe at least a given significance for the mSUGRA-point with  $m_0 = 305$  for  $200 \text{ pb}^{-1}$ . The blue squares correspond to the significance calculation from a pure Poisson distribution, the red triangles correspond to the significance calculation, where the systematic uncertainties of the background estimation method is taken into account . . . . . 76

4.33 The probability to observe at least a given significance for the mSUGRA-point with  $m_0 = 550$  for  $200 \text{ pb}^{-1}$ . The blue squares correspond to the significance calculation from a pure Poisson distribution, the red triangles correspond to the significance calculation, where the systematic uncertainties of the background estimation method is taken into account . . . . . 76

4.34 The probability for an observed number of events to be a fluctuation of the expected background+signal (example) . . . . . 78

4.35 The probability, that SU4 is excluded in an observation for  $200 \text{ pb}^{-1}$ , as a function of the required  $(1 - \text{confidence level})$ , if SUSY doesn't exist . . . . . 79

4.36	The same plot as above, zoomed in to low ( $1 - \text{confidence level}$ ) values . . . . .	79
4.37	The probability, that SU4 is excluded in an observation with $200 \text{ pb}^{-1}$ , as a function of the required ( $1 - \text{confidence level}$ ), if SUSY exists at the SU4 point . . . . .	80
4.38	The probability, that SU4 is excluded in an observation with $200 \text{ pb}^{-1}$ , as a function of the required ( $1 - \text{confidence level}$ ), if SUSY exists at the SU4 point and the background is estimated from data . . . . .	80
4.39	The probability, that SU4 is excluded in an observation for $200 \text{ pb}^{-1}$ , as a function of the required ( $1 - \text{confidence level}$ ), if SUSY exists at the SU4 point and the background is estimated to be 0 . . . . .	81
4.40	The probability, that SU4 is excluded with a 95% CL in an observation with $200 \text{ pb}^{-1}$ , as a function of the factor the SU4 cross-section is scaled with . . . . .	81
B.1	The transverse sphericity for SU4 and QCD. Both histograms are normalized to $\sum(\text{entries}) = 1$ . . . . .	90

# Danksagungen

An dieser Stelle möchte ich mich bei all jenen bedanken, die zum Gelingen dieser Arbeit beigetragen haben.

Als erstes möchte ich Prof. Dr. Dorothee Schaile danken, dass sie mich in ihren Lehrstuhl aufgenommen und mir die Möglichkeit zu dieser Arbeit gegeben hat.

Des weiteren danke ich PD Dr. Raimund Stroehmer für die herausragende Betreuung und die zahlreichen konstruktiven Ideen und Vorschläge.

Mein Dank geht an den Zweitgutachter dieser Arbeit, Prof. Dr. Wolfgang Dünneweber.

Dr. Günter Duceck danke ich für die Möglichkeit, mich in zahlreichen und verschiedenen Aspekten des Grid Computing zu betätigen.

Je voudrais remercier Dr. Cedric Serfon pour les aides précieuses et sa patience infinie.

Merci beaucoup à Dr. Marie-Hélène Genest pour produire toutes les DPDs, et aussi pour ses idées secourables.

Vielen Dank auch an Dipl. Phys. Johannes Ebke für die interessanten und hilfreichen Diskussionen über Statistik.

Frau Herta Franz danke ich für ihre zuverlässige Arbeit im Sekretariat.

Für die angenehme Arbeitsatmosphäre möchte ich mich bei allen Mitgliedern des Lehrstuhls Schaile bedanken.

Insbesondere bedanke ich mich bei Sebastian Becker, Dipl. Phys. Julien de Graat und Dr. Cedric Serfon für die angenehme Stimmung im Büro.

Bei Sebastian Becker, Dipl. Phys. Markus Lichtnecker und PD Dr. Raimund Stroehmer bedanke ich mich fürs Korrekturlesen.

Für die vielen netten und interessanten Gespräche bedanke ich mich bei Stefanie Adomeit, Sebastian Becker, Dr. Johannes Elmsheuser, Dipl.Phys. Albert Engl, Dipl.-Phys. Julien de Graat, Dr. Raphael Mameghani, Dipl.Phys. Thomas Müller, Dr. Benjamin Ruckert, Dipl.Phys. Jonas Will und Andre Zibell.

Von Herzen danke ich meinen Eltern Margit und Kurt Kummer für den Rückhalt und die Unterstützung nicht nur während der Promotion.

Meiner Freundin Franziska danke ich für Belange jenseits der Physik.



